Development of a drop-on-demand inkjet system for stroboscopic small- and wide-angle X-ray scattering experiments

Rita Graceffa

▶ **To cite this version:**

Rita Graceffa. Development of a drop-on-demand inkjet system for stroboscopic small- and wide-angle X-ray scattering experiments. Physics [physics]. Université Joseph-Fourier - Grenoble I, 2010. English. NNT : . tel-00446582

HAL Id: tel-00446582
https://theses.hal.science/tel-00446582

Submitted on 13 Jan 2010

HAL is a multi-disciplinary open access archive for the deposit and dissemination of scientific research documents, whether they are published or not. The documents may come from teaching and research institutions in France or abroad, or from public or private research centers.

L'archive ouverte pluridisciplinaire **HAL**, est destinée au dépôt et à la diffusion de documents scientifiques de niveau recherche, publiés ou non, émanant des établissements d'enseignement et de recherche français ou étrangers, des laboratoires publics ou privés.

UNIVERSITÉ JOSEPH FOURIER
ECOLE DOCTORALE DE PHYSIQUE
EUROPEAN SYNCHROTRON RADIATION FACILITY

DOCTOR OF PHYLOSOPHY DEGREE

Specialty: Physique de la Matière Condensée e du Rayonnement

Rita GRACEFFA

Thesis supervised by Christian RIEKEL
Defense on February the 2nd, 2010

Development of a drop-on-demand inkjet system for stroboscopic small- and wide-angle X-ray scattering experiments

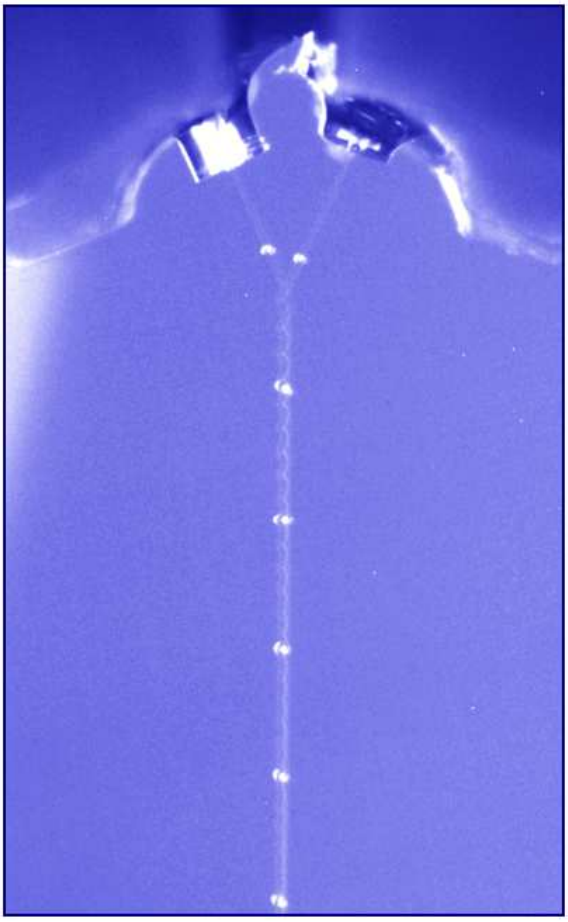

JURY :

S. PEREZ	European Synchrotron Radiation Facility, Grenoble	Member
E.M. DI FABRIZIO	Università degli studi Magna Græcia, Catanzaro	Reporter
J.B. SALMON	Laboratory of Future, Bordeaux	Reporter
M. ROESSLE	European Molecular Biology Laboratory, Hamburg	Member
C. RIEKEL	European Synchrotron Radiation Facility, Grenoble	Thesis Supervisor

The cover picture rapresents two inkjet heads working at a frequency of 2kHz. The ejected microdrops mix in flight. The illumination allows to visualize the microdrops positions and their full trajectory.

UNIVERSITÉ JOSEPH FOURIER
ECOLE DOCTORALE DE PHYSIQUE
EUROPEAN SYNCHROTRON RADIATION FACILITY

THESE DE DOCTORAT

Spécialité: Physique de la Matière Condensée e du Rayonnement

Rita GRACEFFA

Thèse dirigée par by Christian RIEKEL
Soutenue le 2 February 2010

Développement d'un instrument de mélange de gouttes pour jets d'encre synchronisés pour expérience de diffusion centrale et de diffraction de rayons X

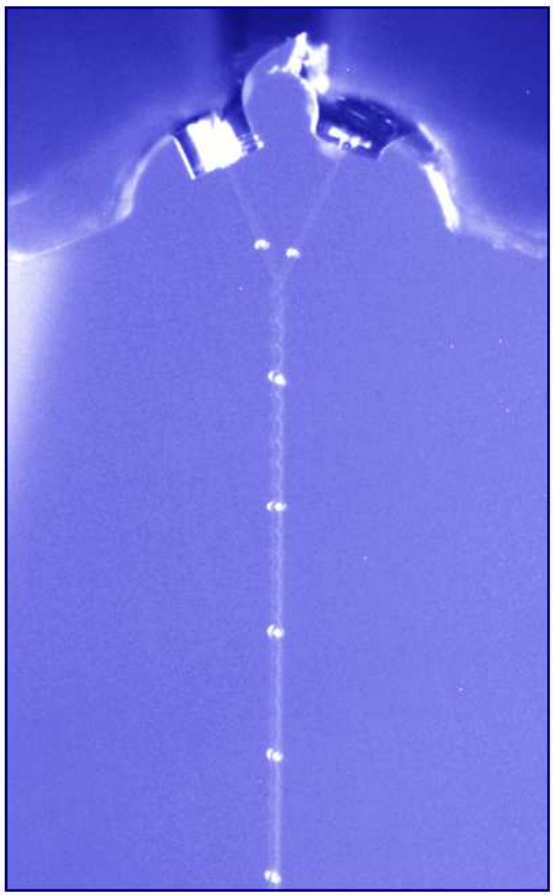

COMPOSITION DE JURY :

S. PEREZ	European Synchrotron Radiation Facility, Grenoble	President
E.M. DI FABRIZIO	Università degli studi Magna Græcia, Catanzaro	Rapporteur
J.B. SALMON	Laboratory of Future, Bordeaux	Rapporteur
M. ROESSLE	European Molecular Biology Laboratory, Hamburg	Examinateur
C. RIEKEL	European Synchrotron Radiation Facility, Grenoble	Directeur de thése

L’image de couverture représente deux têtes de jet d'encre fonctionnant à une fréquence de 2kHz. Les microgouttes se mélangent en vol. L'illumination permet la visualisation de les positions de microgouttes et leur pleine trajectoire.

Abbreviations

BL	Beamline
CCD	Charge Coupled Device
COM	Communication port (PC)
CXDI	Coherent X-ray Diffraction Imaging
cyt c	Cytochrome C
d	diameter
DDU	Dispenser-Drive-Unit
DOD	Drop-On-Demand
DSC	Differential Scanning Calorimetry
E_{kin}	kinetic energy
E_s	surface energy
ESRF	European Synchrotron Radiation Facility
k	thermal conductivity
k_B	Boltzmann's constant
KB-mirrors	Kirkpatrick-Baez mirrors
kD	kilo-Daltons
LED	Light Emitting Diode
MD	Molecular Dynamics
MCP	Micro-Channel-Plate
ml	milli-liter
ms	milli-second
NIM	Nuclear Instrumentation Module
nl	nano-liter
OPIOM	Octal Programmable I/O Module
PC	Personal Computer
pl	pico-liter
SAXS	Small-Angle X-ray Scattering
SPEC	UNIX-based software package for instrument control and data acquisition
SR	Synchrotron Radiation
t	time (s)
T	temperature (K)
TTL	Transistor-Transistor-Logic
VME	Virtual Machine Environment
WAXS	Wide-Angle X-ray Scattering

Greek symbols

μl	micro-liter
μm	micro-meter
μs	micro-second
η	viscosity
ν	speed

Contents

Motivation

Microfluidics is the science and technology of systems that process or manipulate small (10^{-9} to 10^{-18} litres) amounts of fluids. (Whitesides 2006) The "lab-on-a-chip" concept is shrinking a chemical or biochemical laboratory to the dimension of a microchip (Knight 2002) which is getting in the range of functional biological units and is generating an increasing interest in mimicking nature. The practical advantages of microfluidics are a substantial reduction of reagent consumption and a reduction of timescales for diffusion processes which is of interest for studying fast processes such as conformational changes of proteins.

The principal aim of my thesis project was to develop "in-flight" microdrop mixing by crossed inkjets in analogy to "in-channel" microfluidic mixing techniques. (Ottino and Wiggins 2004) Microdrop technology allows significantly reducing sample volumes as compared to microfluidic technology and wall effects, such as shearing or aggregation, can be avoided. As this type of use of microdrops had not been tested before, the risk of my thesis was that the instrumentation development would become too dominating. I am therefore happy that I could also use the technique for scientific applications.

1. Introduction

La microfluidique est la science et la technologie des systèmes qui manipulent de petits volumes de fluides (10^{-9} à 10^{-18} litres). Le concept de "laboratoire sur puce" fait rétrécir un laboratoire chimique ou biochimique à la dimension d'une micropuce qui rentre à la gamme d'unités biologiques fonctionnelles et produit un intérêt croissant dans imiter la nature. Les avantages pratiques de microfluidics sont une réduction substantielle de consommation de réactif et une réduction d'échéance de les processus de diffusion qui sont intéressants pour étudier des processus vite comme les changements de conformation de protéines.

Le but principal de mon projet de thèse était de développer un instrument de mélange en vol de microgouttes pour jets d'encre synchronisés. Les microgouttes balistiques passent voir l'air peut être pensé comme des navires de réaction avec des volumes en bas à la pl-gamme. Les réactifs restent limités dans les microgouttes pendant leur trajectoire. Les effets de tondage induits de la présence murale ne jouent pas de rôle; bien que la compression mécanique de la solution pendant le processus d'éjection puisse influencer l'intégrité structurelle de protéines fragiles.

J'ai exploré dans ma thèse pour la première fois la combinaison de microgouttes balistiques avec des techniques de microdiffusion stroboscopique. L'effort instrumental principal était donc de développer une installation stable avec deux jets d'encre pour étudier mélange de microgouttes en vol à l'ID13-BL utilisant expériences de diffusion centrale et de diffraction de rayons X stroboscopique. J'ai utilisé ces techniques pour étudier la paraffine liquide en vol et des microgouttes de cytochrome C et la coalescence de microgouttes de cytochrome C avec des microgouttes de tampon de Na-acetate. J'ai également exécuté des expériences exploratoires de diffraction de rayons X à la ligne de lumière ID13 sur des microgouttes de paraffine solide déposés sur des surfaces et la diffraction dépendante de la température sur le solide de paraffine pour calibrer les données stroboscopiques. Des expériences statiques de diffusion centrale ont été exécutées à la ligne de lumière ID02 pour obtenir des courbes de la référence pour les états de conformation de solutions du cytochrome C .

Comme ce type d'utilisation de microgouttes n'avait pas été évalué auparavant, le risque de ma thèse était que le développement d'instrumentation deviendrait aussi la dominance. Je suis donc heureux que j'aie pu aussi utiliser la technique pour des applications scientifiques.

1. Introduction

Microfluidic devices are generally associated with liquids confined by μm-sized channels (Whitesides 2006) or drops in a carrier liquid. (Song, Chen et al. 2006; Utada, Fernandez-Nieves et al. 2007) This type of technology has enabled a multitude of new applications ranging from fast mixing (Knight, Vishwanath et al. 1998; Akiyama, Takahashi et al. 2002), complex fluids (Pfohl, Mugele et al. 2003), proteomics (Lion, Rohner et al. 2003), as well as high-throughput crystallization and in particular protein crystallization. (Hansen, Skordalakes et al. 2002; Hansen and Quake 2003; Leng and Salmon 2009) Among the principal advantages of microfluidics technology are the small dimensions of microfluidic devices implying an important reduction of sample volumes (Whitesides 2006), the fast response and short analysis times, completeness of processes and easily adaptable designs. (Dootz, Evans et al. 2007) The upcoming of "digital microfluidics" (Berthier 2008) suggests, however, a larger view of microfluidics as the movement of drops on surfaces can be controlled by an electrode structure without the confinement by a channel. (Berthier 2008)

Microdrops generated by inkjet systems can also be associated to microfluidic devices. (Lee 2003) The term "microdrop" will be used in this work for drops which are free falling (or "ballistic") in air and with a shape dominated by their surface tension. (see Chapter 4) Printing devices were at the origin of inkjet systems. Starting in the 50th as continuous jet-dispensing systems (Elmqvist 1951; Sweet 1965), the first drop-on-demand (DOD) inkjet systems became available in the 70th. (Zoltan 1974; Kyser and Sears 1976; Endo, Sato et al. 1979) For a review on different DOD inkjet systems see: (Lee 2003; Burgold, Weise et al. 2005). Today inkjet R&D is boosted by biotechnology such as the printing of protein biochip arrays. (Zaugg and Wagner 2003; Dijksman and Pierik 2008; Delaney, Smith et al. 2009) For a overview on other technological applications see: (Gans, Duineveld et al. 2004)

Microdrops surrounded by a flow of immiscible fluid resemble to ballistic microdrops. (Song, Chen et al. 2006) It is also interesting to note that a DOD inkjet system has been incorporated into a microfluidic chip. (Xu and Attinger 2008) Ballistic microdrops differ, however, from microdrops in immiscible liquids by their evolution in a low friction environment, their higher speed of several m/s and the possibility of precise drop deposition on solids or liquids without disintegration. (see Section 4.2) Indeed, deposition of water and NaOH solution microdrops has been used in combination with X-ray microdiffraction to study the local structural evolution of biopolymers. (Rössle, Flot et al. 2003; Lemke, Burghammer et al. 2004; Schoeck, Davies et al. 2007)

Free falling microdrops in air can be thought as reaction vessels with volumes down to the pl-range. The reactants remain confined within the microdrops during their trajectory. Wall induced shearing effects do not play a role although mechanical compression of the solution during the ejection process can influence the structural integrity of fragile proteins; reviewed in: (Delaney, Smith et al. 2009).

The coalescence of free falling microdrops can in principle be used for kinetic studies (Riekel, Burghammer et al. 2004) in analogy to microfluidic mixers. (Ottino and Wiggins 2004) Microfluidic technology provides a mixing speed advantage (see section 4) but results in a dispersion of the reactants with distance from the mixing point. (Bringer, Gerdts et al. 2004)

Free falling microdrops are also of interest as carriers for nanoparticles or small biological objects in order to perform coherent X-ray diffraction imaging (CXDI) at the upcoming generation of free electron X-ray laser sources. (Chapman 2009)

I have explored in my thesis for the first time the combination of ballistic microdrops with stroboscopic X-ray microdiffraction techniques with the aim to develop techniques for studying the coalescence of two microdrops in flight. A particular challenge was to obtain stable coalescence conditions as previous demonstrations of microdrop coalescence could not be maintained sufficiently long for diffraction experiments. (Riekel, Burghammer et al. 2004) The production of a commercial microdrop coalescence system has been abandoned by Microdrop Technologies GmbH due to stability problems.[a]

The main instrumental effort was therefore to develop a stable setup with two inkjet heads allowing studying in-flight microdrop mixing at the ID13-BL using stroboscopic SAXS&WAXS techniques. I have used these techniques to study in-flight liquid paraffin wax and cytochrome C microdrops and the coalescence of cytochrome C with Na-acetate buffer microdrops. I have also performed exploratory WAXS experiments at the ID13-BL on paraffin wax microdrops deposited on surfaces and temperature-dependant diffraction on paraffin wax to calibrate the stroboscopic data. Static SAXS experiments were performed at the ID02-BL to obtain reference SAXS curves for the conformational states of cytochrome C solutions.

[a] Personal communication : B. Poulson, Microdrop Technologies GmbH

2 Diffusion de rayons X.

Ce chapitre décrit la principale technique d'analyses utilisées: la diffusion de rayons X.

Un faisceau qu'il grave sur un échantillon, interagit avec lui. Un des résultats possibles est la diffusion du faisceau incident. Elle peut être considérée comme une absorption de la radiation de la part de la matière et rayonnement suivant en toutes les directions. Comme la distribution angulaire du faisceau diffus dépend de la structure du champion considéré, au-delà que de la nature du faisceau et de sa longueur d'onde, ce phénomène est utilisé pour l'analyse structurale de la matière. La diffusion aux grands angles (WAXS) inclue la diffraction. Elle renseigne sur les structures amorphes et cristallines à l'échelle de liaison atomique (Å). La diffusion aux petits angles (SAXS) donne des informations sur la taille et la forme des structures étudiées à l'échelle de la molécule et de l'arrangement moléculaire.

Attention a été dédiée au traitement des données SAXS pour la normalisation et pour obtenir renseignements quantitatifs comme le rayon de giration ou qualitatifs, sur la conformation d'échantillon.

General background on X-ray scattering

2.1 Introduction

X-radiation (composed of X-rays) is a form of electromagnetic radiation with wavelength in the range of 0.01 to 10 nm. The continuous synchrotron radiation (SR) spectrum is often separated into "soft X-rays" and "hard X-rays" by the cut-off of a Be-window which separates the ultra-high vacuum of a synchrotron radiation storage ring from the beamline environment (vacuum or air). This cut-off is situated at an approximate wavelength of $\lambda \sim 0.4$ nm. My thesis work has been principally done at a wavelength of $\lambda = 0.97$ nm, i.e. in the "hard" X-ray part of the SR-spectrum.

2.2 Interactions of X-rays with matter

The basic interaction of X-rays with matter is through an excitation of the electrons surrounding the atoms which resonate at the same frequency as the incident radiation and emit coherent secondary waves. X-rays can interact elastically and inelastically with matter. Diffraction experiments reported in my thesis correspond to elastic interactions. X-ray elastic scattering is related to an electron density modulation which can be local (e.g. isolated molecules in solution) or periodic (lattice).

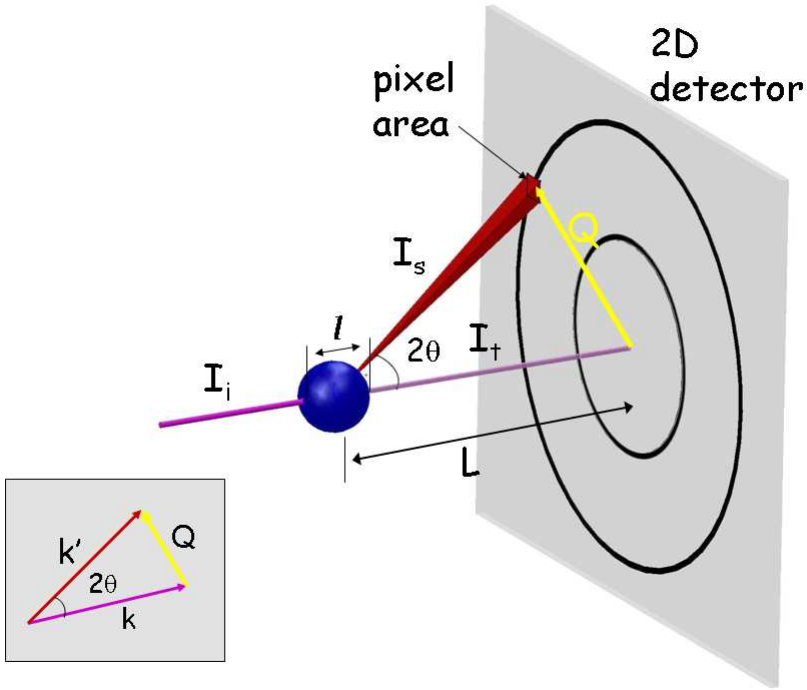

Figure 2.1 Schematic X-ray scattering setup. The inset shows a vector diagram of the elastic scattering process; ***k*** *and* ***k'*** *are the reciprocal vectors of the incoming and scattered beams,* ***Q*** *is the scattering vector*

An X-ray scattering setup is shown schematically in Figure 2.1. The monochromatic X-ray beam impinges on the sample and the scattered intensity is recorded in the forward direction

by a two dimensional detector. The number of photons scattered is determined as function of scattering angle (2θ). The scattering process as a vector diagram is shown in the inset of Figure 2.1. **k** is the vector of the incoming photon beam ($|\mathbf{k}|=2\pi/\lambda$) and **k'** the vector of the outgoing photon beam. The scattering vector **Q** is also called "momentum transfer vector" in neutron scattering.(Bacon 1975) Momentum conservation requires that:

$$\boldsymbol{p} = \hbar\boldsymbol{k} - \hbar\boldsymbol{k}' = \hbar\left(\boldsymbol{k}' - \boldsymbol{k}\right) = \hbar\boldsymbol{Q} \tag{1}$$

and

$$|\boldsymbol{Q}| = \frac{4\pi}{\lambda}\sin\theta \tag{2}$$

Given a flux of X-rays with intensity I_i, impinging on a sample of thickness l, the scattering intensity (I_s) recorded by the detector element subtending the solid angle ΔΩ is:

$$I_s = I_i\ \varepsilon\ T\ \Delta\Omega\ l\frac{d\Sigma}{d\Omega} \tag{3}$$

where ε is the detector efficiency, T the sample transmission and dΣ/dΩ the scattering cross section of the sample for volume unit (Lindner 2002; Narayan 2008). The last quantity characterizes the interactions between the incident X-rays and the sample. The solid angle (ΔΩ) is related to the area of the pixel detector (p_1p_2) and the distance sample-detector (L):

$$\Delta\Omega = \frac{p_1 p_2}{L^2} \tag{5}$$

The sample transmission (T), is defined as the ratio between the transmitted (I_t) and the incident (I_i) intensity:

$$T = \frac{I_t}{I_i} = \exp(-\mu l) \tag{6}$$

where μ is the linear adsorption coefficient and l is the thickness of the sample. If the scattering element comprises n components, the total transmittance is:

$$T = \prod_n \exp(-\mu_n l_n) = \prod_n T_n \tag{7}$$

2.3 X-ray scattering from crystalline solids

The scattering process in a crystalline solid is shown schematically in Figure 2.2. In this case lattice planes with distance d are populated by atoms with a constant interatomic distance. The phase difference between the scattered waves depends on the X-ray path difference from the different lattice planes:

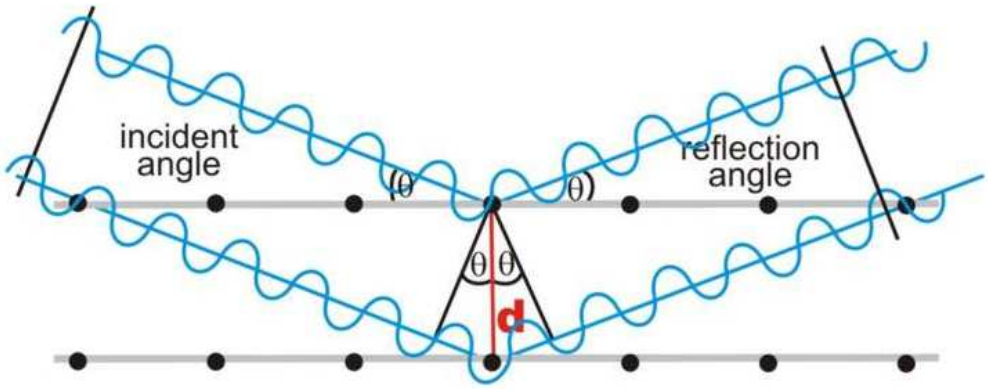

Figure 2.2 Scattering and interference from planes populated by atoms with constant distances

If the difference of the X-ray pathway length is equal to an integer number (n) of the wavelength (Bragg condition) then the interferences between scattered waves are constructive as in Figure 2.2. In a crystal, the atoms are strictly ordered in a repetitive way along the three axes of the crystal. Therefore, the difference in the pathway length is repeated along each of these axes and the addition of these constructive interferences gives rise to intense peaks at the observation point called Bragg reflections. In practice, when a Bragg reflection is observed, knowing the wavelength and the reflection angle 2θ, it is possible to calculate a characteristic repetitive distance d inside the crystal by the Bragg equation:

$$n\lambda = 2d \sin\theta \quad (8)$$

and

$$d = 2\pi/Q \text{ (see Eq.2)} \quad (9)$$

In the case of a crystal, the unit cell is the smallest entity which is sufficient to describe the whole structure. It is delimited by three unit vectors, **a**, **b** and **c**, which lengths and directions depend on the structure. The macroscopic crystal is assembled from this unit cell through a 3D translational symmetry. The characteristic distances (d) inside the crystal are combinations of these three unit vectors. Each Bragg peak corresponds to a characteristic distance. For disordered materials the differences in the X-ray pathway lengths are more variable, and consequently the scattering intensity is more diffuse.

Bragg's equation (Eq.3) corresponds to an *universal reciprocal law* of diffraction which implies that small real space dimensions give rise to large diffracting angles (2θ) and vice versa. In practice objects with small interatomic distances such as inorganic materials scatter at large angles (**wide-angle X-ray scattering**; **WAXS**) while large objects like proteins scatter at small angles (**small-angle X-ray scattering**; **SAXS**). In synchrotron SAXS

experiments the Q-range covered can be three orders of magnitude, typically 0.006 nm^{-1} < Q < 6 nm^{-1} corresponding to real space dimension of about 1 μm down to 1 nm.

2.4 Small-angle X-ray scattering (SAXS)

The analysis of SAXS patterns provides information on the size and shape of molecules in solution as well as on the large-scale organization of materials. (Baruchel, Hodeau et al. 1993) The scattered intensity I(Q) for monodisperse molecules in solution can be written as:

$$I(Q) \propto \Delta^2 * P(Q) \qquad (10)$$

with Δ the electron density difference contrast factor (≡Δρ) and P the molecular form factor. For interacting particles an interference term -structure factor: S(Q)- has to be introduced:

$$I(Q) \propto \Delta^2 * P(Q) * S(Q) \qquad (11)$$

Since macromolecular dimensions are large compared to the X-ray wavelengths, the corresponding angular range of observable scattering is small. In the case of solution scattering, the 2-dimensional (2D) SAXS pattern is isotropic and can be azimuthally averaged over 360 ° to a 1-dimensional (1D) SAXS profile.

Guinier-Plot - Radius of gyration. The analysis of the solution scattering patterns of a protein molecule allows getting information on its size via the determination of the radius of gyration (R_g).(Guinier and Fournet 1955; Glatter and Kratky 1982)

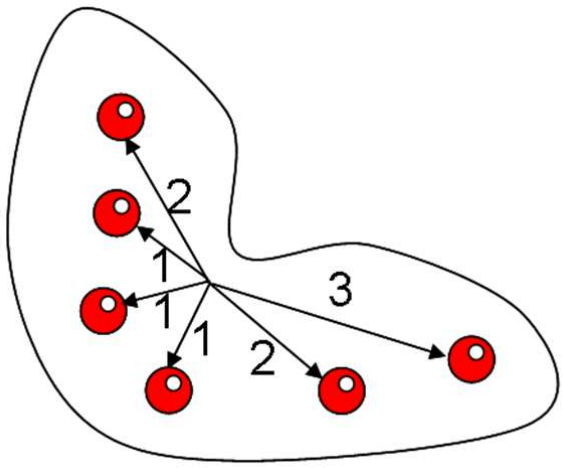

Figure 2.3 Determination of radius of gyration -R_G

R_g corresponds to the square root of the average squared distance of each atom from the centre of the molecule. For the example shown in Figure 2.3 one obtains:

$$R_g = \sqrt{(1^2 + 1^2 + 1^2 + 2^2 + 2^2 + 3^2)/6} = 1.82$$

The R_g value can be deduced from a SAXS pattern of a monodisperse dilute solution of this molecule using Guiniers law:

$$I(Q) = I_0 e^{-\frac{Q^2 R_g^2}{3}} \quad (12)$$

where I is the SAXS intensity. This law holds for $Q < 1/R_g$ and requires dilute solutions without interference between molecules. As shown Figure 2.4, the plot of ln(I) as a function of Q^2 (called Guinier plot) has a linear part. The slope S of this part is proportional to the square of R_g:

$$S = -1/3 * R_g^{0.5} \quad (13)$$

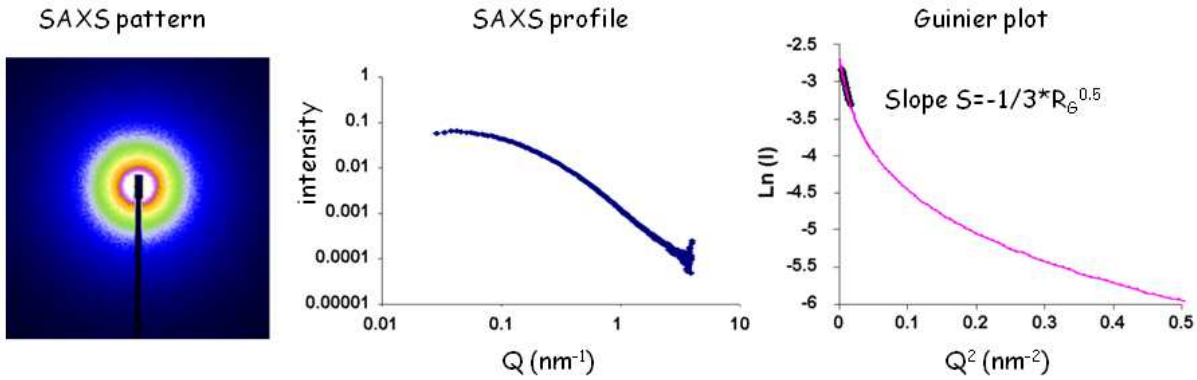

Figure 2.4 Solution SAXS pattern and Guinier analysis

An analysis of the SAXS profile also provides information about the shape of the molecule.(Svergun and Koch 2003)

Kratky plot. The SAXS pattern of a protein solution is sensible to the intermolecular interactions between distant parts of protein's chains which affect the statistics of distances between the scattering centres. A folded protein shows long range interactions between the chains while in the unfolded state only short range interactions remain. The small angle scattering of an *unfolded protein* in solution is well fitted by the "Debye function". It determines the small-angle scattering of a Gaussian distribution of segment density about a centre of mass characterized by a radius of gyration R_g (King 1999):

$$I(Q) = \frac{2(e^{-R_g^2 Q^2} + R_g^2 Q^2 - 1)}{R_g^4 Q^4} \quad (14)$$

A characteristic feature of the Debye function is its asymptotic Q^{-2} behaviour for high Q-values. Globular molecules follow instead Porod's law, for which the asymptotic value for high Q-values is Q^{-4}. A $I*Q^2$ versus Q plot (Kratky plot) is a convenient display of the compactness state of a protein. It is often used to monitor a folding process. (Grossmann 2002)

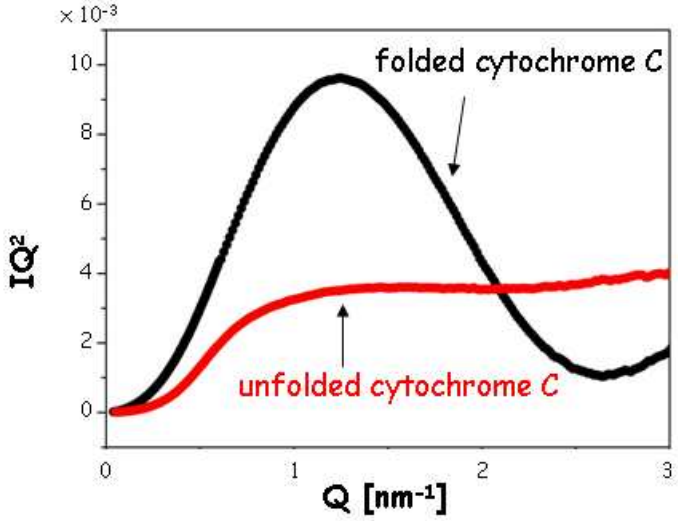

Figure 2.5 Kratky plots for folded and unfolded cytochrome C. The compact form of the folded molecule is reflected in the shape of the curve

2. Dynamique de repliement des protéines

Le processus de repliement des protéines est au centre du débat scientifique depuis presque quatre-vingts ans.

Les méthodes utilisées pour étudier ce processus consistent à perturber les conditions d'équilibre de la protéine afin de provoquer un changement de la conformation qui est suivi principalement par des techniques de diffusion ou de spectroscopie. Une des techniques utilisables est la diffusion centrale résolue en temps couplée aux techniques microfluidiques qui changent la nature du solvant par un mélange de la solution protéique avec des dénaturants ou des tampons de pH sélectionné. En raison du faible pouvoir de diffusion des protéines et des volumes utilisés, l'utilisation de rayonnement synchrotron est indispensable.

La mise en place d'expériences de micro-diffusion centrale stroboscopique pour suivre les changements de conformation de protéines à l'intérieur de micro-gouttes balistiques c'est une nouvelle approche développée dans le cadre de ce travail de thèse.

3. Protein folding dynamics

Denatured proteins, which have had essentially all of their native three-dimensional structure disrupted, can refold from their random disordered state into a well-defined unique structure, in which the biological activity is virtually completely restored. (Levinthal 1968) The *Levinthal paradox* observes that if a protein were to fold by sequentially sampling all possible conformations, it would take an astronomical amount of time to do so, even if the conformations were sampled at a rapid rate (on the ns or ps scale). Based upon the observation that proteins fold much faster than this, it is then proposed that a random conformational search does not occur, and the protein must, therefore, fold through a series of metastable intermediate states.

Understanding protein folding occurs is an old scientific problem that can be dated back at least seven decades, namely to the experiments of Anson and Mirsky in the 1930s.(Anson and Mirsky 1931) It is a fascinating subject because of the enormous number of degrees of freedom available to a polypeptide chain, the speed of conformational transitions and the structural intricacy of the native state (Creighton 1994). It is also of practical importance since it helps to predict structure from sequence, in the protein engineering design, and in understanding protein misfolding. (Jackson 1998)

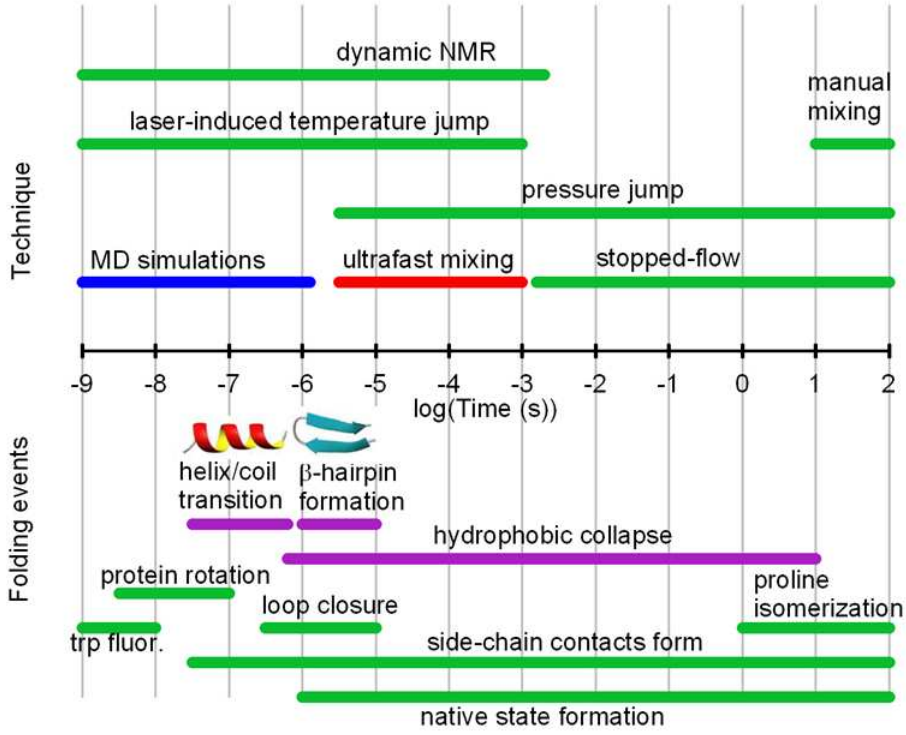

Figure 3.1 Timescales of protein dynamics and experimental techniques; (source: O. Bilsel, University of Massachusetts Medical School; web page: www.osmanbilsel.net/Home/microsecond-protein-folding-kinetics)

Important conformational changes occur on the time scale of ms and sub-ms. Several experimental techniques allow rapidly triggering the folding of a sample of unfolded protein, and then observing the resulting dynamics. An overview on protein dynamic and available experimental techniques is shown in Figure 3.1; see also: (Bartlett and Radford 2009).

The most common method for initiating protein folding or unfolding relies on mixing the protein with a buffer to achieve a rapid change in solvent conditions (denaturant, concentration, pH, etc). Since the protein is sensible to pressure and temperature changes, pressure and temperature jump methods are also used. Conformational changes can be coupled with photochemical events as well, such as the photolysis of a protein–ligand bond or photo reduction (Roder 1999). Each of these techniques has fundamental limitations such as mass diffusion in the case of rapid mixing, acoustic speed for pressure jump or thermal diffusivity for temperature jump.

Time resolved SAXS solution scattering is one of the main techniques to investigate protein folding kinetics. This technique gives information on the overall shape of the protein in solution (Glatter and Kratky 1982). It can therefore be useful to discriminate among theoretical folding models. Lattice simulations suggest that slow folding amino acid sequences collapse to compact structures (with non-native topologies) before folding, while fast folders collapse and fold simultaneously. The changes on the radius of gyration, obtained with SAXS experiments, give indications about the number of steps of the process.

High brilliance SR-sources allow experiments on nl-samples (Narayan 2008). The two main mixing techniques are stopped-flow(Panine, Finet et al. 2006) and continuous flow.(Pollack, Tate et al. 1999) Stopped-flow techniques are based on the repetitive filling of a vessel with solutions. SAXS patterns are accumulated until the necessary counting statistics has been reached. Time-resolutions of a few ms can be attained.(Weiss, Narayanan et al. 2005) Continuous-flow mixing experiments are usually done with microfluidics technology in order to reduce sample consumption.(Ottino and Wiggins 2004) The time resolution depends on the size of the X-ray beam (providing a positional resolution) and the spatial extent of the mixing zone.(Pollack, Tate et al. 1999; Pollack, Tate et al. 2001; Akiyama, Takahashi et al. 2002; Dootz, Evans et al. 2007) The spatial extent of the mixing zone can be reduced by turbulent mixing. (Akiyama, Takahashi et al. 2002) Indeed, time resolutions of a few 10^{th} of μs have been reached for turbulent mixing combined with SAXS.(Akiyama, Takahashi et al. 2002) Experimental results on cytochrome C folding kinetics are collected in Annex D.

The use of stroboscopic SAXS to follow cytochrome C conformational changes inside ballistic microdrops is a new approach developed during this thesis work.

4. Jets d'encre technique

Dans ce chapitre, le système à travers lequel les gouttes sont produites, jets d'encre goutte à la demande, est décrite. Les forces physiques qui en règlent les propriétés, sont décrites. L'attention est focalisée sur l'énergie superficielle qui en détermine la forme et qu'il permet la coalescence en vol de deux gouttes ou l'impact sur surfaces sans éclaboussement. La compétition entre cette énergie superficielle et l'énergie cinétique est aussi responsable des oscillations atténuées qu'ils caractérisent l'impact entre gouttes ou avec des substrats. Finalement l'influence de frottement de l'air sur la vitesse des micro gouttes, est analysée.

4. Inkjet Technology

4.1 Introduction

Inkjet systems have found multiple applications in various domains of science and technology.(Lee 2003; Gans, Duineveld et al. 2004; Burgold, Weise et al. 2005) For applications in fundamental science, ballistic microdrops can be considered as wall-free compartments with a surface energy barrier. This is of interest if physical wall-effects such as nucleation sites or shearing effects are to be avoided.

4.2 Generation of microdrops(Lee 2003)

The different technologies used for microdrop generation are reviewed in: (Lee 2003; Burgold, Weise et al. 2005). The technology used in the present work consists of a glass capillary surrounded by a piezoelectric transducer (also called *dispenser head*). One end of the capillary forms a nozzle (diameter 30 to 100 μm) the other is connected to a reservoir. (Figure 4.1)

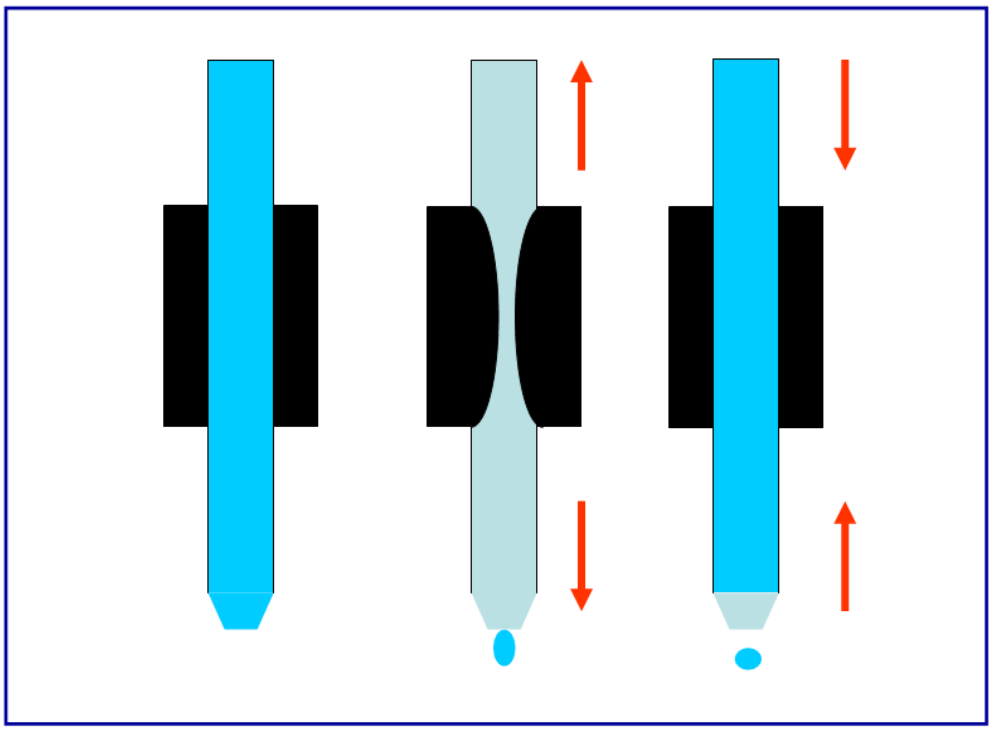

Figure 4.1 Schematic design of microdrop generation by compression of a capillary by a piezotransducer

The piezo contracts (expands) when a positive (negative) voltage is applied to it and thereby squeezes (relaxes) the tube. This process creates a pressure wave that accelerates the liquid. A small liquid column leaves the nozzle, breaks off and forms a droplet.(Badie and Lange 1997;

Basaran 2002; Xu and Basaran 2007) Depending on the nozzle interior diameter, volumes between 25 to 500 pl are generated. The microdrop is ejected with speed ν.

4.3 Microdrop properties

The basic equations for free falling microdrops ν are as follows:

Volume	$V=4/3\pi r^3$	(1)
Surface	$A=4\pi r^2$	(2)
Surface Energy	$E_{sur} = \sigma A$	(3)
Kinetic Energy	$E_{kin} = (2/3\rho\pi)\nu^2 r^3$	(4)
Ratio E_{kin}/E_{sur}	$(1/6\ \rho/\sigma)\nu^2 r$	(5)

with σ: surface tension, r: microdrop radius, ρ: density. ν: speed

At the surface of a microdrop the molecules experience an unbalanced attractive force towards the bulk due to lack of neighbours on the external side of the microdrop surface. As a consequence a fluidic object will tend to minimize the surface area into a sphere in order to minimize the surplus of surface energy. (Figure 4.2A) E_{kin}/E_{sur} becomes <1 for a microdrop radius of less than ~100 μm. (Figure 4.2B) The impact behaviour of microdrops of such dimensions with several m/s speed is dominated by their surface energy.(Lee 2003) This has the practical consequence that microdrops do not splash upon impact. (Figure 4.2A)

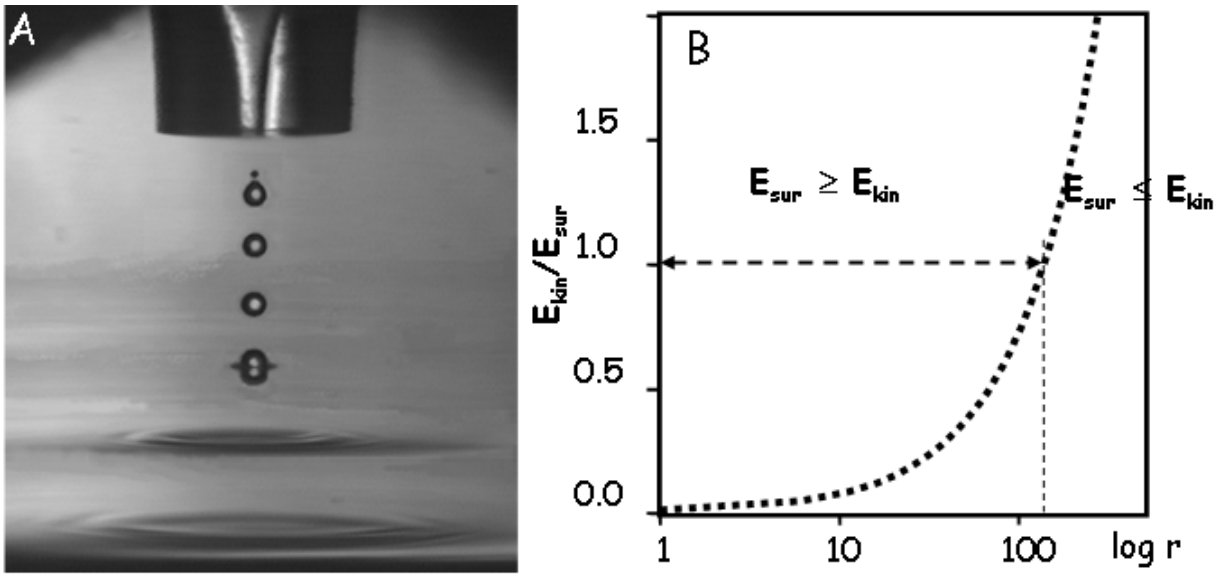

Figure 4.2A: Ballistic microdrops ejected from inkjet head under stroboscopic illumination. (courtesy Microdrop Technologies GmbH); B: calculated ratio E_{kin}/E_{sur} for water microdrops with 2m/s speed and radius r (courtesy M. Roessle; EMBL-Hamburg)

I used for my thesis work microdrops with a typical diameter of 80 μm and a speed of $v \leq$ 2m/s. The evolution of such a free falling microdrop is determined by the viscous resistance of air defined by Stokes's law:

$$F_{Stokes}=6\pi\eta r v \qquad (6)$$

where η is the viscosity of air. This implies that the microdrop speed is reduced as a function of distance from the inkjet head and a calibration has to be performed. The practical travel range of a microdrop from the inkjet head to a target can be estimated from its terminal velocity and its relaxation time, which is a measure how fast the motion of the microdrop reaches a steady state after ejection.(Lee 2003) The terminal velocity is calculated by setting the gravitational forces on the microdrop equal to the velocity dependent drag forces. For a 75 μm diameter microdrop the terminal speed is calculated from Stoke's law as 0.17 m/s.(Lee 2003) The relaxation time τ can be calculated from:

$$\tau=(1/18)(d^2/\eta)\rho \qquad (7)$$

For a 75 μm diameter microdrop one obtains τ=17 ms (Lee 2003). This implies that inkjet systems with ejection speeds of a few m/s can operate only in the range of several 10^{th} of mm.

4.4 Microdrop coalescence

The coalescence (mixing) of microdrops is shown in Figures 4.3A,B. Stroboscopic light operating at the frequency of the microdrop ejection allows seeing the shape of the drops while continuous light makes the trajectories of the drops visible. It can be seen that the shape of the microdrop after coalescence is affected by oscillations.

Consider two microdrops of equal mass and speed arriving at the collision point with moments of equal magnitude: $|\mathbf{p}_1|=|-\mathbf{p}_1|$. (Figure 4.4) The interaction of the colliding microdrops with the viscous drag of the surrounding medium and induced motions inside the microdrops will be neglected. The total momentum of the two microdrops is conserved in the collision. As the horizontal momentum components ($\mathbf{p}_h$) of the microdrops are opposite, the resulting momentum -$\mathbf{p}_c$- corresponds to $\mathbf{p}_c=2*\mathbf{p}_v$ and the combined entity moves into the vertical direction. The speed of the combined entity is assumed to be equal to the speed of the individual microdrops before the collision in order to avoid acceleration or deceleration effects. This imposes that $|\mathbf{p}_1|=|-\mathbf{p}_1|=2*|\mathbf{p}_h|$ and therefore an angle of 60^0 between the trajectories of the two microdrops which is close to values used in practice. (Figure 4.3)

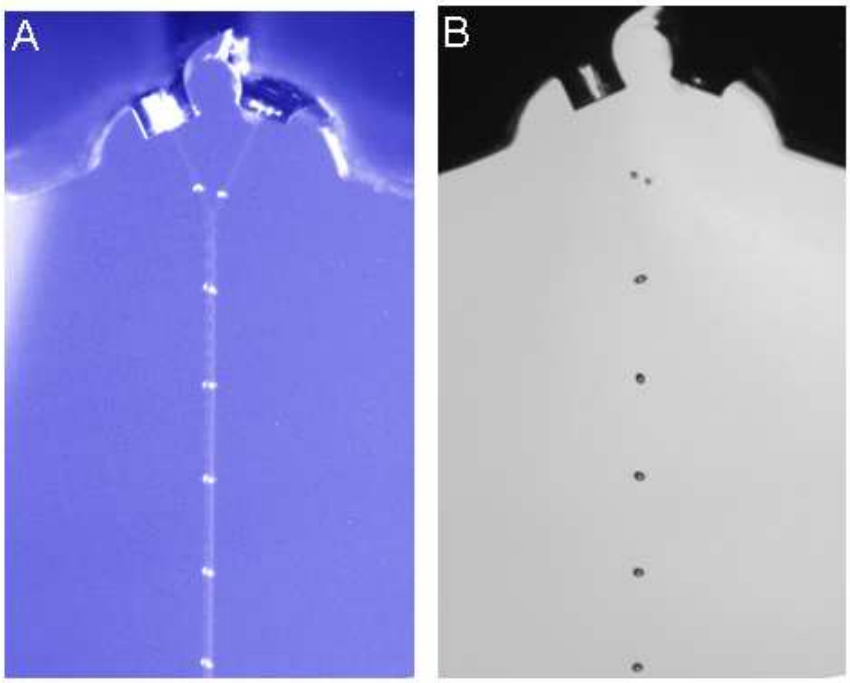

Figure 4.3 Stroboscopic images of microdrop imaging. The microdrop ejection and LED illumination are triggered at the same frequency. A: overlap of stroboscopic LED illumination and illumination by continuous light. The sensitivity of the digital camera allows visualizing the drop trajectory. The oscillations are associated with the dissipation of excess kinetic energy in the coalescence. B: stroboscopic LED illumination showing more clearly the microdrop shape evolution after coalescence.

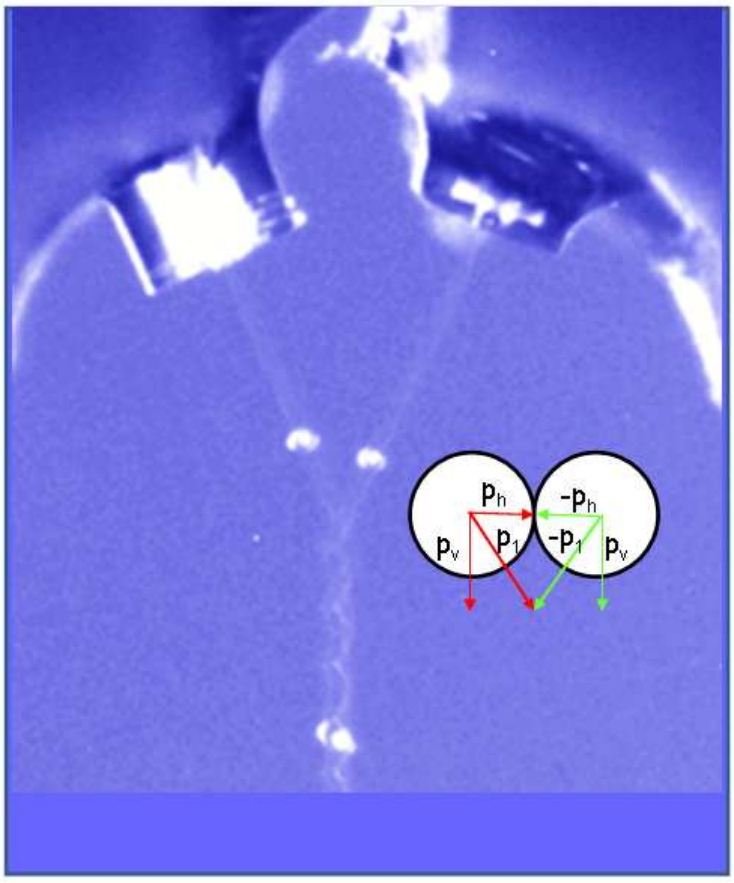

Figure 4.4 Schematic vector diagram of microdrop momentum at the collision point.

The collision of the two microdrops is inelastic as only the momentum is conserved and the horizontal components of the kinetic energy are transformed into a deformation of the microdrops. Damped oscillations occur until the excess kinetics energy is dissipated. This is also observed for a microdrop impact on a solid, wetting surface.(Kim, Park et al. 2003) The microdrop doesn't break up because the gain in surface energy is bigger than the kinetic energy. A restoring force towards the centre of the drop is acting and the liquid is squeezed so that it undergoes stretching and compression phases. The shape of the microdrop at the end of the process will be spherical to minimize the surface energy.

The natural oscillation frequency for a liquid microdrop surrounded by a gas medium of much lower density is given by:(Clift, Grace et al. 1978; Fukai, Zhao et al. 1993)

$$f_N = \left(\frac{16\gamma}{\pi^2 \rho d^3}\right)^{1/2} \qquad (6)$$

where d is the droplet diameter, γ the surface-tension coefficient and ρ the liquid density. For water γ=0.073 N/m and ρ=1000 kg/m^3, f_N=3 kHz.

Accessible time scales: The lower limit of accessible time scales is determined by the coalescence time of two microdrops and will be experimentally studied in this work. The upper limit of time scale accessible to microdrops is defined by their path length and flight time in air. For aqueous microdrops with ν=2m/s and a practical flight range of about 10 mm limited by air drag(Lee 2003), the upper limit of accessible time-scales is approximately 5 ms.

5. Matériels et Méthodes

Ce chapitre est consacré à l'illustration de l'instrumentation utilisée.

Pour effectuer des expériences de diffusion sur de microgouttes balistiques il est nécessaire de disposer d'un jet d'encre synchronisés, produisent de gouttes avec une dimension prédéterminée et avec des trajectoires reproductibles, un faisceau de rayons X à la haute intensité (rayonnement synchrotron) de dimension compatible avec la dimension des gouttes (micrométrique) et un détecteur sensitif. Un système de jets d'encre avec cette caractéristique, été intégré dans la ligne de lumière ID13 à ESRF, qui normalement opère avec un faisceau de rayons X de 1 μm.

L'émission des gouttes est synchronisée avec l'activation d'un diode électroluminescente pour leur visualisation voie un microscope; en fixant un retard entre les deux événements, il est possible de visualiser les gouttes en différents points de la trajectoire. L'acquisition du signal de diffusion des rayons X de la part du détecteur est synchronisée avec le passage des gouttes devant le faisceau pour minimiser lu signal de l'air.

Le FReLoN CCD détecteur a été initialement utilisé pour l'acquisition des données. Cette opération a été synchronisée par l'activation de la galette de microcanaux. Successivement le FReLoN CCD a été remplacé par le Medipix. Dans ce cas les opérations stroboscopiques sont imposées par l'activation des pixels.

La dernière partie du chapitre s'occupe de la modalité de traitement des données SAXS. Ils ont été normalisés pour le temps d'acquisition, pour l'intensité du faisceau incident et pour la longueur du chemin de faisceau à l'intérieur de la goutte.

5. Materials & Methods

5.1 Materials

White paraffin wax (*purissime*) with a specified setting range of 50-61 ^{0}C was obtained from Riedel de Haën. Cytochrome C (cyt c) with 13 kD molecular weight was obtained from Aldrich. All solutions were prepared using deionised water. Cytochrome C solutions were prepared via dialysis using a membrane filter with 3.5 kD cut-off. 1.5 mM cytochrome C solutions were dialyzed in 0.01 M HCl (pH 2) or in 0.17 M Na-Acetate buffer (pH 5.5). 4 mM cytochrome C solution was prepared via dialysis against 0.01 M HCl (pH2). After dialysis the cytochrome C solutions were diluted to the required concentration and pH with Na-acetate buffer or with 0.01M HCl. The minimal cytochrome C concentration was 0.2 mM. The table 5.1 shows the solutions concentration used. Further details are reported in Section 6.2.2.

[cyt c] (mM)	[NaAc] (mM)	pH
4	0	1.96
3.5	23.5	
3	47	
2.5	70.5	
2	94	4.9
1	141	
1.5	0	2
1	0	2
1.5	170	5.5
0.5	85	4.5
0.2	0	2

Table 5.1. Concentrations of solutions used for static experiments on ID02 BL.

5.2 ESRF beamlines used

Experiments on paraffin wax and all stroboscopic experiments were performed at the ID13 beamline. Static SAXS experiments on cytochrome C solution were performed at the ID02 beamline. More details on both beamlines are reported in Annex A.

5.3 Stroboscopic SAXS/WAXS experiments

5.3.1 Introduction

Microbeam SAXS/WAXS patterns of polymers and biopolymers require data collection times from a few ms up to a few sec at the ESRF-ID13 beamline.(Riekel 2000) I have been using ballistic microdrops of 70-80 μm diameters, ejected with a speed of about 2 m/s and a maximum frequency of 2 kHz. Such microdrops will transit a 1 μm SR-beam in 40 μs. The

detector would collect only air scattering during 460 μs for every period of typically 500 μs. This implies that stroboscopic data acquisition techniques have to be used to minimize background scattering and obtain patterns with sufficient statistics.

The following instrumentation is required for stroboscopic SAXS/WAXS experiments:

- A DOD inkjet system for the production of microdrops with a predetermined size and with spatially and temporally controlled trajectories
- a SR microbeam compatible with the size of microdrops
- the integration of the DOD inkjet system (also called microdrop generator) into the SR beamline environment
- a sensitive detector which can be triggered

5.3.2 DOD inkjet setup & control system

I have been using during my thesis separate commercial DOD inkjet systems for room temperature and high temperature operation by *Microdrop Technologies GmbH*.[b] The components of the DOD inkjet system used for room temperature work on aqueous solutions are shown in Figure 5.1.

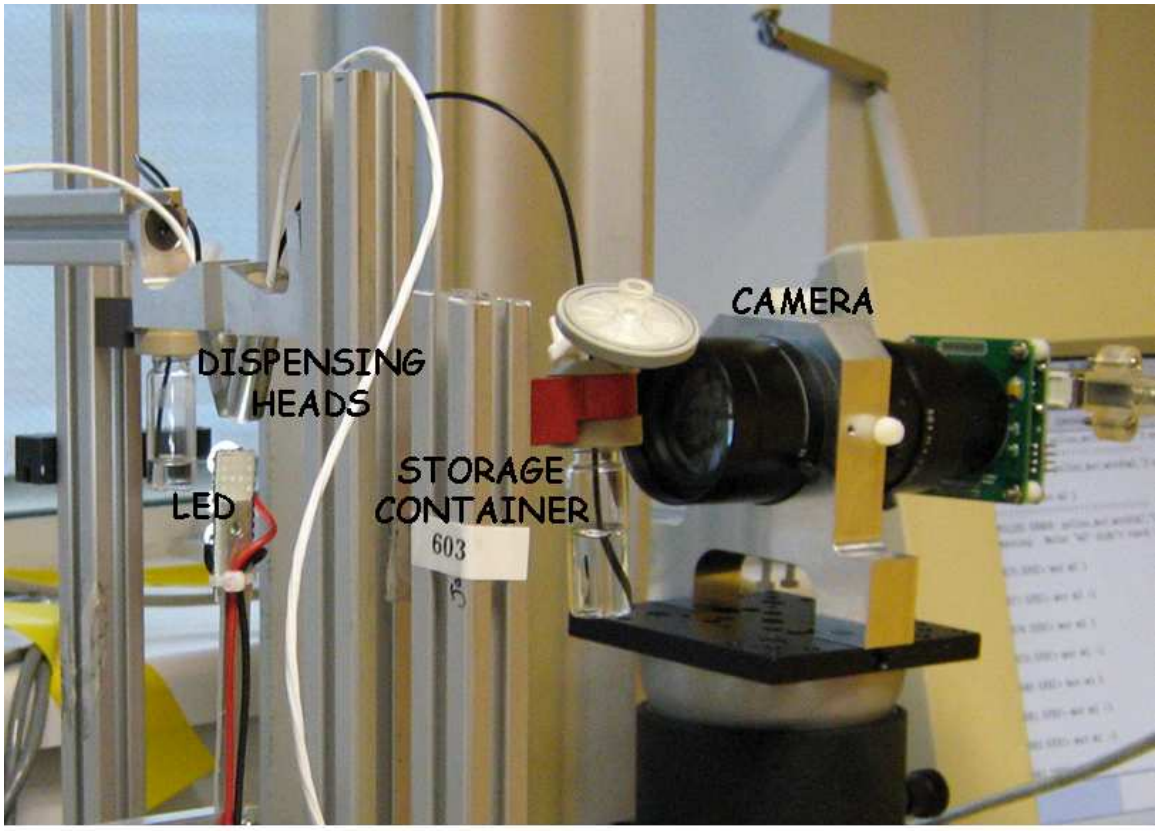

Figure 5.1 DOD inkjet set-up installed in ID13 laboratory.

[b] www.microdrop.de/

The master of the stroboscopic data acquisition is an OPIOM, "multi-purpose digital input/output" NIM module, developed at ESRF.[c] The triggering by the OPIOM module synchronizes:

- the Dispenser-Drive-Unit (DDU) enabling the piezo contraction (and therefore microdrop ejection)
- the Light Emitting Diode (LED) activation to visualize the frozen microdrops by a microscope
- the detector front-end activation to minimize air scattering

A schematic picture of the DOD control system with a stand-alone DDU and a pixel detector is shown in Figure 5.2A; adapted from: (Graceffa, Burghammer et al. 2009). This DDU version, with manually selected parameters, was initially used. The Figure 5.2B shows the modular DOD control system driving two dispenser heads, to realize microdrops mixing in flight. The DDU-parameters are set by computer control. Details of the triggering system are shown in the pictures 5.3A/B. A scheme of the stroboscopic operation involving all triggered devices is shown in Figure 5.4.

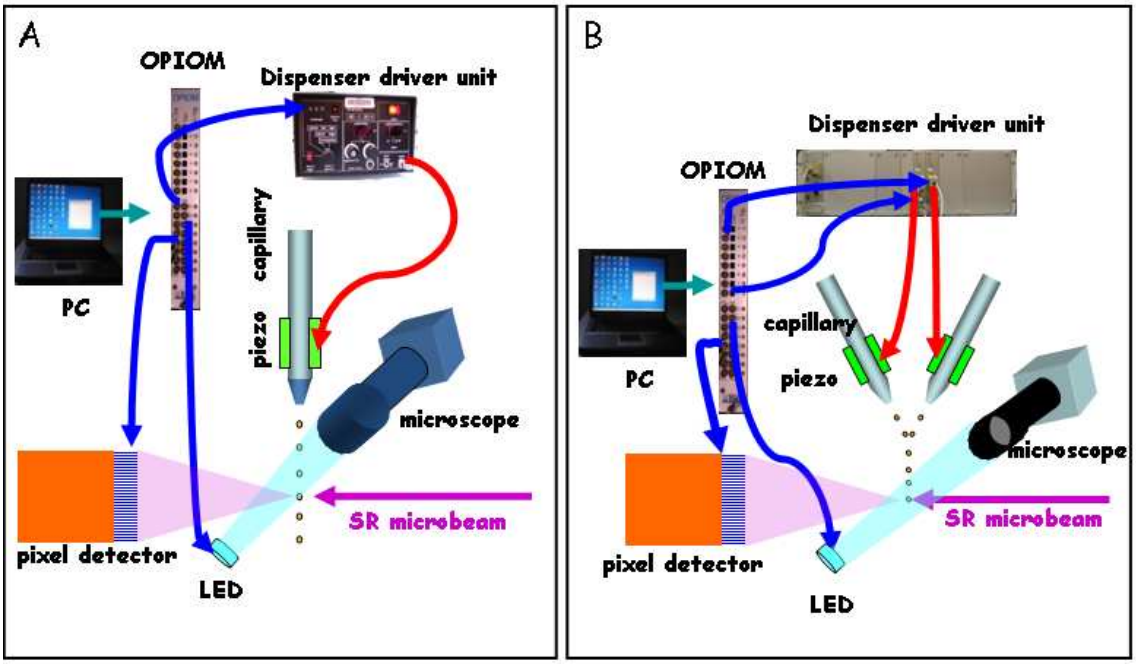

Figure 5.2 A: Schematic design of microdrop triggering module acting on a stand-alone DDU, LED and pixel detector. The DDU triggers the piezo of the inkjet capillary; B: microdrop triggering system with modular DDU unit controlled by a PC. Two inkjet heads are driven by the DDU modules.

[c] www.esrf.fr/UsersAndScience/Experiments/TBS/ISG/opiom

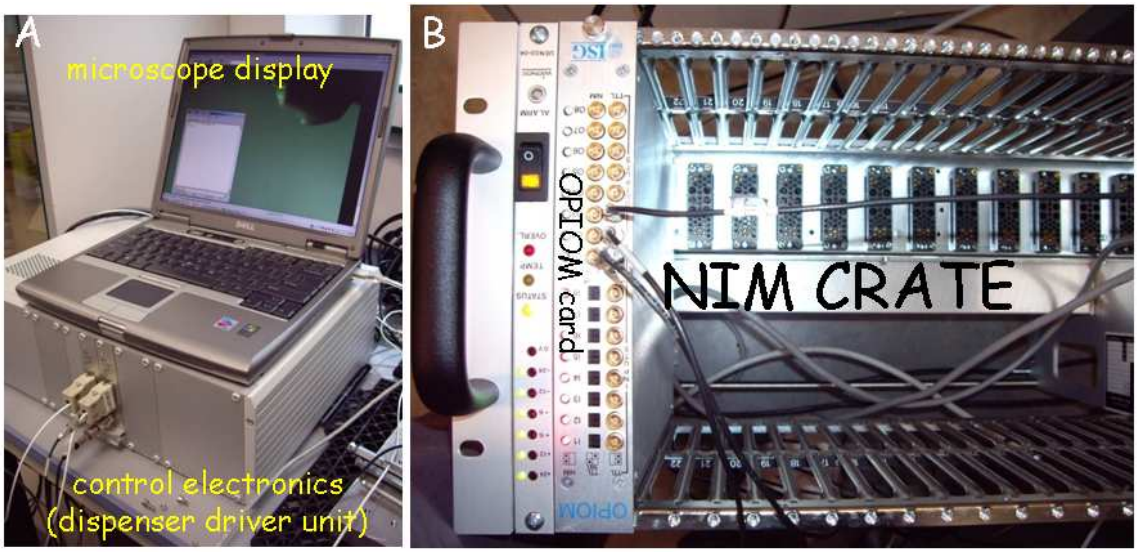

Figure 5.3 A: modular microdrop control unit comprising DDU and laptop for microscope display; B: NIM crate with OPIOM card used for triggering

The OPIOM module generates pulse signals of user-defined period and pulse width. The wave signal has a saw tooth shape with values of 0 or 1. When the value is 1 the electrical output channel is activated, i.e. the electronics driver is activated, the LED is illuminated and the front-end detector is acquiring a signal. It is possible to set a delay between microdrop generator and the LED illumination. Furthermore, the OPIOM module can set a delay between two dispenser heads. It allows mixing processes between microdrops arriving with different speed.

The working frequency of about 1 KHz does not require a synchronization of the microdrop generator with the intrinsic pulsed structure of the SR beam.[d]

[d] Photon pulse separation in single bunch operation: 2.8 μs and smaller depending on bunch sequence

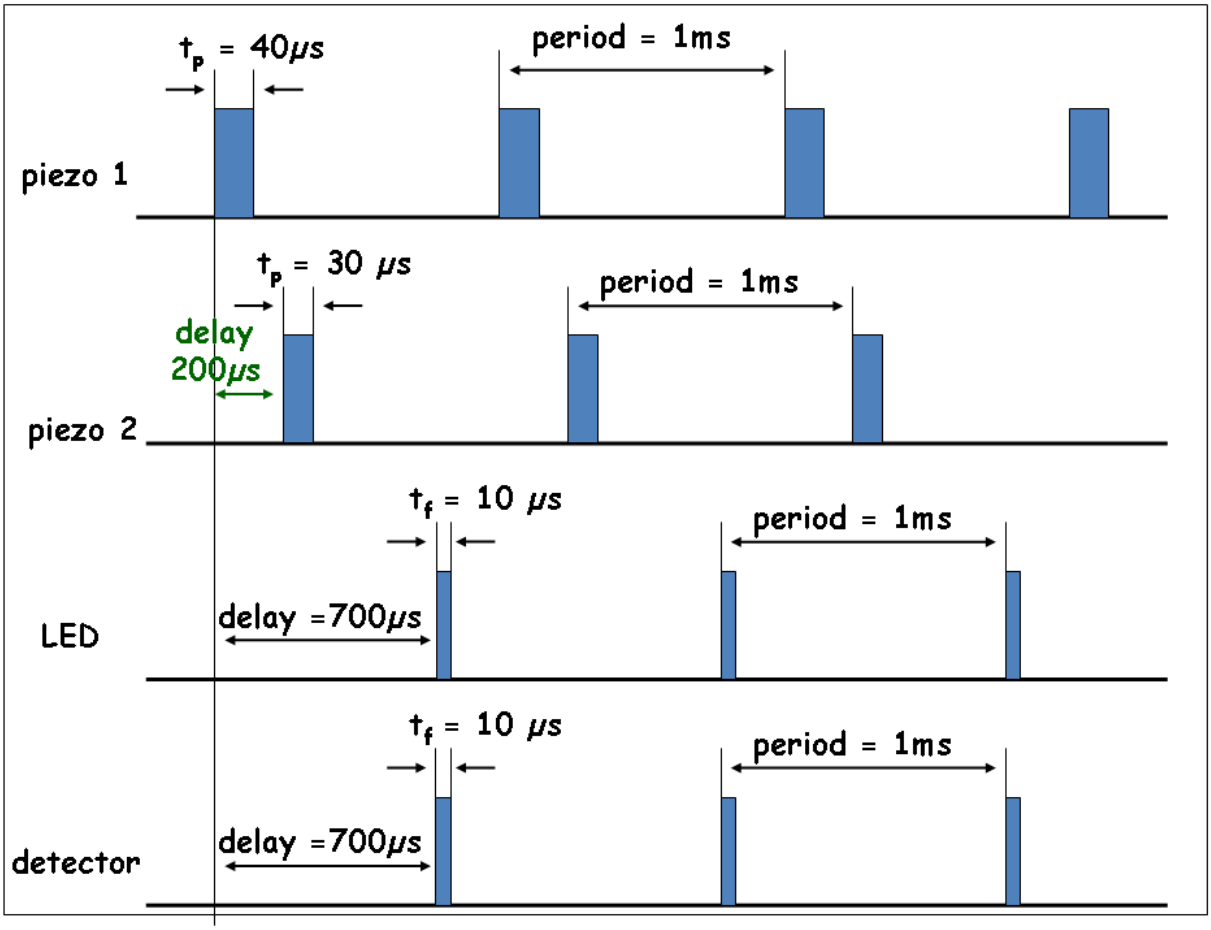

Figure 5.4 Triggering operation of devices used for stroboscopic SAXS experiments with typical times. The triggering period is determined by the OPIOM module. In order to match the drop ejection by the two capillaries, a delay of 200 μs has been imposed between the two piezo-transducer pulses. The delay of 700 μs between the first piezo-transducer pulse and the detector/LED activation is required to observe an ejected drop at a specific time. (t_p: piezo-transducer activation period; t_f: framing, i.e. activation time of LED and pixel detector)

5.3.3 High temperature DOD setup

A high temperature DOD setup was used for test experiments on paraffin wax. (see Section 6.1) Ballistic paraffin microdrops of 70 μm diameter (about 180 pl) were generated by a special DOD system from *Microdrop Technologies*. The temperature of the glass capillary (T_1) and the reservoir (T_2) could be defined independently with $T_1>T_2$ in practice. The connecting part between capillary and reservoir was kept at T_2. A constant negative pressure of a few mb is maintained at the reservoir in order to facilitate microdrop ejection. The temperature of the storage container and the glass capillary heating element was kept constant at T_2=360±2 K. A picture of the set-up installed in ID13 laboratory is shown in Figure 5.5. The control of the electronics was identical to the room temperature DOD system.

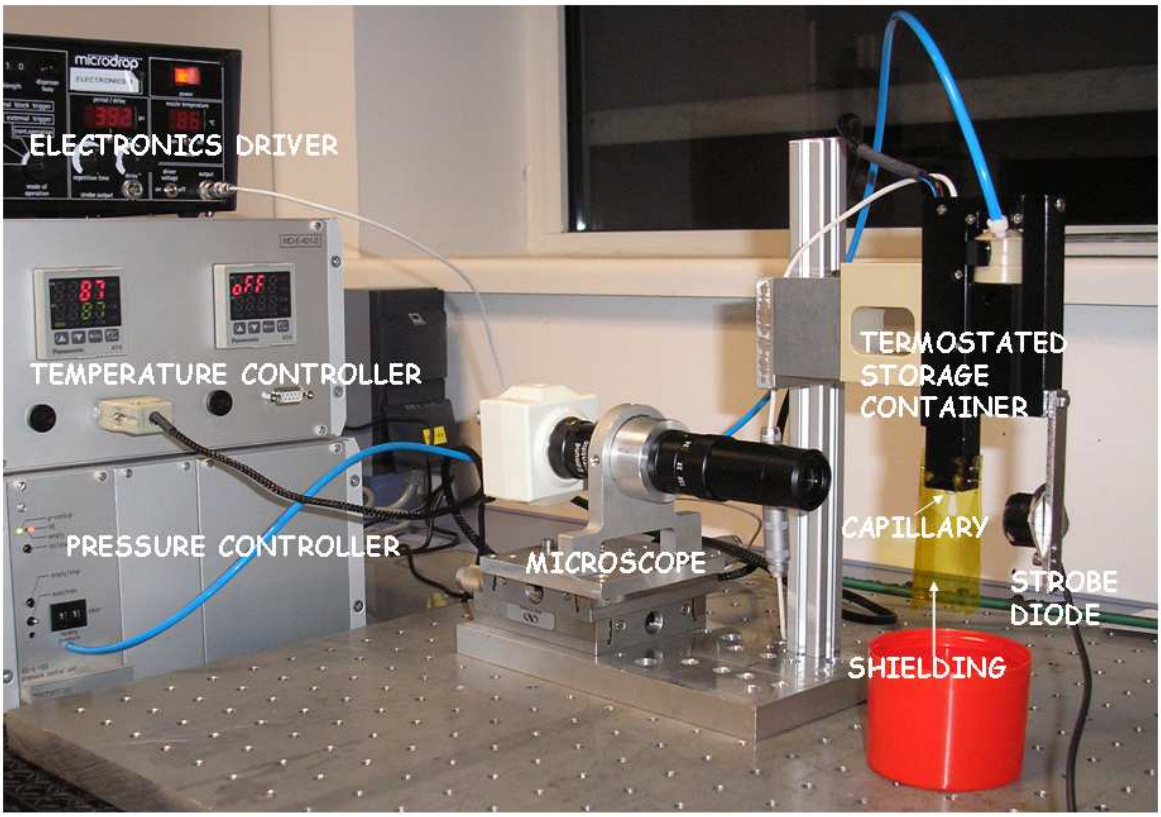

Figure 5.5 DOD high temperature inkjet set-up installed in ID13 laboratory.

5.3.4 Control parameters for the piezo-transducer

The voltage waveform used to drive the piezo-transducer is a square wave. In Figure 5.6 a typical control impulse is shown, as measured by an oscilloscope. The pulse-width defines the applied impulse length. The parameters which can be controlled are the level and the width of the voltage pulse (t_p). The level determines the amount of pressure created and thus the acceleration of the liquid in the nozzle and the speed of the drops.(Xu and Basaran 2007)

In practice the required voltage parameters depend on several factors such as the viscosity of the liquid, the capillary nozzle inner diameter, the quality of the piezo-transducer and the connection of piezo-transducer to capillary. Each dispenser head has its own characteristics, so that individual voltage and pulse-width values are required for the same liquid. The volume and the speed of the microdrops depend on these parameters. Microdrops generated by different dispenser heads have therefore different speeds which have to be matched for drop collision experiments (see below). The ejection frequency is regulated by the OPIOM module.

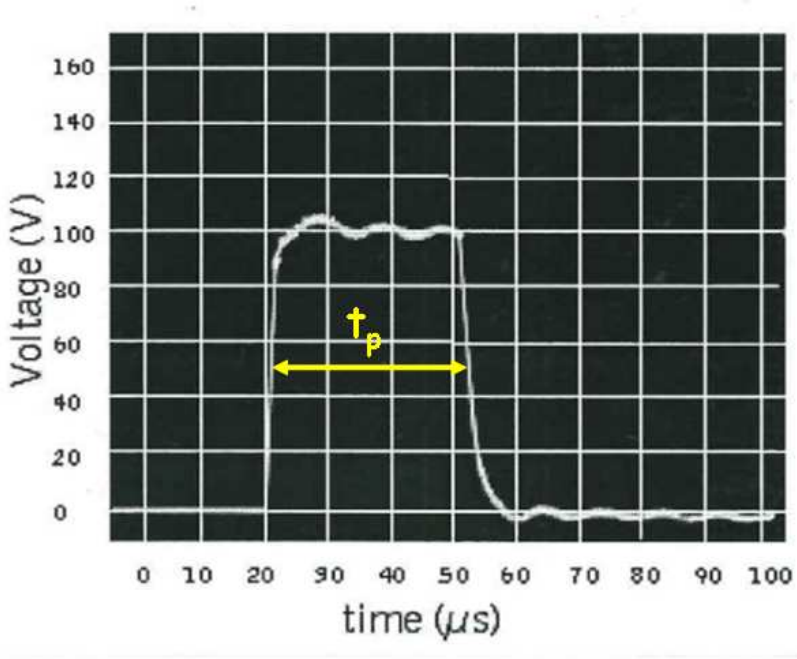

Figure 5.6 Oscilloscope trace of voltage pulse with width t_p used to drive the piezo-transducer during microdrop generation.

5.3.5 Microdrop visualization

The microdrops are visualized by a CCD camera attached to a microscope. Using a conventional source of light it is barely possible visualizing the trajectory of the microdrops ejected at a frequency of 2 KHz (period 0.5 ms) with t_p=40 μs. (Figure 5.7A) This effect is analogous to the blurring observed when imaging a fast moving object with long exposure times. In order to visualize the microdrops at a speed of about $v \sim 2$ m/s, a stroboscopic illumination by a LED is required. The OPIOM module has fixed the frequency of the LED, the frequency of the piezo contraction and the framing time at 10 μs, for this example. (Figure 5.7B) A schematic picture of the corresponding triggering sequence is shown in Figure 5.7C.

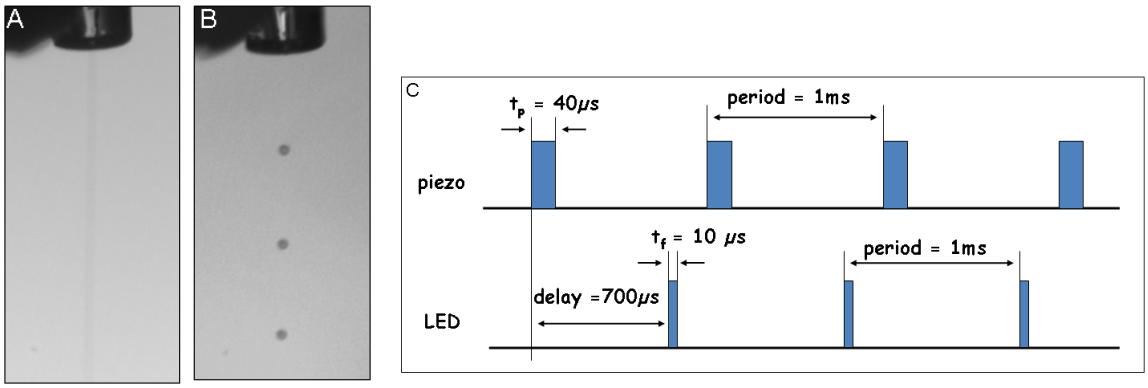

Figure 5.7 Microdrops pictures made with a CCD camera attached to a microscope. A: conventional light illumination; B: LED illumination; C: stroboscopic operation corresponding to B.

The blurring induced by an increasing framing time of the LED is shown in Figure 5.8.

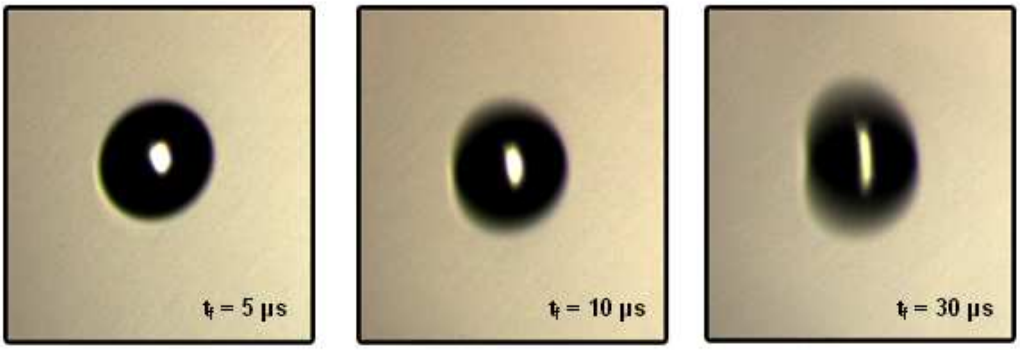

Figure 5.8 Pictures of microdrops captured with stroboscopic illumination. A framing time of t_f=5 µsec shows practically no distortion whilst a framing time of t_f=30 µsec results in the appearance of an elongated microdrop.(Graceffa, Burghammer et al. 2008)

A change in delay between the microdrop ejection and the LED activation (Figure 5.4) will change the position of the microdrops along their trajectory as shown in Figure 5.9.

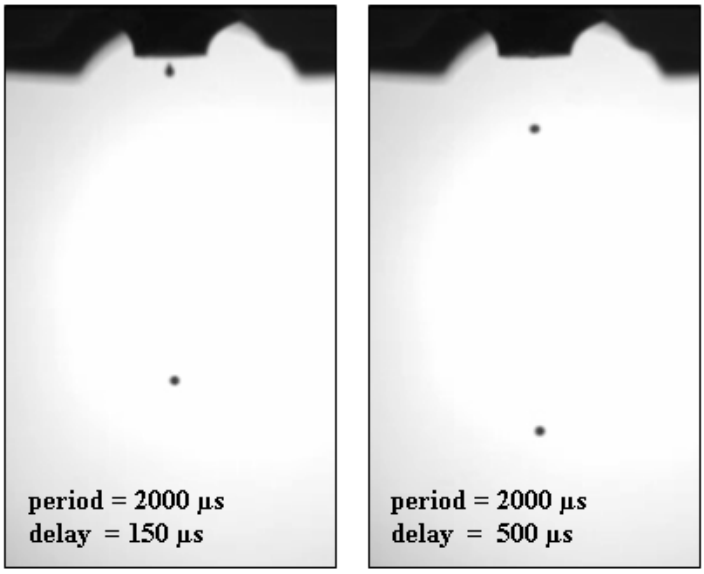

Figure 5.9 Influence of microdrop parameters on microdrop positions along trajectory

5.3.6 Pressure control

The pressure in the inkjet head is an important parameter for an inkjet DOD system. In order to keep the trajectory of the microdrops constant one has to maintain the pressure in the inkjet head constant via a constant liquid level in the storage container. A change in pressure modifies also the position of a microdrop observed under stroboscopic conditions. (see section 6.2.4) The reservoir is constantly refilled by a *Harvard Pico Plus* syringe pump system.[e] The speed of the liquid flow is controlled via a program, developed by Richard Davies, running on PC. (see ANNEX C)

[e] www.harvardapparatus.com/webapp/wcs/stores/servlet/haicat1_10001_11051_37295_-1_HAI_Categories_N

ID13 beamline set-up

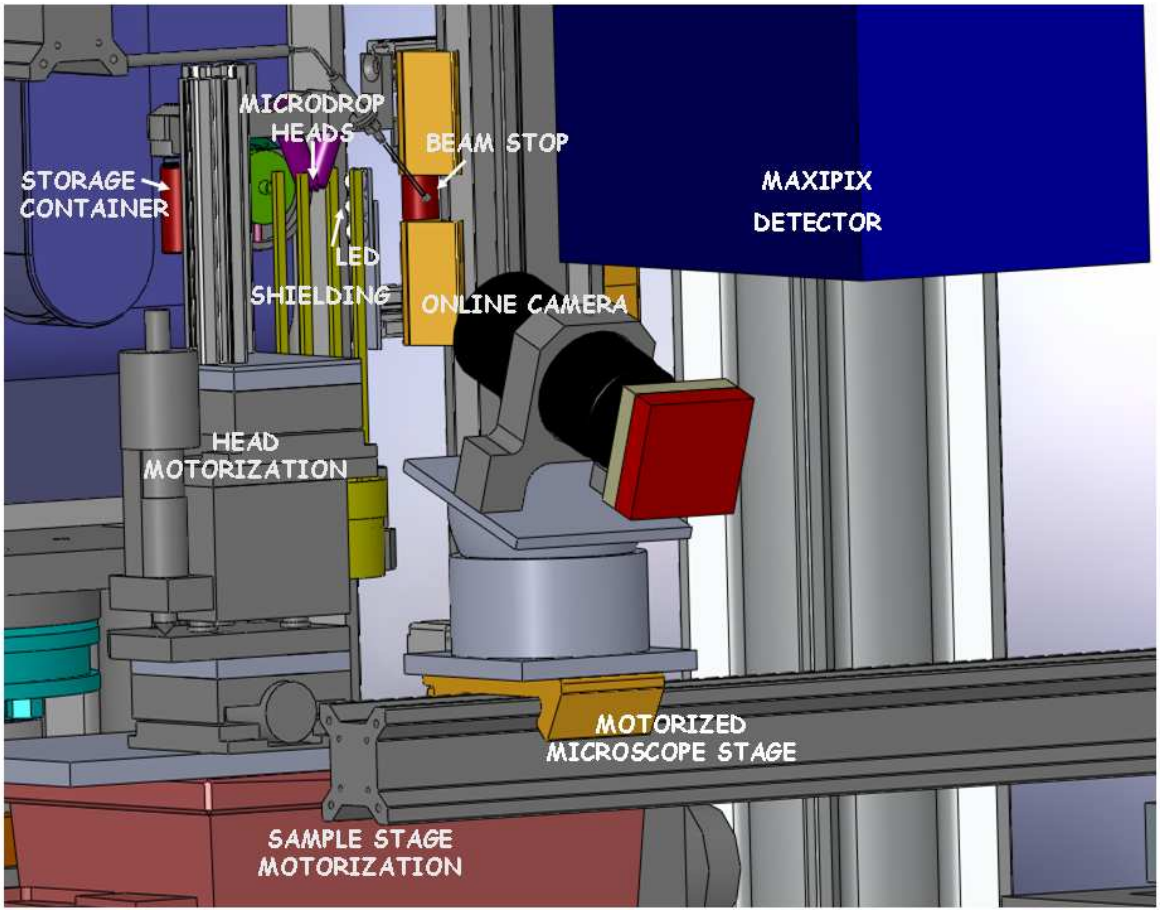

Figure 5.10 Schematic picture of DOD inkjet setup installed at the ID13 beamline. A Maxipix pixel detector is used for data collection. (see below)

The set-up of the DOD inkjet system for microdrop mixing experiments at the ID13 beamline includes:

- two dispenser heads with storage containers
- motorization of one head and its storage container to match the trajectories of the two drops
- two syringe pumps to refill the storage containers
- the shielding of the microdrop tracks against air perturbations and its motorization
- the LED
- sample stage motorization
- online CCD camera and its motorization

A schematic picture of the beamline setup (Solid Works) is shown in Figure 5.10. Figure 5.11 shows a picture of the set-up installed at ID13 beamline.

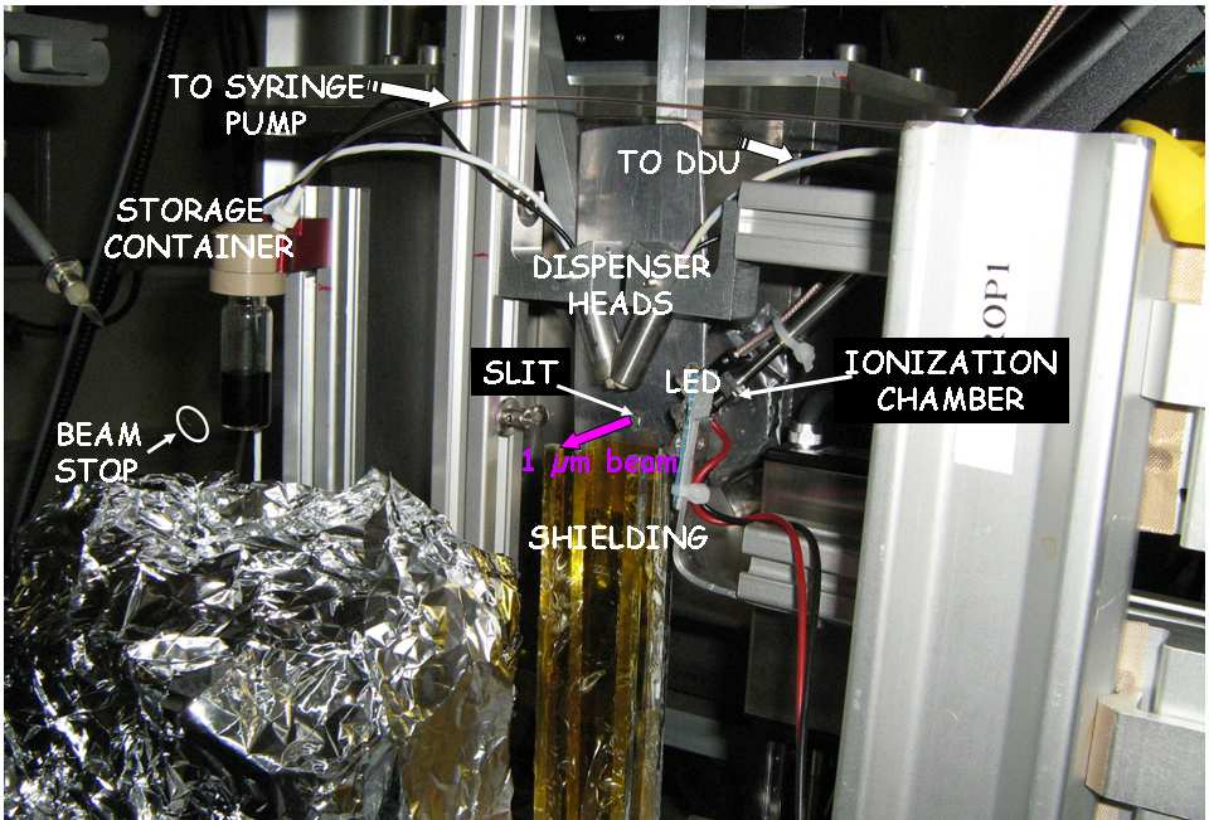

Figure 5.11 Picture of the set-up installed at ID13 beamline. The detector, the camera, the beamstop and the shielding are moved out of the sample area to access the inkjet heads.

5.4 Detectors

5.4.1 Introduction

The main requirements for the detector used in the present work are:

- *high sensitivity in view of weak signals:* this is due to the small sample volumes of microdrops with sub-nl volumes which imply weak scattering signals. For SAXS data collection a sufficient dynamic range (14 bits or more) is required.
- *stroboscopic data collection mode:* in order to minimize the air background, it is necessary to collect data in stroboscopic mode. (see above) Assuming a flight time of ν=2m/s, the flight time of a 100 µm microdrop through a 1 µm X-ray beam will be 50 µs. The stroboscopic time resolution of the detector should be at least 1/10, i.e. 5 µs of the 50 µs transit time of the microdrop through the 1 µm beam (see above) in order to resolve local features in the microdrop. An example for this will be shown in the experimental part. If one wants only to obtain as much as possible scattering signal with a reduced local resolution, the framing time can be increased to several 10^{th} of μs. The schematic triggering sequence is shown in Figure 5.4.

For stroboscopic data collection I used initially a FReLoN CCD camera with a triggered image intensifier and subsequently a Medipix pixel detector with a triggered detector frontend. In the following the basic features of both detection systems are described.

5.4.2 The FReLoN CCD camera[f]

A schematic picture of the FReloN CCD camera(Labiche, Mathon et al. 2007), integrated in the microdrop control system, is shown in Figure 5.12 The camera was custom build by the ESRF detectors group for the ID13 beamline.(Graceffa, Burghammer et al. 2008)

Detector parameters: The detector is based on an integrating charge coupled device (CCD) with 2048x2048 pixels of 51.05x51.05 μm^2 size with 14 bit readout data. The CCD was binned to 512x512 pixels so that the binned pixel size matches the point spread function of about 200 μm full with at half maximum of the entrance converter screen. The gain of the detector at 13 keV is about 61 ADU/X-ray photon (analog-to-digital units) while the readout noise is 1.9 ADU/pixel. The detector has a 110 mm entrance window with an Itech P43 X-ray converter, which is coupled by a fiber optics reducer to a 40 mm diameter Proxitronic microchannel plate (MCP) amplifier.

Stroboscopic operation: The MCP-PROXIFIER has 100 ns gateability with a maximum triggering frequency of 14 kHz (company specs). The image from the MCP P43 output phosphor is transferred to the CCD by a lens coupler with demagnification 1.33:1. During stroboscopic operation, the CCD is continuously operated and the MCP intensifier is typically activated with a frequency of 1 KHz during 2 μs. This is in the range of the required time resolution of 5 μs. (see above). In practice it was not possible to trigger the MCP efficiently as the recorded signal on the detector was very weak.

[f] www.esrf.fr/UsersAndScience/Experiments/TBS/ISG/opiom

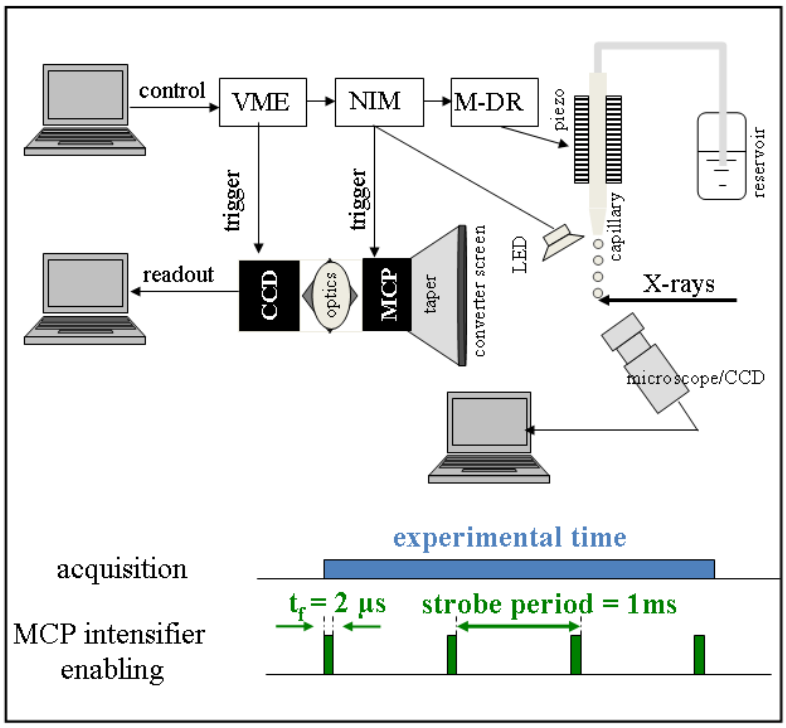

Figure 5.12 Schematic design of microdrop control system with integrated LED and Frelon camera. (MCP: Micro-Channel-Plate)

5.4.3 The Medipix2 pixel detector(Ponchut, Visschers et al. 2002; Ponchut, Zontone et al. 2005; Ponchut, Clément et al. 2007)

A schematic picture of the Medipix2 detector, integrated in the microdrop control system, is shown in Figure 5.13.

Detector parameters: the Medipix2 chip is a pixel-detector readout chip consisting of 256 × 256 identical elements, each working in single photon counting mode for positive or negative input charge signals. The basic principle is the single photon detection with direct X-ray to charge conversion in a semiconductor. Each pixel cell occupies a total surface area of 55 µm × 55 µm. It acts as an independent X-ray photon counter including a charge preamplifier, a shaper, a discriminator and an event counter. The image produced during an exposure is the map of the number the events above the threshold in each pixel. The readout system architecture consists essentially of a custom readout board named PRIAM (Parallel Readout Image Acquisition for Medipix), a fast serial PCI board with fiberoptic input/output ports. It allows external trigger modes with µs resolution.

Stroboscopic operation: By operating the system in a stroboscopic acquisition mode, counts are only accumulated on the readout electronics during a defined exposure window (t_f). At the end of the stroboscopic sequence, the counts are readout to a custom readout board and

transferred to a PC. The overall counting time t_o is user defined. The minimum exposure time used in the present work was t_f=5 μsec, which is compatible with the 1 μs maximum dead time of the Medipix pixels.

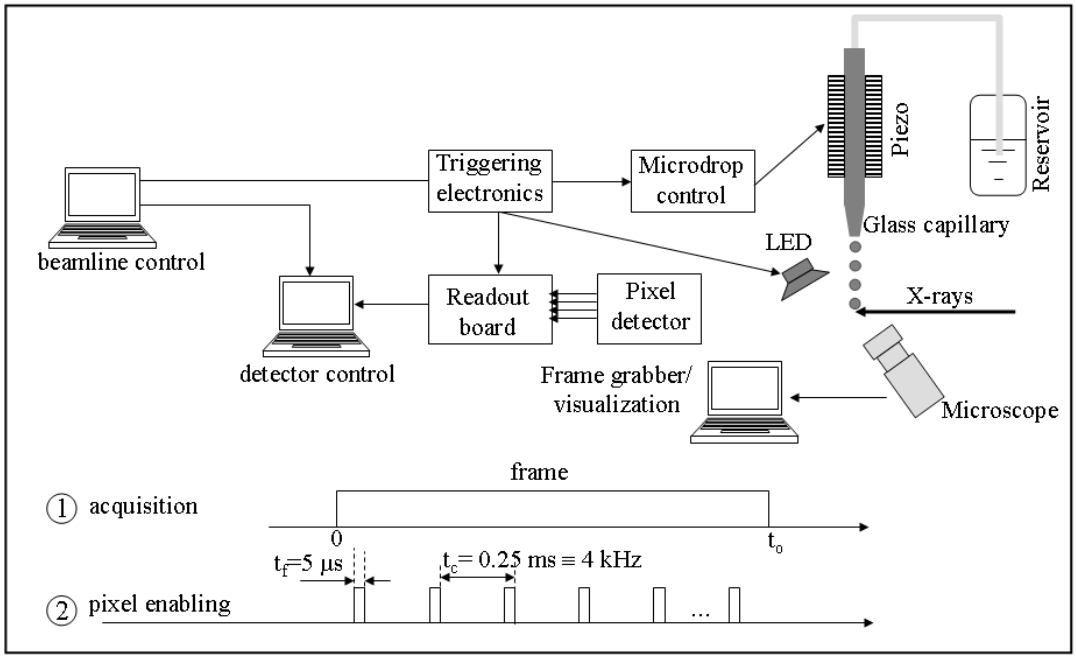

Figure 5.13 Schematic design of microdrop control system with integrated LED and pixel detector.(Graceffa, Burghammer et al. 2009)

5.5 SAXS data corrections (Lindner 2002; Narayan 2008)

In order to compare scattering data from different experiments (I_s) it is necessary to normalize them to the scattering cross section of the sample for volume unit (I_N):

$$I_N = \frac{I_s}{I_i \ \varepsilon \ T \ \Delta\Omega \ l} \qquad (1)$$

with I_i incident intensity, ε detector efficiency, T sample transmission, ΔΩ solid angle subtended to the detector element, l thickness of the sample (see section 2.1). The normalization of the scattered intensity towards the solid angle subtended by the pixel elements requires the knowledge of the distance sample-detector (L). Silver behenate was used as calibrant. It shows diffraction peaks at $Q = 2\pi n / 5.837\ nm^{-1}$, where n is the diffraction order. From a pattern of silver behenate collected at the same distance of the sample it is possible to determinate the distance sample-detector. After masking the unusable pixels, the azimuthal averaging of the normalized 2-D patterns as function of the distance from the transmitted beam, gives $I(Q)$.

For the Maxipix detector dark current subtraction and corrections for the spatial distortion of the detector are not required. A ionization chamber was used as monitor counter of the incoming beam intensity. The following corrections were applied to the stroboscopic data acquired at the ID13 BL:

1. **Acquisition time normalization**: The data are acquired in a stroboscopic way. Given the experimental time, the detector is acquiring only for a few μs for each period according to the scheme in figure 5.14. The exposure time of the sample is:

$$exposure\ time = \frac{experimental\ time * framing\ time}{strobe\ period} \qquad (2)$$

The data are divided by the exposure time.

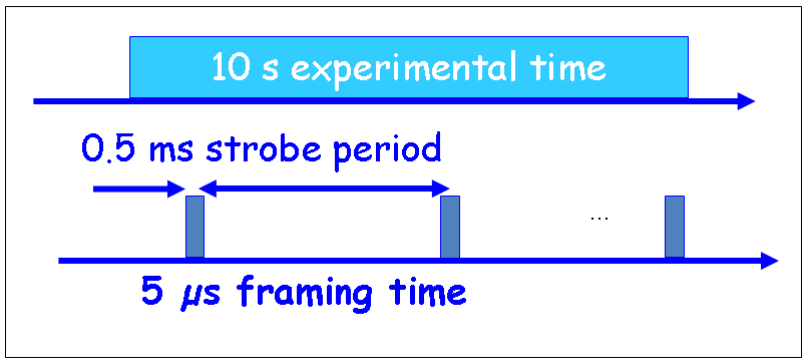

Figure 5.14 Stroboscopic acquisition scheme

2. **Incoming intensity normalization**: Incoming X-ray intensity values were divided by the experimental time, since the ionization chamber acquires not in a stroboscopic mode. Dark current values of the ionization chamber (recorded without X-ray beam) were subtracted from the total incoming beam intensity. *The scattering intensity values are divided for the corresponding corrected incoming intensity values.*

3. **Sample thickness normalization**: By mapping the drop through the beam it is possible to obtain the shape of the drop and, therefore, the position of the incoming beam respect the drop, and the length of the path of the beam inside the drop. *The scattering intensity is divided by this value, to normalize for the thickness of the samples.*

4**. Transmission correction**: An experimental correction for the sample transmission was not performed. However, an estimate of the transmission variation has been done according to the following calculation. For mixed microdrops of 100 μm diameter with solutions of 2mM or 5 mM cytochrome C in HCl and 85 mM $NaCH_3CO_2$ (NaAc) the transmission can be derived from:

$$T_{sol} = T_{H_20} * T_{HCl} * T_{NaAc} * T_{cytochrome}$$

The transmission values of the components have been calculated with a program from the Berkeley lab web site: http://henke.lbl.gov/optical_ constants/filter2.html, for X-ray energy of 12.5 keV, at which the experiment was performed.

T_{sol} = 0.97457*0.99995*0.99959*0.99941= 0.973547

The picture 5.15 shows the transmission due to the cytochrome C, as function of its concentration which is about 1%.

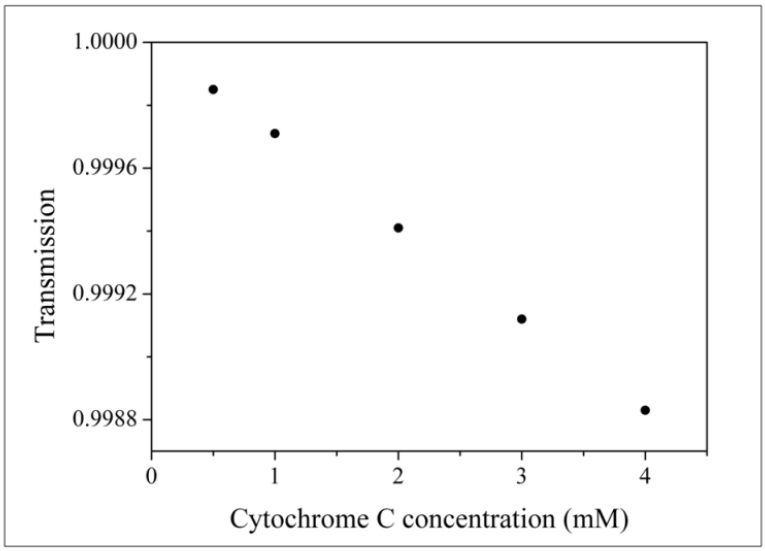

Figure 5.15 Cytochrome C transmission as function of its concentration at 12.5 keV. (LBL-website software)

6 Résultats et Discussion

Dans ce chapitre, j'exposerai les résultats expérimentaux obtenus. Pour tester la faisabilité d'expériences stroboscopiques avec les microgouttes, nous avons utilisé paraffine, matérielle avec un fort pouvoir de diffusion. La paraffine fondue, maintenue à une température de T=360±2K, a été émise sous forme de microgouttes de diamètre de 80 μm. Les gouttes ont été explorées avec un faisceau de rayons X de 3 μm jusque à une distance maximale de 7 mm da lu point de formation.

Donnée de micro diffraction de rayons X stroboscopique a étant recueilli, en montrant la faisabilité de la technique. Il a été possible de tirer la température de la paraffine dans les microgouttes par calibration avec des expériences statiques de diffraction; cette température est près de la température de fusion. Les pics caractéristiques l'état cristallin ne sont pas relevés. La température du processus de solidification a été vérifiée aussi auprès des mesures de calorimétrie différentielle à balayage.

Microgouttes de paraffine liquide a été déposé sur substrats de verre ou de cuivre, à distances différentes de leur point de formation. Les chaînes d'alcanes montrent une orientation préférentielle voisins à l'appui; telle orientation augmente dans le cas dans lequel le substrat utilisé est le cuivre. Gouttes déposées sur cuivre aux hauteurs différentes montrent une augmente orientation à l'augmenter de la distance du capillaire.

Expériences de diffusion centrale sur microgouttes de solutions de cytochrome C, qui a un faible pouvoir de diffusion, ont été donc effectuées. Pour vérifier la bonté des données recueillies et obtenir valeurs de rayon de giration de la protéine en solution diluée, simulations théoriques avec le programme CRYSOL et expériences statiques de diffusion centrale ont été exécutées sur BL ID02. Le processus de repliement du cytochrome C a été recherché, par mélange d'une microgoutte de solution de cytochrome C dénaturé avec une goutte de tampon qui rétablit l'état natif. Le mélange a été opéré en vol.

6. Results and Discussion

6.1 Paraffin wax microdrops(Graceffa, Burghammer et al. 2008)

6.1.1 Introduction

In order to develop stroboscopic data collection techniques I studied first liquid paraffin wax (see section 5.1) which shows a strong WAXS pattern in the solid state.(Chevallier, Petitjean et al. 1999; Briard, Bouroukba et al. 2006) Paraffin wax microdrops are used by graphics industry for producing high quality impressions by DOD inkjet technology.(Korol and Greb 2000; Gans, Duineveld et al. 2004) The phase diagram and the crystalline phases of paraffin wax have been studied in great detail.(Ungar 1983; Ungar and Masic 1985; Chevallier, Petitjean et al. 1999; Briard, Bouroukba et al. 2006) In order to calibrate the temperature of the paraffin wax microdrops from the WAXS-patterns collected under stroboscopic conditions, I also performed static WAXS experiments on paraffin wax. The crystallographic phase transitions observed in the static experiments were checked by complementary DSC experiments.

6.1.2 DSC experiments

Methods: I used a SETARAM DSC 131 instrument at the ILL chemical laboratory. The sample weight was 10 mg. Experiments were performed with continuous cooling rates of 0.5 K/min and 2 K/min. The difference in the amount of heat required increasing the temperature of the paraffin wax and a reference sample was measured as a function of temperature.

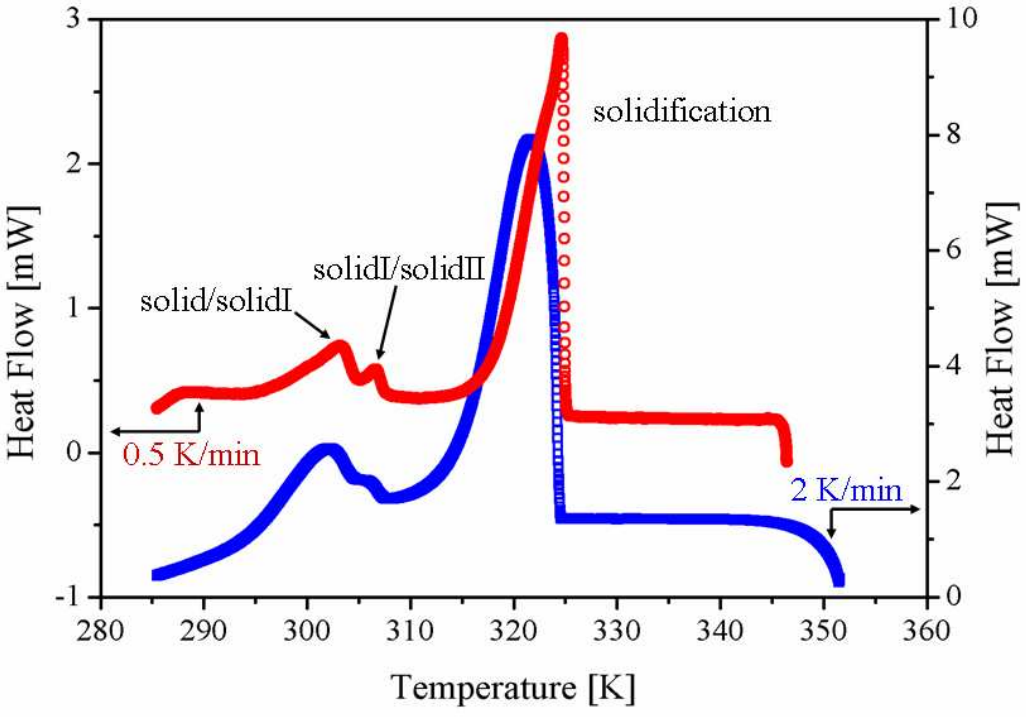

Figure 6.1 DSC cooling curve of paraffin wax during ramping with 0.5 and 2 K/min

Results: Figure 6.1 shows a graph of the heat flow versus the temperature for the two cooling conditions. The peaks correspond to the heat production associated to the phase changes of the paraffin wax sample. The DSC curve was analyzed as described elsewhere.(Chevallier, Petitjean et al. 1999; Briard, Bouroukba et al. 2006) From the 0.5 K/min DSC curve, the crystallization point is derived at T_{cryst}=324.6 K, the maximum of the 1st solid/solid transition at 302.2 K and that of the 2nd solid/solid transition at 306.2 K. The shift of the liquid/solid transition DSC peak for the larger cooling rate is due to a thermal lag.(Wunderlich 1990)

6.1.3 Static WAXS experiments

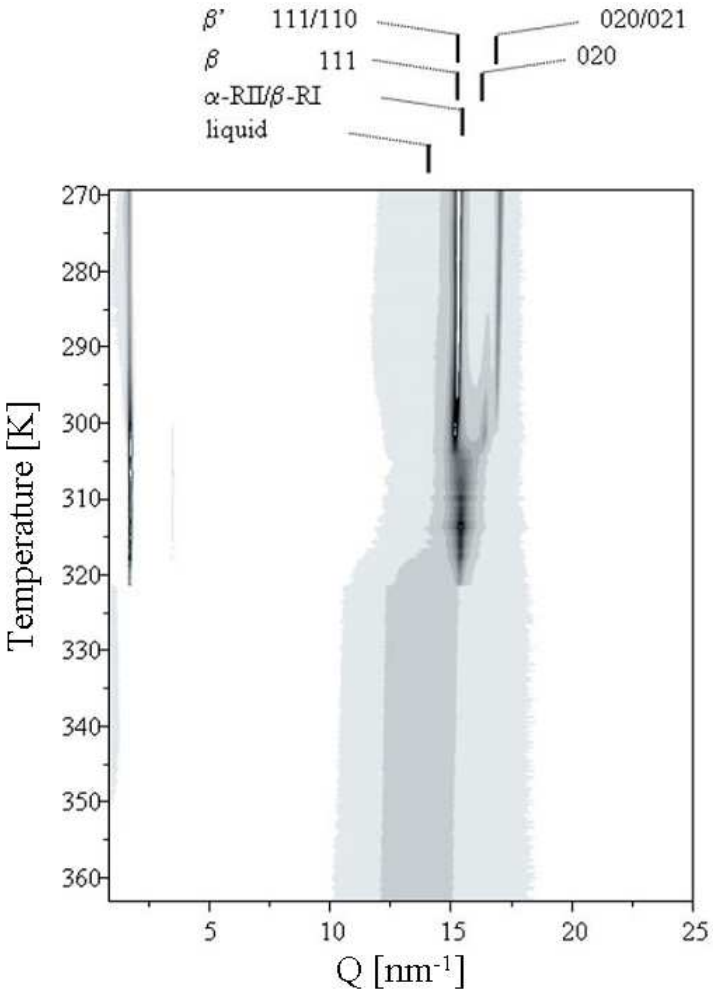

Figure 6.2 Sequence of azimuthally integrated 2D WAXS-patterns recorded during ramp-cooling of a paraffin wax sample with 3 K/min.(Graceffa, Burghammer et al. 2008) The pattern sequence has been converted into a temperature scale provided by the cryoflow system thermocouple. The positions of selected reflections for selected phases are indicated: β': orthorhombic; β: cubic; β-RI: cubic, α-RII: hexagonal.

Methods: WAXS-patterns were collected at the ID13 BL from an 80 μm diameter borosilicate glass capillary filled with paraffin wax during ramp-cooling at 3 K/min. The capillary temperature was controlled by an *Oxford Cryosystems* Cryostream 700 system with 5 liters/min nitrogen flow. The nitrogen gas temperature at the sample position is within 1 K of

the cryoflow set-temperature for a range of 10±5 mm according to company specs.[g] Several patterns were also measured at selected constant temperatures defined by the cryoflow system.

Results: A sequence of azimuthally integrated 2D WAXS-patterns obtained during cooling from the melt into the solid with 3 K/min is shown in Figure 6.2. The temperature scale is provided by the thermocouple output from the cryoflow system. These WAXS-experiments allow the observed DSC peaks to be associated with the transition of the liquid phase into the α-RII/β-RI rotator states(Ungar 1983; Ungar and Masic 1985) and the α-RII/β-RI and β/β' solid-solid transitions.(Chevallier, Petitjean et al. 1999; Briard, Bouroukba et al. 2006) The dynamic structural and thermal data recorded by me for similar cooling speeds show a good correspondence.

6.1.4 Stroboscopic WAXS experiments

Methods: A high temperature DOD system from *Microdrop Technologies GmbH* was used. (see section 5.3.3) Experiments were performed with 70 μm diameter paraffin wax microdrops. WAXS-patterns were recorded by a 14-bit readout FReLoN CCD detector.(Labiche, Mathon et al. 2007) (see above) The LED and MCP intensifier were activated with a frequency of 1000 Hz during 2 μs. (see section 5.3) The CCD was typically operated for up to 30 s prior to readout, which corresponds to a total signal accumulation time of up to 60 ms in a triggering sequence. Further experimental parameters are provided in Ref. (Graceffa, Burghammer et al. 2008)

The relative position of the ejected microdrops from the glass capillary exit was determined by the ID13 on-axis microscope. The error in position measurement is estimated as ≤ 0.01 mm. The microdrops visualised under the same stroboscopic conditions are ejected at different periods, i.e. separated by 1 ms. The microdrop speed is derived from the distance between consecutive microdrop pairs detected with the same strobe conditions. (Figure 6.3) The reduction in speed with distance is due to the viscous resistance of air.(Lee 2003)

[g] www.oxfordcryosystems.co.uk/cryostream/plusdownloads.htm

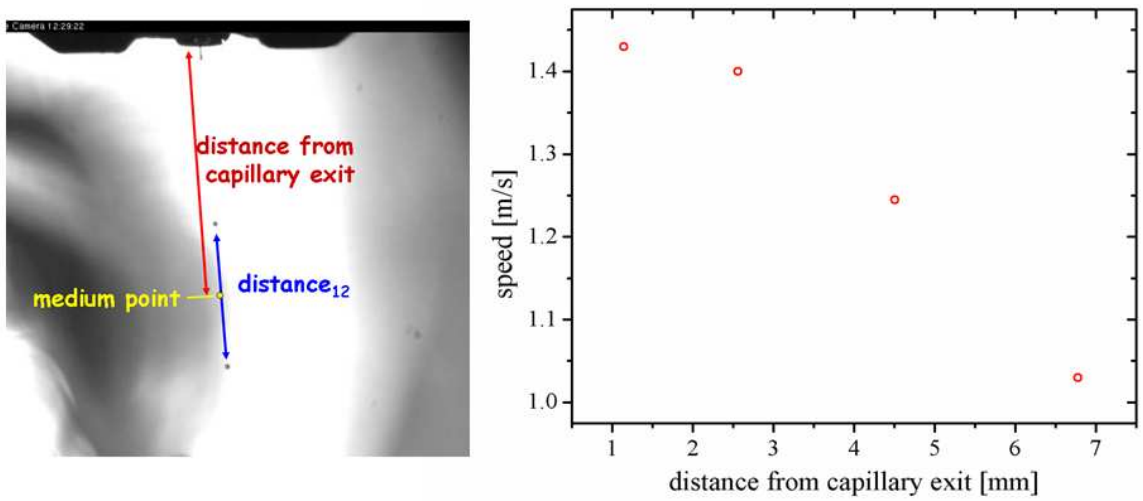

Figure 6.3 Distance of consecutive microdrop pairs from the capillary exit and separation of consecutive pairs. The microdrop speed is calculated for a 1000 Hz strobe frequency. The error in position measurement is ≤ 0.01 mm.

WAXS-patterns of stroboscopically frozen microdrops were obtained at five distances from about 0.5 to 8 mm from the capillary exit. The microdrop was also scanned horizontally across the microbeam at several distances from the capillary exit with a step resolution of 25 μm.

Results: A typical WAXS-pattern of a microdrop close to the nozzle is shown in Figure 6.4 A. (60 ms total signal accumulation time)

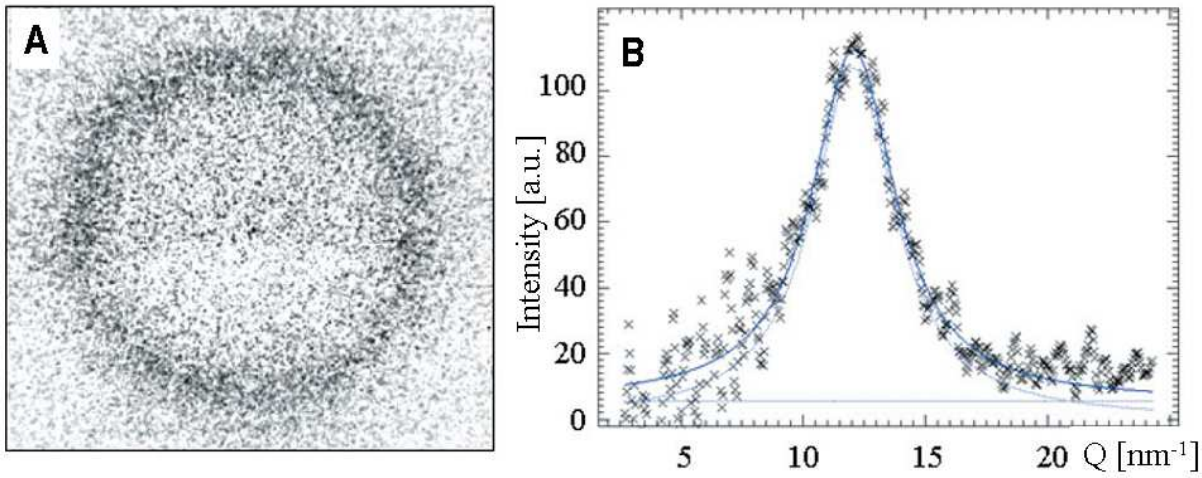

Figure 6.4 A WAXS pattern of a liquid paraffin wax microdrop obtained under stroboscopic conditions; B Azimuthally integrated pattern with fitted Lorentzian profile and zero-order polynomial (blue curves). The thicker fitted curve corresponds to the sum of Lorentzian and polynomial profiles.

The scattering from air collected for an equivalent period just outside the microdrop is subtracted. The beamstop is not well visible due to the small size of the beamstop, the short integration time and the background subtraction. The peak profile of the azimuthally

integrated microdrop pattern obtained during stroboscopic data collection can be fitted by a single Lorentzian function, which is expected for liquid scattering. The Lorentzian peak profile (Figure 6.4B) was observed for all distances of the microdrops from the capillary exit. No evidence for a peak due to a solid phase (Figure 6.2) was observed. Figure 6.5A shows the liquid peak position as a function of the microdrop distance to the capillary exit for all microdrops studied.

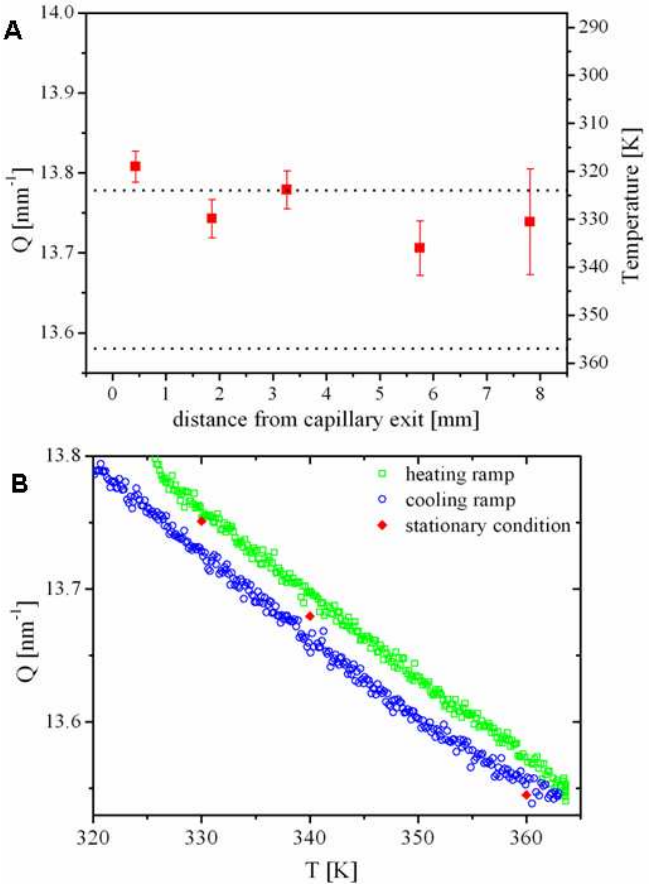

Figure 6.5 A : Microdrop peak positions (Lorentzian function) with σ-value error bars as a function of distance from the capillary exit. The temperature of the glass capillary heating element and the wax paraffin crystallization temperature (T_{cryst}) are indicated. B: Variation of Q value of paraffin wax peak in the liquid phase range during heating and cooling ramps. The red points represent data recorded under stationary conditions.

The temperature scale in Figure 6.5A is obtained from the liquid paraffin wax calibration curve by linear interpolation between the heating and cooling curves to compensate for the thermal lag (Figure 6.5B). The Q-values of the peaks suggest that the temperature of the microdrops corresponds to within 2σ to the paraffin wax crystallization temperature of 324.6 K, which is about 32 ±2K below the temperature of the heating element. The rather constant temperature of the microdrops (up to about 8 mm distance from the capillary nozzle exit) agrees experimentally with modelling (Gao and Sonin 1994) which supports the suggestion that the thermal diffusion timescales inside the microdrop are much larger than the microdrop

cooling timescales.(Gao and Sonin 1994) The thermal homogeneity of the microdrop is also supported by the structural homogeneity upon lateral scanning.(Graceffa, Burghammer et al. 2008) The observation that the temperature of the ballistic microdrops is at the crystallization temperature is assumed to be due to a strong temperature gradient between the paraffin wax temperature at the heating element and the exit of the glass capillary which is thermally not shielded. This is corroborated by the occasional observation of small pieces of solid paraffin wax at the capillary exit surface.

Conclusions: The paraffin wax experiments demonstrate the technical feasibility of stroboscopic WAXS-experiments at the ID13 BL. The intensity of the stroboscopic WAXS patterns appear, however, to be too weak (Figure 6.4A) as compared to equivalent time static WAXS-experiments on paraffin wax. An inefficient triggering of the FReLoN detector image intensifier is the most probable cause for this. For the subsequent stroboscopic SAXS experiments I used therefore a Medipix pixel detector with direct on-chip pattern integration.

6.1.5 Paraffin wax microdrop deposition

Introduction: The control of the deposition process is of particular importance for technological applications such as high definition printing in graphics industry.(Korol and Greb 2000; Gans, Duineveld et al. 2004) Microstructural information on the deposited microdrops is, however, lacking although simulations of the deposition process have been performed.(Gao and Sonin 1994) I have performed preliminary WAXS-experiments for ballistic paraffin wax microdrops deposited on solid surfaces in order to explore the homogeneity of the deposited microdrops.

Liquid drop impact on solid surfaces is known to be associated with oscillatory behavior of the drop shape.(Rein 1993; Kim, Park et al. 2003) During the initial stage of impact the drop is deformed and compressed at its base.(Rein 1993) An interesting question was whether this deformation would result in a texture development of the solidified microdrop.

Methods: The microdrops were deposited on a copper wire and on a glass capillary at different distances from the capillary exit. These two substrates were chosen according to their large differences in thermal conductivities (k) which might influence the cooling rate of microdrop solidification. (Glass: k=1.1 W/m-K for glass; Copper: k=401 W/m-K)

Results: Figure 6.6 shows A: microdrops on a glass capillary at 15 mm from the microdrop capillary exit; B: on a copper wire 10 mm far from capillary exit and (C): on glass at 10 mm from the capillary exit.

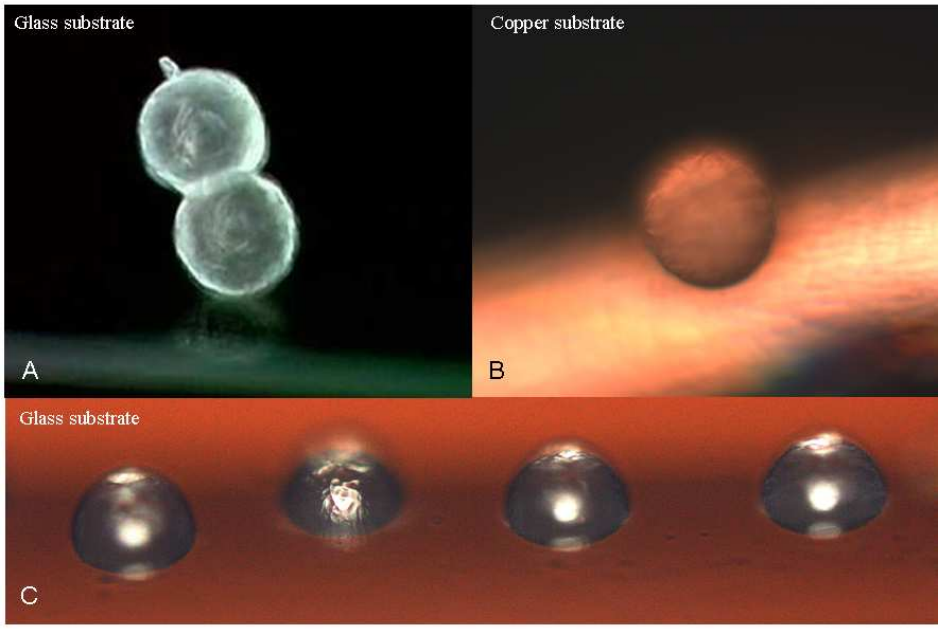

Figure 6.6 Microdrops deposited on glass capillary and copper wire substrates A: substrate 15 mm away from the microdrop generator capillary exit; B: substrate 10 mm far from capillary exit; C: substrate at 10 mm far from capillary exit. The drop diameter is about 70 μm.

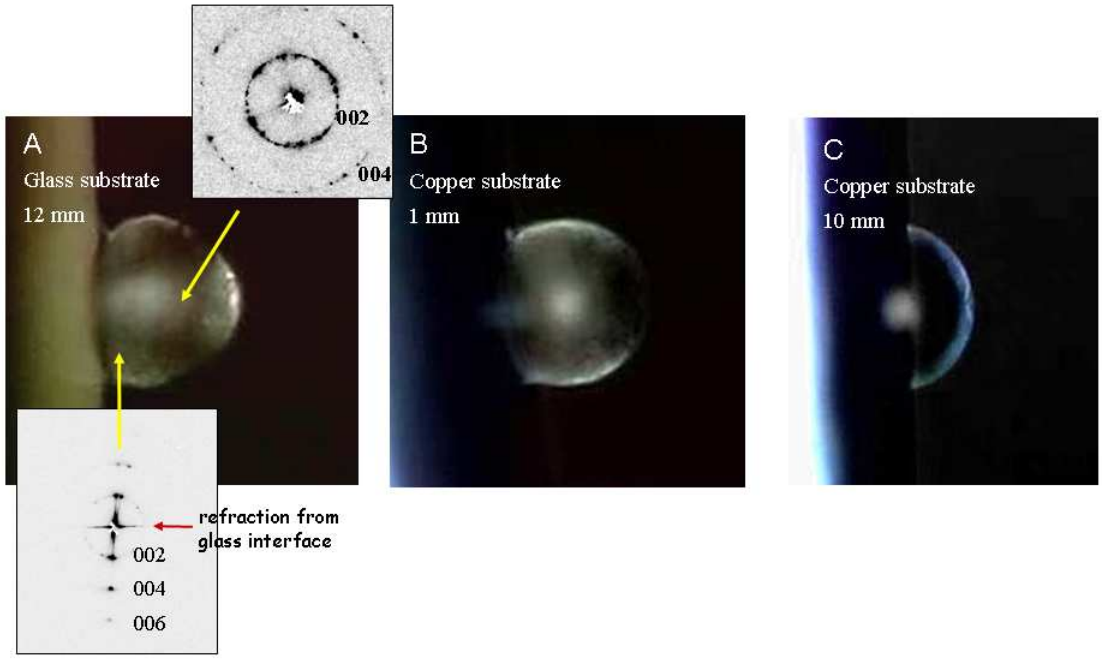

Figure 6.7 A: paraffin wax microdrop at 12 mm from the capillary exit with WAXS patterns from several locations across the microdrop. Background due to copper interface scattering has been subtracted (see text). The 00l peaks shows a preferential orientation close to the glass capillary. The horizontal streak is due to refraction from the glass interface. The scale of the microdrop is indicated in Figure 6.9B; B: paraffin wax microdrop solidified on copper substrate at 1 mm from the capillary exit; C: paraffin wax microdrop deposited on copper at 10 mm from the capillary exit. The sharp cutoff of the microdrop edge is due to partial obstruction by the copper substrate.

A strong deformation is only observed at the glass interface at 10 mm distance from the capillary. Microdrops solidified on a glass capillary at 12 mm far from the capillary exit of the microdrop generator and on a copper wire at 1 mm and 10 mm from the capillary exit are

shown in Figure 6.8A/C. Selected WAXS-patterns from different locations on the microdrop are shown for the glass substrate. We note the particularly strong 00l reflections which are due to the lamellar packing of the paraffin molecules and thus the alignment of the crystalline domains. The glass and copper interfaces can be located from strong refraction streaks as shown in the WAXS-pattern in Figure 6.7A

The microdrops were mapped through the beam using a 2*2 μm raster. A composite picture for WAX-patterns collected from a paraffin wax microdrop on a copper wire (at 10 mm from capillary nozzle) is shown in Figure 6.8. The strong diffuse scattering at the copper interface is overlapping the paraffin wax scattering. The same is observed for the glass interface. In order to enhance the paraffin wax scattering a background subtraction was necessary.

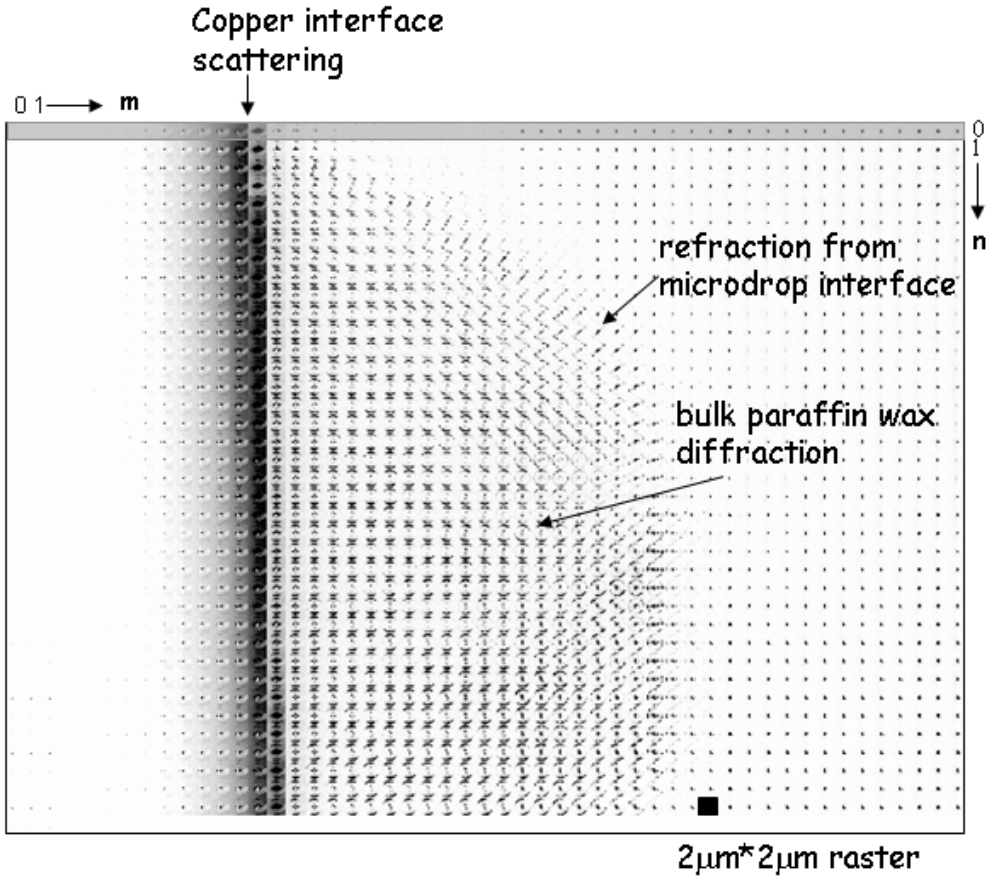

Figure 6.8 Composite image of paraffin wax drop at 10 mm from capillary nozzle on copper wire. m,n define an 2D array of WAXS-patterns (see text).

One can define the composite image in Figure 6.8 as an array of WAXS-patterns $P_{m,n}$ (n=0→50; m=0 →36). The background subtraction was performed as $\Delta_{m,n}=P_{mn}-P_{0,n}$ with $\Delta_{m,n}$ corresponding to the difference WAXS-pattern. This implies that the first row WAXS-

patterns were subtracted in columnar way from all the other WAXS-patterns. The WAXS-patterns shown in Figure 6.7A have been corrected in this way.

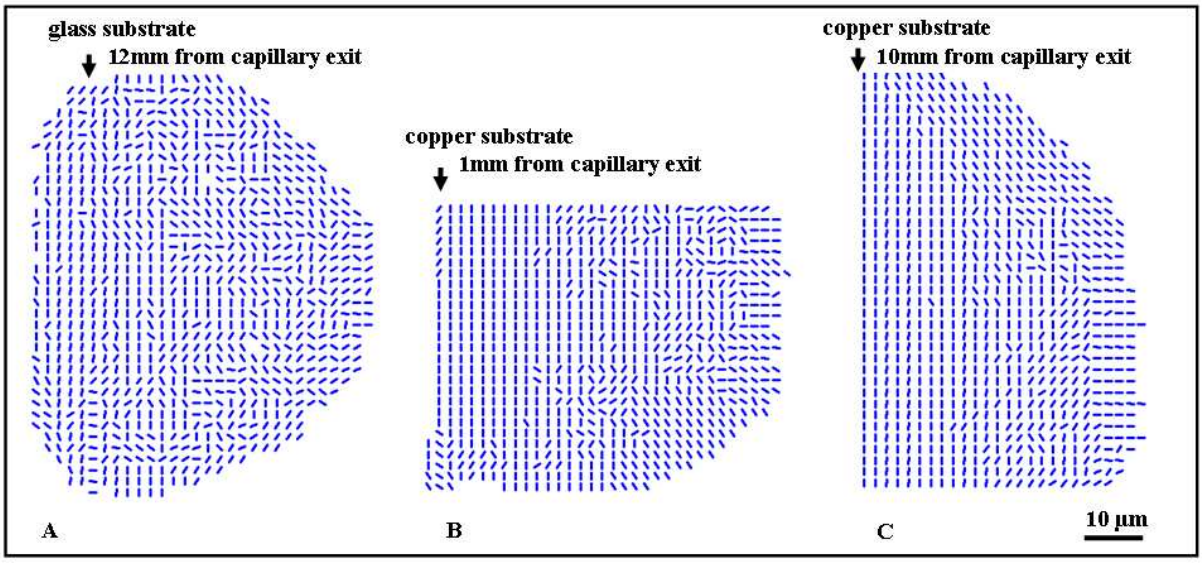

*Figure 6.9 Paraffin wax microdrop mapped with 2µm*2µm mesh for A: glass 12mm away from capillary exit (see Fig.6.7A), B and C copper substrates. The position of the interface is indicated by an arrow. The lines indicate the local c-axis orientation inside the microdrop for glass (see Fig.6.7) and copper substrates. Note the strong orientation close to the substrate interface. For the copper substrate an extended domain with homogeneous c-axis texture is observed.*

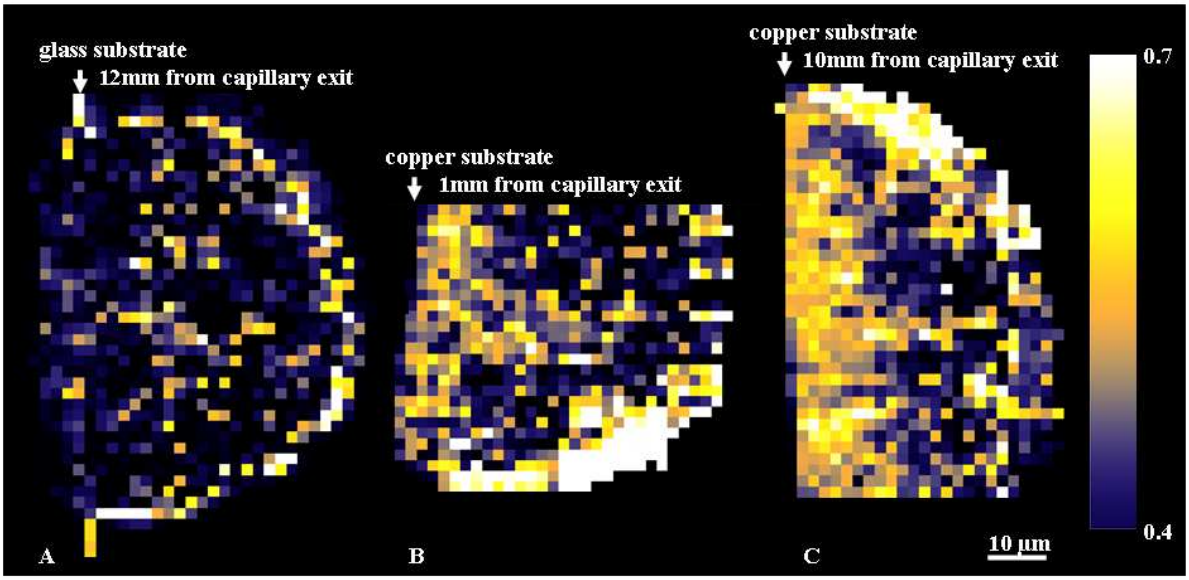

Figure 6.10 Map of preferred orientation parameter α of the paraffin wax chains (see text). A: Microdrop deposited on glass (see Fig.6.7A) 12 mm away from the capillary exit; B: copper substrates 1 mm away from capillary exit; C: copper substrate 10 mm away from capillary exit. The sharp cutoff in (C) is due to a partial obstruction of the deposited microdrop by the Copper wire (Figure 6.7C)

In order to quantify the orientational order of paraffin chains at the glass and copper interfaces, the azimuthal range of the 002 reflection was divided in twelve regions of 30 degrees each and the intensity was integrated in every region. The values of the opposite angular regions (180^0 distant) were summed up to provide an integrated intensity. The angle

of maximum integration value was chosen as orientation of the c-axis vector. Figure 6.9 shows map of the c-axis vector orientation for the microdrops shown in Figure 6.7. The ratio $\alpha=I_{max}/I_{tot}$ between the maximum integration value (I_{max}) and the total intensity (I_{tot}), shown in the figure 6.10, is correlated with the texture of the paraffin wax chains. Random orientation of chains implies that $I_{max}=(I_{tot})/6=0.167$ while ideal texture implies that $I_{max}=I_{tot}$ and a value of $\alpha=1$. An overall α-scale is incorporated in Figure 6.10. Discrete α-values in Figure 6.10 were obtained via software.

Figures 6.9 and 6.10 show a sharp cutoff at the copper substrate interface while paraffin wax scattering is observed within the glass capillary for the glass substrate interface. This can be explained by the higher absorption coefficient of copper as compared to glass.(Vaughan 1986) The X-ray beam will be practically absorbed by the copper wire while the glass capillary still shows a finite X-ray transmission. The observation of paraffin wax scattering from within the glass capillary confinement (Figure 6.10A) suggests also that the paraffin wax drop interface is not aligned parallel to the glass surface. This can also be seen in the optical image in Figure 6.7A. The sharp cutoff of the paraffin wax drop at the copper interface (Figure 6.10B/C) suggests a similar misalignment.

For the microdrop on the glass substrate the α-value is on the average 0.3 by sampling over a number of pixels in Figure 6.10A. A large domain of parallel chain-axis orientation extending into the bulk of the microdrop is, however, observed in the case of copper substrates (Figure 6.9B/C), especially for the microdrop deposited at 10 mm (Figure 6.9C). The α-value at the copper interface is on average about 0.5 for both distances (Figure 6.10 B/C). This value extends to a larger volume fraction in the case of the drop at 10 mm from the capillary exit (Figure 6.10C).

Conclusions: The distribution of α-values shows a weak preferred orientation of paraffin wax at the glass interface but a strong preferred orientation at the copper interface. The preferential alignment of the c-axis parallel to the substrate interface implies that the paraffin wax chains are parallel to the substrate interface. An increase of the distance of the copper interface to the capillary exit increases also the volume fraction of preferred orientation in the microdrop. The origin of these differences could be related to the cooling rate and, therefore, to the solidification rate of the microdrop on substrate. The process is faster on the copper substrate due to the higher thermal conductivity. This results apparently in a freezing-in of the aligned chains in an extended domain. The lower thermal conductivity of the glass substrate delays the freezing-in of the bulk chains. It is reasonable to assume that an increased travelling

distance up to impact of a microdrop in air at 22^0C will result in higher heat dispersion. It is also interesting to note that the microdrop at 15 mm from the capillary exit retains a spherical shape on the glass substrate. (Figure 6.6A) It is therefore suggested that this reflects an already crystallized microdrop (only a rigid outer shell is required) impinging on the substrate. This assumption is supported by the observation that the temperature of the ballistic microdrop is already close to the crystallization temperature up to 8 mm from the capillary exit.(Graceffa, Burghammer et al. 2008) The structural data of the microdrops deposited at 10 mm from the capillary exit can, however, only be explained by liquid microdrops impinging on the substrate with subsequent crystallization.

6.2 Cytochrome C solution microdrops (Graceffa, Burghammer et al. 2009)

6.2.1 Introduction

Stroboscopic X-ray scattering was extended to the much weaker SAXS signals from aqueous protein solution microdrops. Cytochrome C protein solutions used in this study make an ideal model system as they have been comprehensively studied using stopped flow and microfluidics techniques.(Pollack, Tate et al. 1999; Akiyama, Takahashi et al. 2002; Panine, Finet et al. 2006) (see Annex D) For comparison and detailed analysis of the radius of gyration (R_g), static SAXS experiments on cytochrome C solutions were performed at the ESRF-ID02 beamline. I also used the CRYSOL program to simulate the SAXS curve of globular cytochrome C from the crystal structure.(Svergun, Barberato et al. 1995) A test experiment with a single ballistic microdrop was performed to check the feasibility of stroboscopic SAXS.(Graceffa, Burghammer et al. 2009) Finally a microdrop mixing experiment in flight was performed to detect protein conformational changes inside the mixed microdrops.

6.2.2 Static experiments

Introduction: The stroboscopic experiments were performed at cytochrome C concentrations up to 4 mM in order to optimize the SAXS scattering signal. At these concentrations interparticle scattering will influence the Guinier curve and therefore calculation of R_g.(Akiyama, Takahashi et al. 2002) I have therefore measured the static SAXS curves of diluted cytochrome C solutions in order to determine the R_g value without interparticle scattering.

During the stroboscopic experiments 4 mM cytochrome C solution microdrops are mixed with 0.188 M Na-acetate solution microdrops. In order to determine the influence of the

dilution of the cytochrome C solution by Na-acetate buffer on the SAXS patterns I performed static SAXS experiments on a range of cytochrome C/Na-acetate solutions.

Methods: Cytochrome C solutions were prepared as described in section 5.1. SR-experiments were performed at the ID02 beamline in 16 bunch mode (see section 5.1 and Annex A).

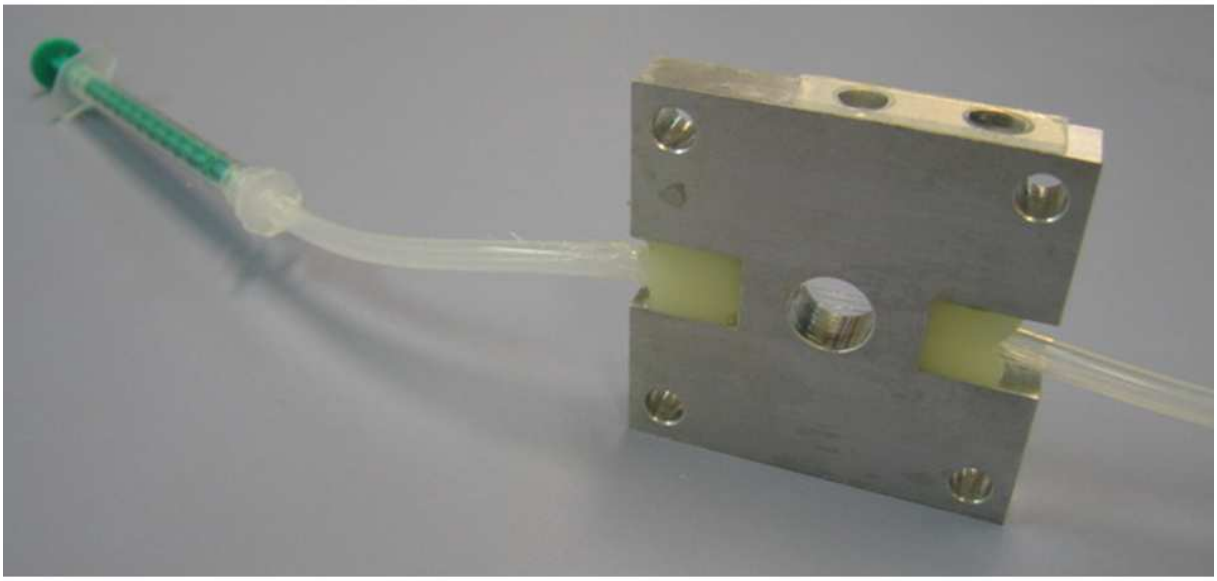

Figure 6.11 Picture of the ID02 flow-through cell.[h]

The solutions were loaded in a quartz capillary flow-through cell with internal diameter of about 2 mm. (figure 6.11). The incident and transmitted intensities were simultaneously recorded. For absolute intensity calibration, water was used. The patterns were corrected for the detector distortion and efficiency and the transmission of the sample. The 2D patterns were reduced to 1D patterns -I(Q)- by integrating the intensity over the azimuthal angle. The normalized 1D patterns were corrected for background scattering by subtracting the buffer scattering pattern obtained for the same geometry.

Figure 6.12 shows the 1D SAXS patterns (A) and the Kratky plots (B) of 4 mM cytochrome C solution (pH 2) diluted by Na-acetate solution (Table 6.1). A peak at 1.06 nm^{-1} appears in the Kratky plot as soon as Na-acetate is added. When the Na-acetate concentration reaches of 70.5 mM, the peaks shifts to 1.23 nm^{-1}. The folding process is then complete.

[h] www.esrf.fr/UsersAndScience/Experiments/SoftMatter/ID02/SampleEnvironment/PeltierFlowThrough

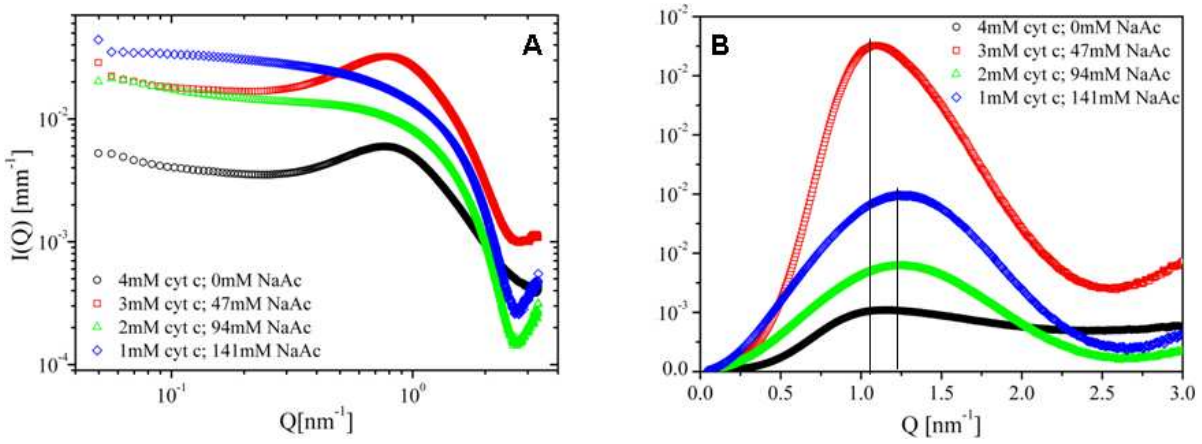

Figure 6.12 A: SAXS curves of 4 mM cytochrome C solution in HCl (cyt c) diluted with Na-acetate solution. B: Kratky plots; The peak at 1.06 nm^{-1} shifts to 1.23 nm^{-1} as the folding process is complete.

The solutions spectra show an interaction peak, due to the high concentration. Measurements of lower concentration solutions were performed to evaluate more accurately the radius of gyration (R_g). Figure 6.13 shows the SAXS curves (A) and Kratky plots (B) of unfolded cytochrome C solutions at pH2. SAXS curve and Kratky plots of folded cytochrome C solutions are shown in Figure 6.15A-D.

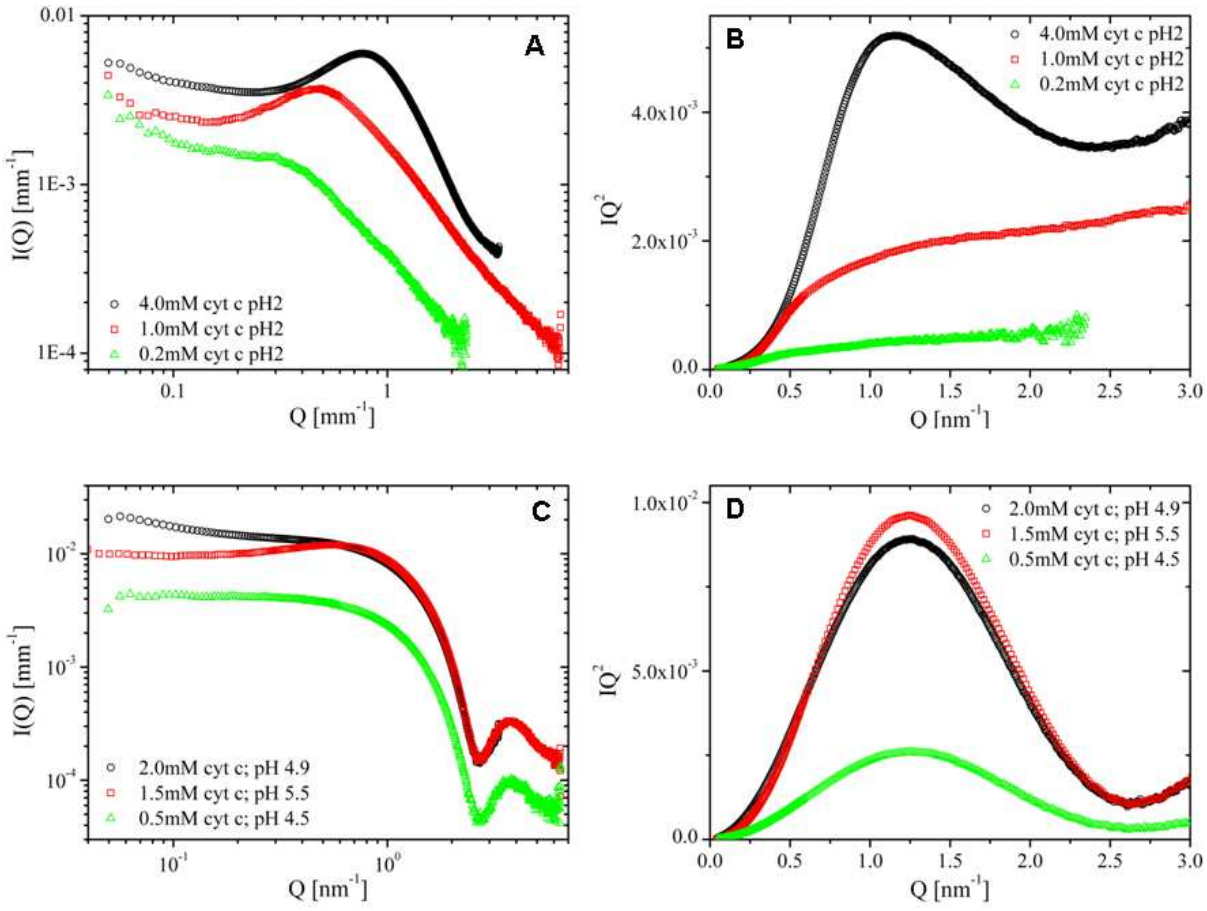

Figure 6.13 SAXS curves of unfolded (A) and folded (C) cytochrome C; Kratky plots of unfolded (B) and folded (D) cytochrome C solutions.

Figure 6.14A shows the Guinier plot of cytochrome C 0.5 mM solution at pH 4.5. The radius of gyration of the folded protein, calculated by the intercept, is 13.$_4$ Å. In Figure 6.16B is shown the Guinier plot of 1.0 mM cytochrome C solution at pH 2. The radius of gyration of the unfolded protein is 21.$_2$ Å.

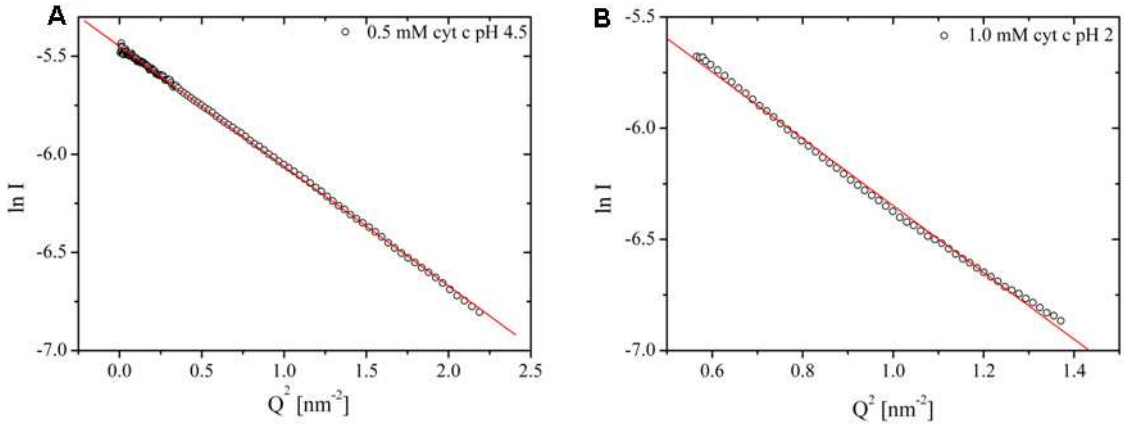

Figure 6.14 A: Guinier plot of 0.5 mM cytochrome C solution at pH 4.5 (folded; B: 1.0 mM cytochrome C solution at pH 2 (unfolded)

6.2.3 Simulations(Svergun, Barberato et al. 1995)

To calculate the theoretical solution scattering curve of folded cytochrome C solution from the atomic parameters, the software CRYSOL http://www.embl-hamburg.de/ExternalInfo/Research/Sax/crysol.html was used. The program uses multipole expansion of the scattering amplitudes to calculate the spherically averaged scattering pattern and takes into account the hydration shell. The file with the structure of the cytochrome C was downloaded by the Brookhaven Protein Data Bank, http://www.pdb.org/pdb/home/home.do a computer-based archival file for macromolecular structures, as derived from crystallographic studies.(Bernstein, Koetzle et al. 1977) The used crystallographic reference was the article (Banci, Bertini et al. 1999). The scattering curve obtained is plotted in Figure 6.15.

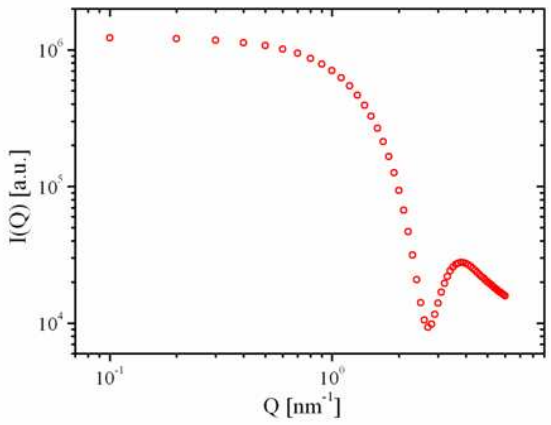

Figure 6.15 Theoretical scattering curve calculated with CRYSOL software.

6.2.4 Stroboscopic SAXS microdrop experiments

Methods (Graceffa, Burghammer et al. 2009): Stroboscopic experiments were performed at the ID13 beamline (see Annex A). SAXS data have been collected stroboscopically from ballistic microdrops of cytochrome C protein solution. The stroboscopic mode is imposed by triggering the readout of a fast framing silicon pixel with integrated readout electronics based on the Medipix2 chip (256*256 pixels of 55 μm pitch).(Llopart, Campbell et al. 2002; Ponchut, Clément et al. 2007) Details of the triggering operations are in the Methods chapter.

A 3*3 μm^2 monochromatic synchrotron radiation beam at a wavelength of 0.0965 nm was used for SAXS solution scattering. Microdrops were generated at a frequency of 2 KHz corresponding to a strobe period of 0.5 ms. The minimum framing time used was 5 μs. Scattering from the microdrops is accumulated on the pixel detector during the 10 s data collection period. This corresponds to an accumulated detector activation time of 100 ms.

The shape of the stroboscopically frozen microdrops can be determined by mapping them through the beam. The sample stage is moved by vertical and horizontal steps, to generate a composite SAXS image of the drop.

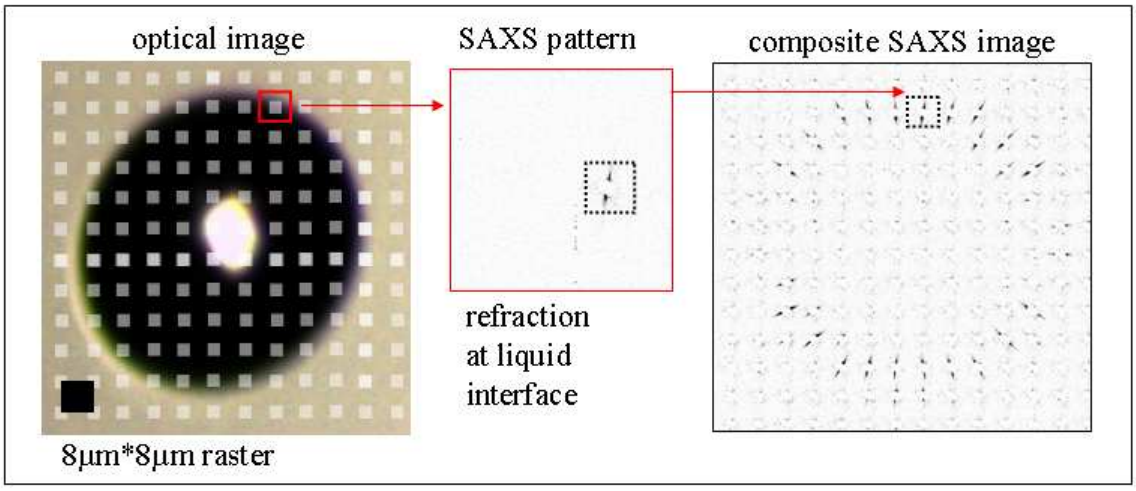

Figure 6.16 8μm 8μm mesh-scan (black square) of stroboscopically frozen microdrop by a microbeam of about 3 μm diameter symbolized by white squares. An example of a single recorded pattern with the interface refraction streak and composite image of all recorded patterns is also shown. The edge of the microdrops is indicated by the streaks which are oriented normal to the interface.*

The composite SAXS image in Figure 6.16 corresponds to a 8μm*8μm raster-scan. It shows streaks oriented normal to the microdrop interface, which are due to refraction from the air/water interface.(Mueller and Hentschel 2004) The image reveals therefore the outline of the 0.01 M HCl solution microdrop via the refraction streaks. Every "pixel" of the image corresponds to 10^4 accumulated patterns from different drops. The microdrop outline from the composite SAXS image corresponds well to the optically observed microdrop diameter of

about 80 µm and is also in agreement with the 71 µm capillary exit diameter specified by the manufacturer. The results suggest a high positional repeatability and a high volume fidelity of the microdrops. The refraction streaks provide also the possibility of analyzing the influence of the framing time on the microdrop shape. For a better visualization the integrated intensity of the streak and its orientation were recursively determined.(Davies 2006). The composite map in Figure 6.17A corresponds to Figure 6.16 but shows a gray-scale display of the intensity of the streaks and a vector-display (white lines) of the streak orientation. An increase in framing time increases the path length along the flight direction over which the interface scattering is recorded. This effect is analogous to the blurring observed when imaging a fast moving object with long exposure times. A framing time of t_f=5 μs shows practically no distortion whilst a framing time of t_f=30 μs results in the appearance of an elongated microdrop as interface scattering extends across several data collection positions.

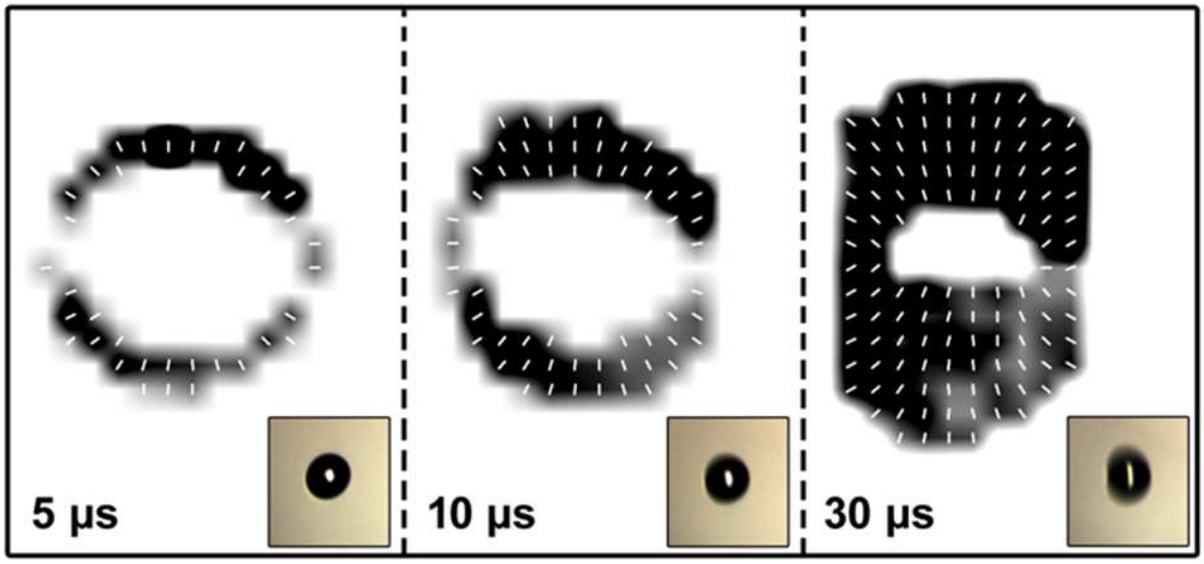

Figure 6.17 Influence of detector framing time on observed microdrop shape in mesh scan. Optical images are obtained with LED illumination for identical stroboscopic conditions (inset).

The speed of the microdrops was determined from the position of a sequence of microdrops under stroboscopic conditions as already shown for the paraffin microdrops. (Figure 6.18) The fit of a 2nd order polynomial suggests a speed of about 1.7 m/s at the 1.5 mm distance from the nozzle exit where the SAXS experiments were performed.

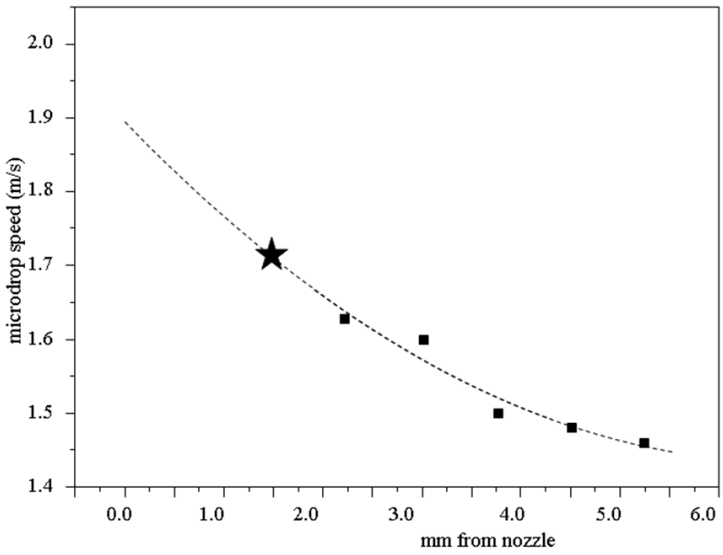

Figure 6.18 Microdrop speed derived from the optically determined position of the microdrops from the capillary exit. A 2nd order polynomial (barred curve) was fitted to the data (solid squares). The star corresponds to the microdrop position for the SAXS experiments

Data collection: Stroboscopic SAXS data could be collected from a solution of cytochrome C at pH 3.5 (2mM protein in 0.015 M HCl solution). The protein solution scattering was recorded close to the centre of the microdrops with 20 μs framing time for an accumulated detector time of 400 ms during 50 cycles in order to maximize the counting statistics and avoid the scattering from the edge. The air scattering was measured in the same way outside of the microdrop. The scattering coming from microdrops of 0.015 M HCl and the scattering coming only from the air were recorded, in order to perform a good background subtraction.

Data reduction: The scheme for data reduction has been indicated in section 5.5. The key point in the data treatment was the normalization for the sample thickness, since the microdrops do not have defined walls. The position where the microdrop is hit by the beam defines the length of X-ray path inside the sample. Scans were performed to find the microdrop position through the refraction streak at the solution/air interface. Figure 6.19A shows the positions of the scans points used to find the centre of the cytochrome C solution microdrop. The step size was 4 μm and the framing time 20 μs. From the observation of the refraction streaks (see inset of figure 6.19A) and the known size of the microdrop of 80 μm it was possible to determine the centre of the microdrop. It was fixed as the origin O(0,0,0) of an orthogonal coordinate system. The X axis is parallel to the beam direction. The points P(x_p, y_p, z_p) at which the beam hits the surface of the microdrop (Figure 6.19B) are described by the relation:

$$x_p^2 + y_p^2 + z_p^2 = r^2$$

with the sphere radius r=40 μm. x_p corresponds to half of the beam path inside the drop. It is equal to:

$$x_p = \sqrt{r^2 - {y_p}^2 - {z_p}^2}$$

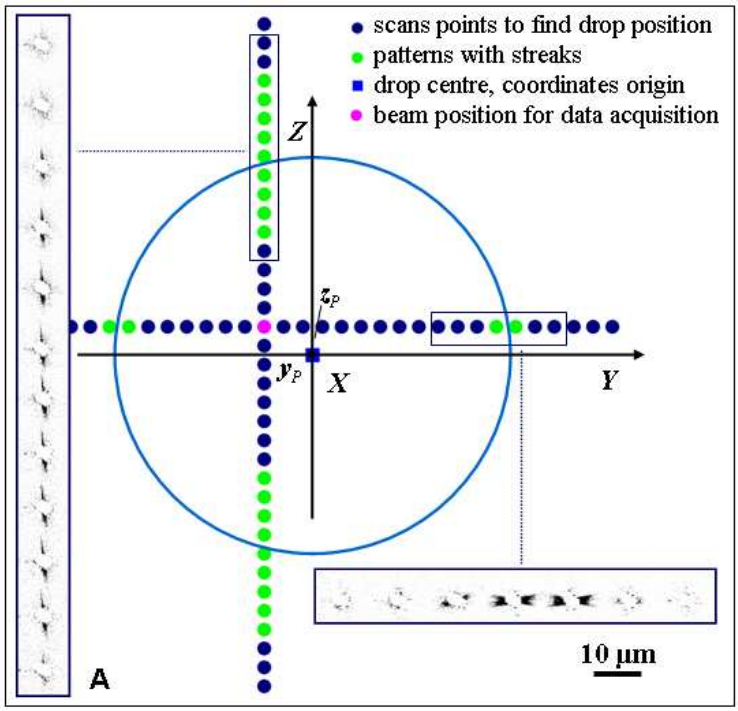

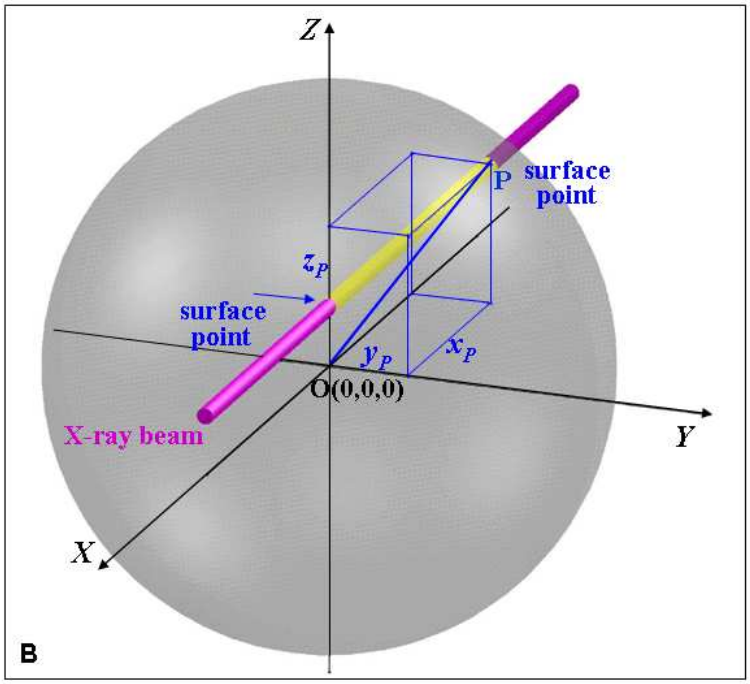

Figure 6.19 A: beam positions during the scan used to locate the microdrop. The green points show streaks coming from the air/liquid interface. The patterns of the selected points scan are shown on the insets. Note that the increased number of streaks in vertical direction is due to an increased framing time which implies blurring.(see Fig.6.17) The centre of the drop is assumed as the origin O(0,0,0) of a three-dimensional Cartesian space. B: The intersection of the beam position with the microdrop surface is individuated by points P(x_p, y_p, z_p). The x_p value is half of the beam path inside the microdrop.

The averaged raw 2D SAXS patterns of microdrop and air scattering were divided by their own exposure time and the averaged normalized primary beam intensity. (see also Methods 5.5) The pattern of the cytochrome solution was subtracted of the air pattern and, then, divided for x_p. (Figure 6.19B)

The scattering from the 0.015 M HCl solution microdrops was determined by a mesh-scan with 2.5 μm steps, 10 μs framing time and 100 ms exposure time (Figure 6.20). The liquid ejection speed at 2 kHz was 2ml/hr. For a total data collection time of 1hr 44 min, about 3.5 ml of the 4 ml volume storage container of the dispensing head were delivered. This implies a pressure drop in the storage container which reduces the microdrop speed systematically and results in a distortion of the drop shape. In subsequent experiments this was corrected experimentally by continuously refilling the reservoir by a syringe pump. Due to the change in microdrop speed, the shape of the spherical microdrop is distorted into an ellipse when visualized by the surface streaks (Figure 6.20A). The horizontal and vertical experimental step width is 2.5 μm. A cut through the centre of the microdrop corresponds to a circle with 80 μm diameter. Due to the vertical distortion into an ellipse the apparent vertical diameter has become 47.5 μm as visualized by the refraction streaks. In order to correct for this distortion one has to take the real diameter of 80 μm into consideration and define an apparent vertical step size of 4.2 μm (figure 6.20B). This is consistent with the number of vertical streaks. The upper ones are 5. Considering a path of 4.2 μm, the total length is 21 μm. Since the microdrop speed is 1.7 m/s, i.e. 1.7 μm/μs, the time needed to cover the distance is 12±2.5 μs. It is consistent with a framing time of 10 μs. A path of 2.5μm gives a time of 7.3±1.4 μs.

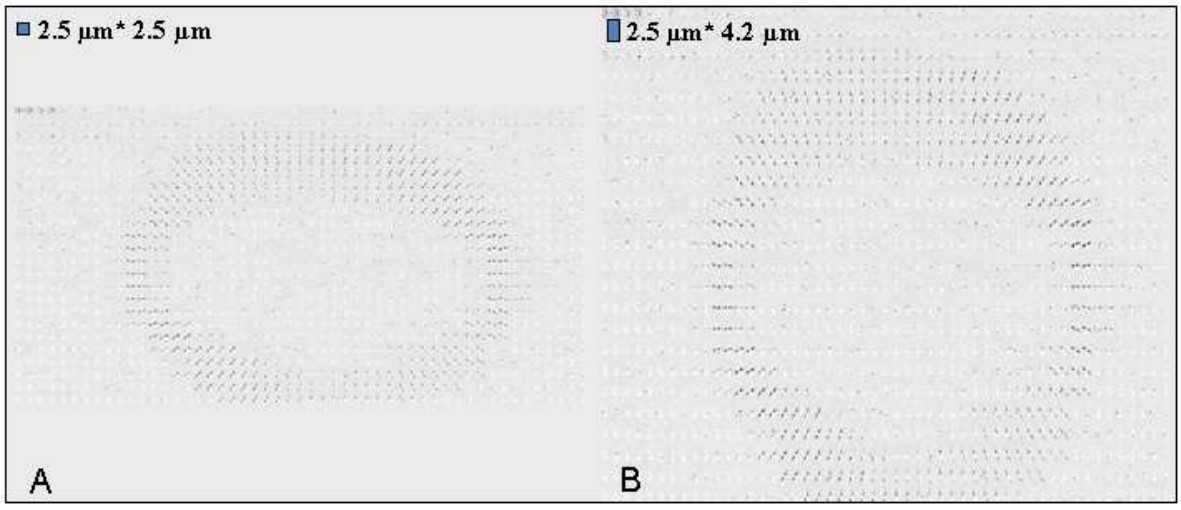

*Figure 6.20 A: Composite image of SAXS patterns collected with a raster-mesh of 2.5µm*2.5µm. The area of each "pixel" is limited to the Q-range of the refraction streak. The microdrop shape, revealed by the water/air interface refraction streaks, is distorted into an ellipse due to the change in microdrop speed with change of pressure in the reservoir.(see section 5.2.6) B: image corrected for the speed change. The apparent vertical step is 4.2µm.*

Every pattern of the mesh is inserted in a two-dimensional array (Figure6.21). The green pattern (array point 27,14) was chosen as origin O(0,0,0) of a three-dimensional space to characterized the points at the microdrop surface P(x_p, y_p, z_p) and find x_p.

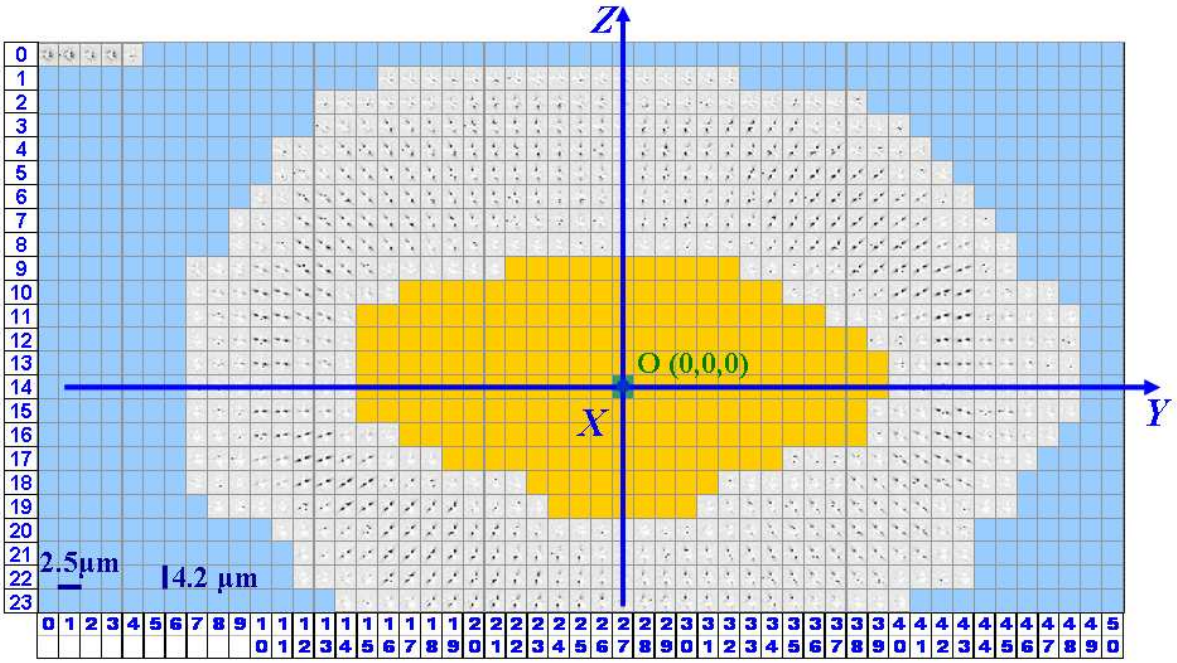

*Figure 6.21 Two-dimensional raster-grid used for background scattering. The pattern 27*14 (the green one) was chosen as origin O(0,0,0) of a three-dimensional space to characterized the points at the microdrop surface P(x_p, y_p, z_p) and find x_p (Figure 6.19B). The sum of patterns recorded on the yellow points was used as signal of the HCl solution, the sum among the blue ones was used for the air scattering.*

The HCl solution patterns of 203 mesh points (yellow squares in picture 6.21) were added up, avoiding any contributions from interface scattering. The air patterns of 406 mesh points (blue points of the picture 6.21) outside the microdrop were added up and dived by 2 (to normalize the data points). The two patterns were scaled to the normalized average incoming beam intensity and to the exposure time. The HCl scattering was subtracted of the air scattering. It was then divided by the sum of the beam paths inside the drop (Σx_p).

The scattering of the HCl solution was subtracted from the scattering of the cytochrome C solution. The resulting cytochrome C protein scattering signal was azimuthally averaged and used to calculate a Kratky plot providing information on the protein conformation.(Glatter and Kratky 1982)

Discussion of results: Figure 6.22A shows the SAXS pattern of cytochrome C at pH 3.5. The azimuthally averaged pattern (Figure 6.22B) confirms that the molecules in solution at pH 3.5 correspond to a native, folded morphology.(Panine, Finet et al. 2006) The radius of gyration, (Figure 6.23) derived from the Debye function (Calmettes, Durand et al. 1994; Akiyama,

Takahashi et al. 2002), of R_g=1.48 ±0.07 nm is in good agreement with data obtained from microfluidics experiments with similar protein concentrations.(Pollack, Tate et al. 1999)

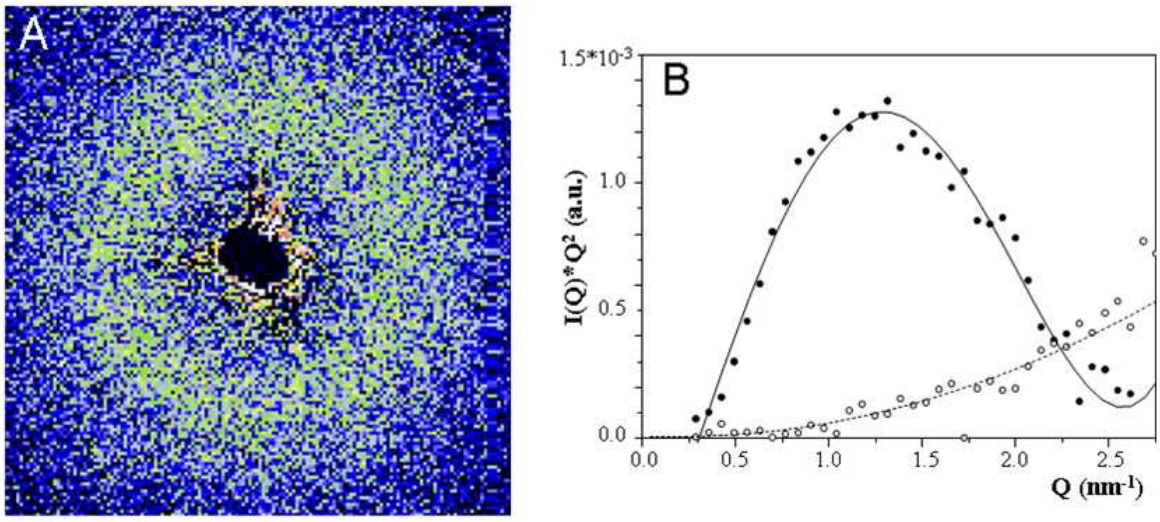

Figure 6.22 Pattern of Cytochrome C 2 mM, pH 3.5. The background scattering was subtracted as indicated in the text.

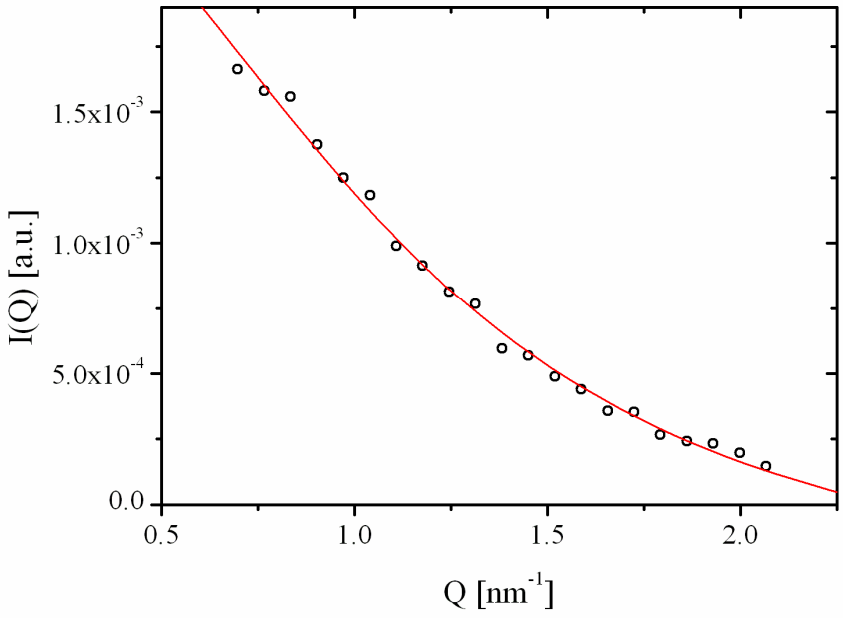

Figure 6.23 Scattering curve of 2mM folded cytochrome C in ballistic microdrop fitted with Debye function (red line)

Figure 6.24A,B shows a summary of the results obtained with the stroboscopic and static experiments and the theoretical calculations. The SAXS curve (Figure 6.24A) shows a peak at 0.7 nm^{-1} which increases with the protein concentration and is attributed to interparticle scattering. The Kratky plots in Figure 6.24B show that the stroboscopic cytochrome C data compare very well with static data obtained at ID02 and theoretical calculations on native cytochrome C.

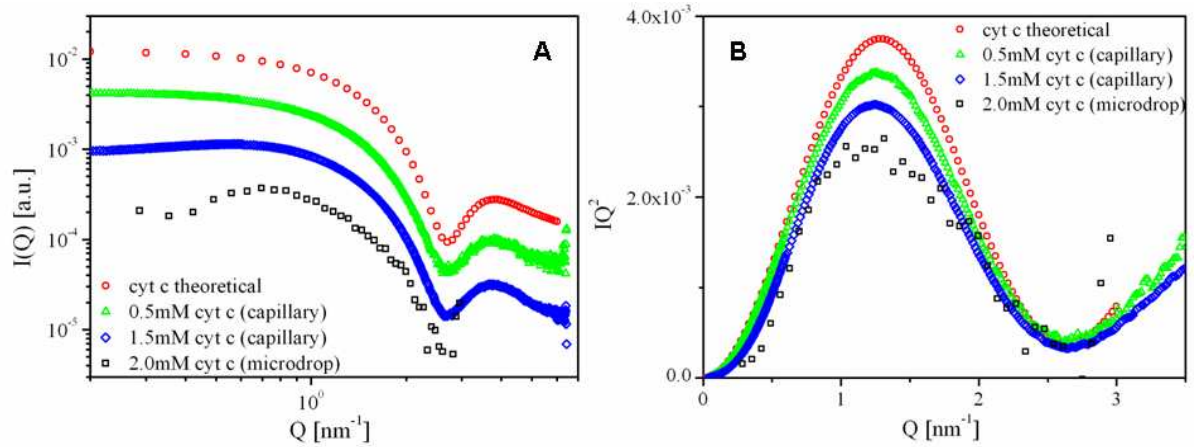

Figure 6.24 Comparison among the results obtained with the theoretical scattering curve ,the static experiments (@ID02) and the stroboscopic experiment on microdrops (@ID13). A: scattering curves; B: Kratky plots; curves have been multiplied by arbitrary scale factors with respect to the ID02 0.5 mM concentration value.

6.2.5 Stroboscopic SAXS microdop coalescence experiment

Methods: Coalescence experiments were performed using two DOD inkjet heads. (Figure 4.3: 5.2B) One inkjet head was generating 4 mM cytochrome C microdrops, the 2nd inkjet head 0.188 M Na-acetate buffer microdrops. The cytochrome C concentration in the mixed drop of about 2mM and pH 4.9 corresponded to the range of concentrations in microfluidic mixing experiments.(Pollack, Tate et al. 1999; Akiyama, Takahashi et al. 2002)

Stroboscopic SAXS experiments were performed at the ID13 beamline. (see section 6.2.4) Raster scans with step resolutions of 10*10 μm^2 or 20*20 μm^2 were performed at the point of coalescence and for the merged microdrops at two distances from the coalescence point corresponding to 2 ms and 4 ms after the coalescence. The framing time was 20 μs and the data collection time per point varied from 0.1 to 0.6 s. Therefore the signal collected for every raster-point corresponded was averaged among $5 \cdot 10^3$ microdrops (0.1 s), $1 \cdot 10^4$ microdrops (0.2 s), $3 \cdot 10^4$ microdrops (0.6 s). Patterns were collected in some points of the microdrops for an exposure time of 18 s, i.e. averaged among $9*10^5$ microdrops.

Results: A single SAXS pattern collected in 0.2 s, divided by its own incoming intensity values and air scattering subtracted, is shown in Figure 6.25A. The refraction streak at interface allows localizing the drop position and therefore the beam path inside the drop. The Figure 6.25B shows the region of the pattern used for azimuthal integration. The red region has been masked. Examples of the 1-D pattern obtained for 0.6 s and 0.2 s exposure time at different positions of the microdrop are shown in the Figure 6.26A,B.

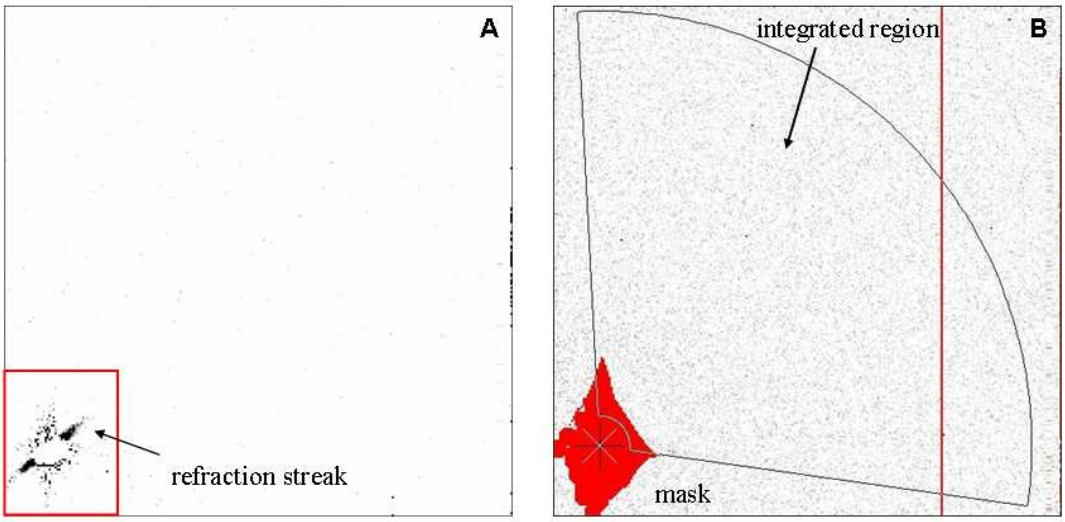

Figure 6.25 A: SAXS pattern collected at edge of a microdrop showing a streak due to refraction at the air/water interface. B: Region used for the azimuthal integration. The red pixels have been masked

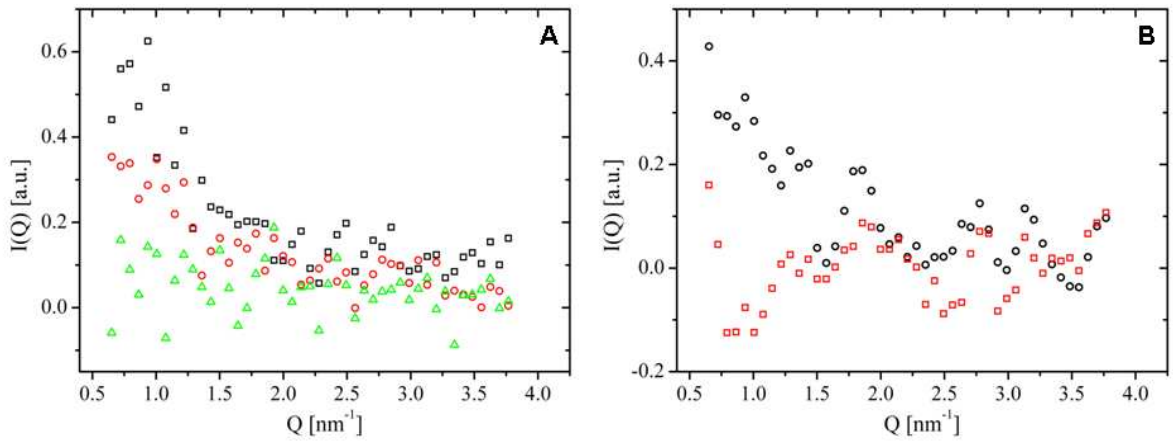

Figure 6.26 SAXS curves of the protein solution collected at different points of the microdrop. The exposure time was 0.5 s (A) and 0.2 s (B).

The intensity difference is mainly due to a gradient of protein concentration inside the microdrop. As shown in the Figures 6.13 A,C, the scattering intensities of the folded and unfolded protein are comparable.

Coalescence point: Raster scans with a step resolution of 20*20 μm^2 and exposure time of 0.2 s was performed. The area defined by the red square in the Figure 6.25A is used as a "pixel" in the composite SAXS image (Figure 6.27A) which allows localizing the contours of the microdrops via the refraction streak at the water/air interface. The azimuthal averaged patterns, indicated in the Figure 6.26, were integrated among the region 0.65 to 1.50 nm^{-1}. The map of this value is shown in Figure 6.27B. As the scattering from the buffer is much lower than the scattering from the protein, the composite image based on the integrated intensities reflects the local protein density. From the integrated intensity map one can localize the

position of the protein microdrop and of the acetate buffer microdrop. The microdrop with an integrated intensity >2 is identified as protein microdrop.

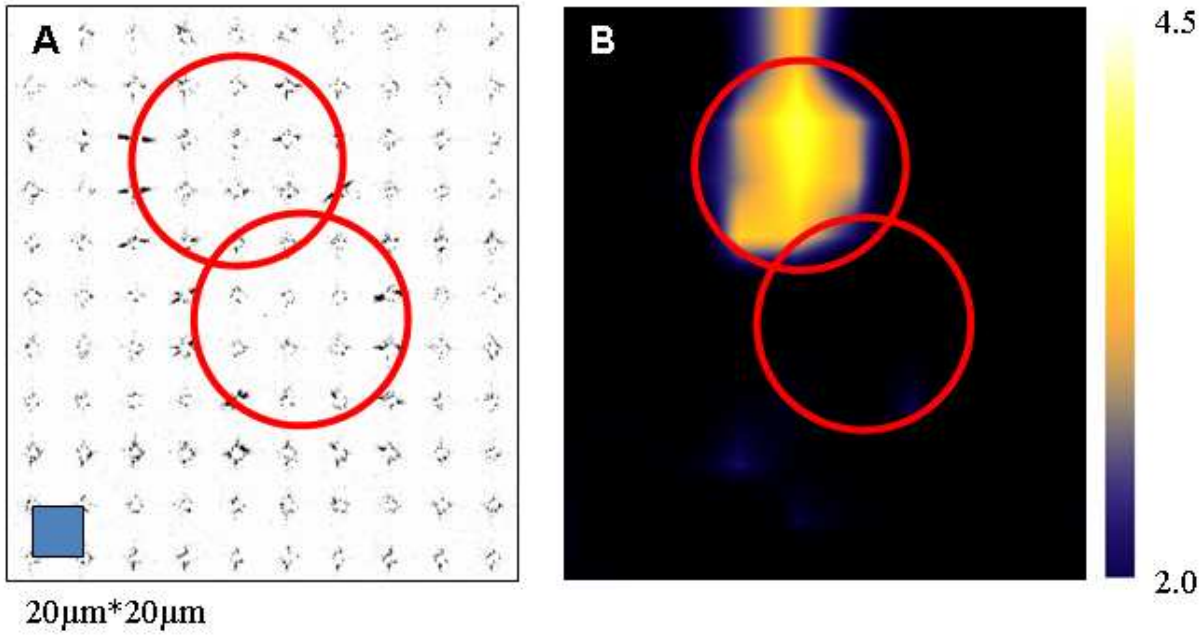

Figure 6.27 Composite image of the scattering close to the beamstop obtained at the coalescence point (A), The size of the raster-mesh is indicated by the blue square. The selected area of a "pixel" corresponds to the red square in Figure 6.25A. The contours of the microdrops are indicated by red circles. B: Integrated intensity map of the mesh points.

2 ms after coalescence: Raster scans with step resolutions of 10*10 μm^2, exposure time of 0.1 s (Figure 6.28 A/B) and 0.6 s (Figure 6.28 C) were performed. Figure 6.28A shows the composite SAXS image. After subtraction of air scattering, the patterns were azimuthally integrated and then normalized for the beam path inside the microdrop, so that the protein concentration is not masked by volume effects (Figure 6.28 B/C). The composite map in Figure 6.30 C corresponds to the region included in the white square of the Figure 6.28B. An inhomogeneous protein distribution at the outer rim of the merged microdrop is observed.

It is also interesting to compare the Kratky plots of the protein solution across the microdrop. The data collection time per point of 0.6 s used for the overview on the protein distribution is too short to determine a statistically significant Kratky curve. I collected therefore a series of patterns at two positions indicated in Figure 6.28C. The positions are closer to the rim (blue triangle) and close to the center (green triangles). The Kratky plots of the two points within the microdrop are shown in the Figure 6.28D. The superimposed red lines are scaled data collected at ID02 for 3 mM cytochrome C, 47 mM sodium-acetate solution. The data seems to point out the presence of a dilution gradient of the protein and suggest a beginning of the compactation processes. The dilution of the protein is a reasonable

assumption as the protein is more spread along the rim than in the microdrop before the onset of coalescence (Figure 6.27B). An onset of compactation is also a reasonable assumption given the neighboring protein and buffer layers. Whether the current data allow already a more quantitative simulation will have to be explored in more detail.

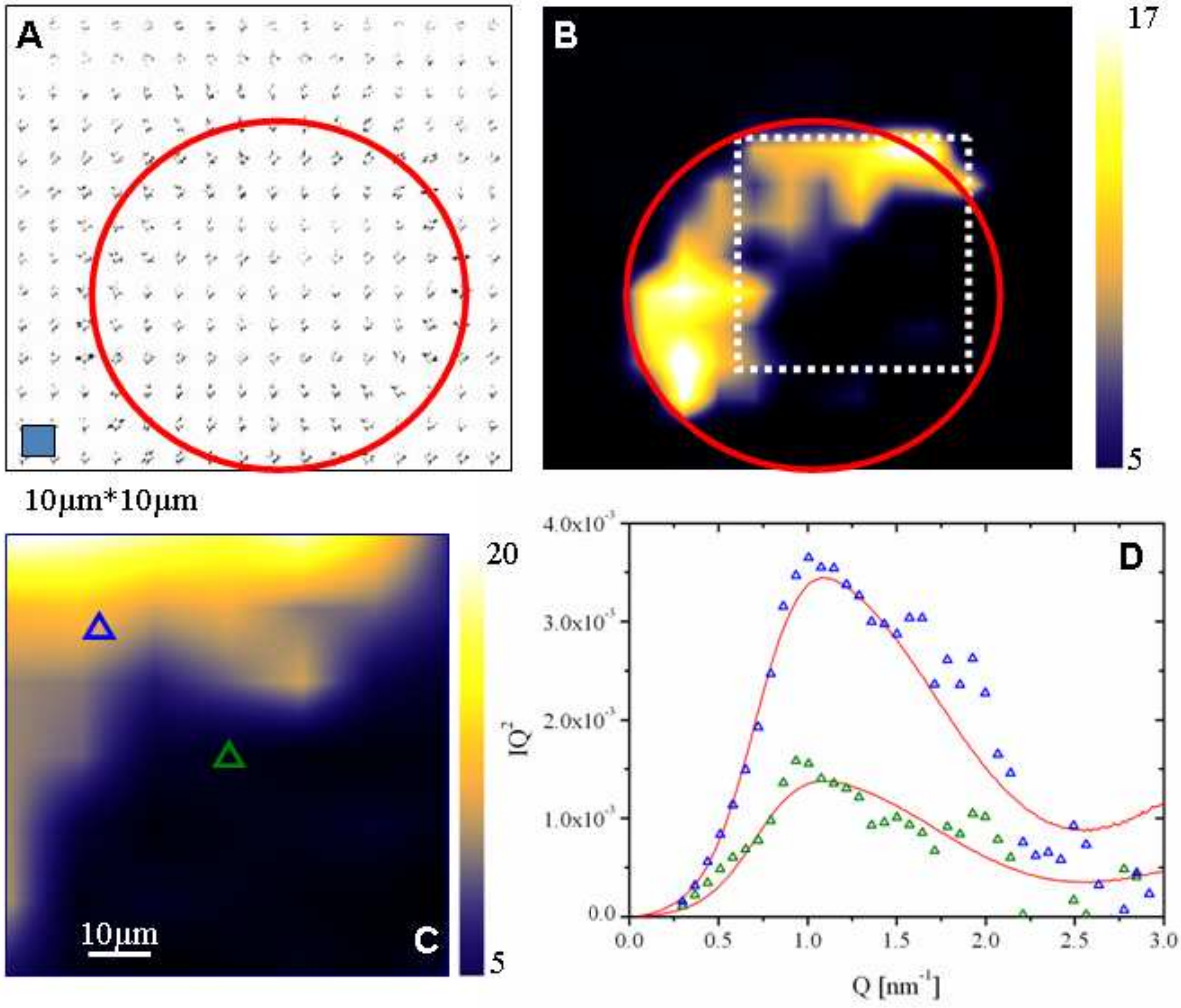

*Figure 6.28 Composite image of microdrop at 2 ms after coalescence point. Composite SAXS image (A) of a 10µm*10µm raster with 0.1 s exposure time and corresponding integrated intensity (B). The contours of the drop are schematically depicted by red circles defined by edge refraction. The white square indicates the region mapped with a 10µm*10µm raster of 0.6 s exposure time. The integrated intensity is shown in C. The blue and green triangle localize the beam position for the acquisition of pattern of exposure time of 18 s. Kratky plots corresponding to the two positions in D. The lines indicate the scaled ID02 data.*

4 ms after coalescence: Raster scans with step resolutions of 10*10 µm^2 and exposure time of 0.1 s was performed (Figure 6.29). The protein distribution has become rather homogeneous.

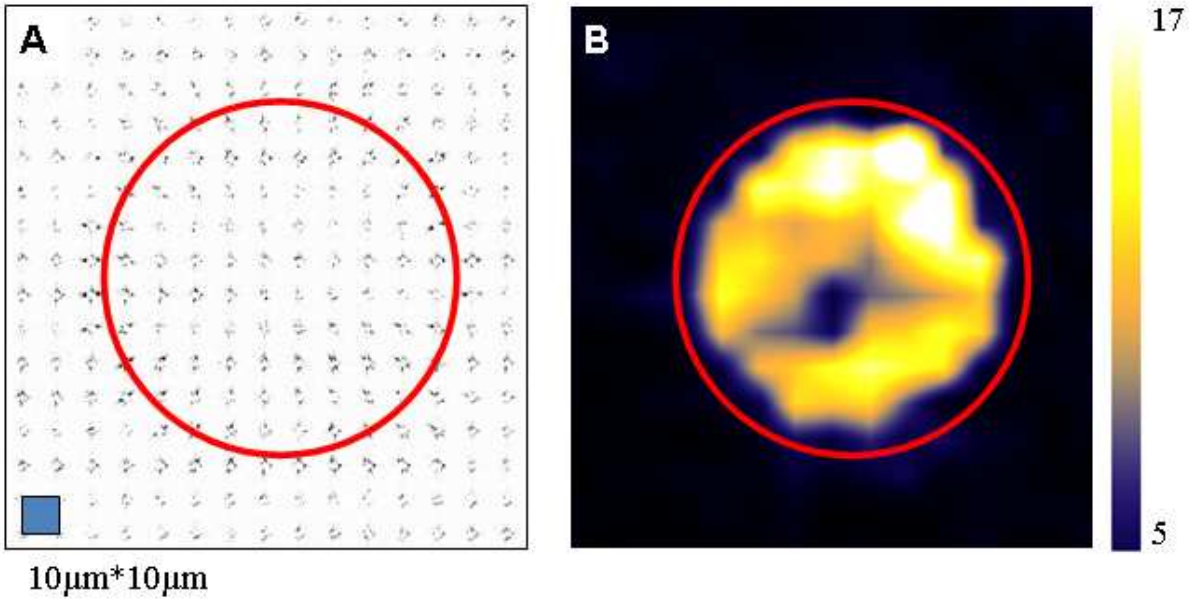

Figure 6.29 Composite images obtained at 4 ms from the merging point. A: SAXS pattern map of the drop; B: integrated intensity map of the drop. The values were normalized for the beam path.

Discussion of results: A raster-scan at 2 ms after the onset coalescence reveals a single microdrop with an inhomogeneous protein distribution. (Figure 6.28A) The protein is located roughly at the position of the protein microdrop at the coalescence point but has already started to spread at the rim of the microdrop and has therefore become more diluted. (Figure 6.28B) The data obtained close to the center of the drop suggest already a partial compactation as also observed by Akiyama et al., At 4 ms after the onset of coalescence a more homogeneous protein distribution is observed. (Figure 6.29B) The coalescence process is therefore joined by a mass redistribution inside the microdrop.

It is interesting to compare the inkjet mixing setup with the microfluidic droplet mixing device shown in Figure 6.30A. (Bringer, Gerdts et al. 2004) Aqueous droplets are injected into an immiscible solvent inside a microfluidic channel with hydrophobic walls. The droplets move typically with a velocity U=50 mm/s which induces a recirculation inside the droplets. Mixing is inefficient as there is no fluid exchange between the two vortices.(Ottino, Muzzio et al. 1992) The fluid exchange and therefore the speed the mixing can be enhanced by a winding channel (Figure 6.30B) which induces chaotic advection.(Bringer, Gerdts et al. 2004) Mixing time scales of a few ms can in this way be realized.

The principal difference of ballistic microdrops is their higher speed (~2 m/s) and therefore kinetic energy which is dissipated in the coalescence process through compression/expansion cycles. (Figure 4.4) These cycles are analogous to stretching/folding cycles inducing chaotic mixing in microfluidic mixers. It is therefore tentatively suggested

that the compression/expansion cycles induce chaotic advection reducing thus the mixing time.

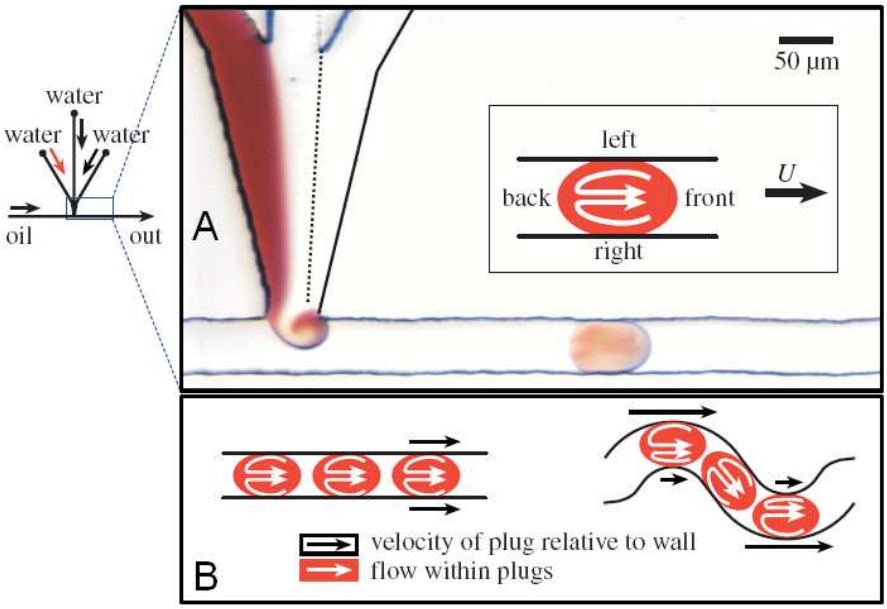

Figure 6.30 A: Formation of droplets from three aqueous solutions in a flow of immiscible fluid in a microfluidic channel. Oppositely rotating vortices are induced by the movement of the slug through the channel; B: A change of geometry from straight to winding channels induces chaotic advection; adapted from:(Bringer, Gerdts et al. 2004)

7. Conclusion et perspectives

J'ai montré dans ma thèse que la coalescence de microgouttes balistiques peut être maintenue pendant des périodes prolongées, avec une haute stabilité de la position, utilisant un instrument de mélange de gouttes pour jets d'encre synchronisés. Cela a fourni un premier aperçu dans la dynamique des changements de conformation de cytochrome C, avec une résolution de ms, sans les effets de tondage induits de la présence murale, rencontrés dans autres dispositifs microfluidiques. Je suppose qu'il est possible d'étudier le début du repliement du cytochrome C, conduit par pH, avec une résolution temporelle de sub-ms, dressèrent la carte, avec les rayons X, de microgouttes tout près du point de coalescence.

La expérimentation de technique stroboscopique pendant ca thèse ouvre la rue pour autres applications. La dynamique d'impact de microgoutte pourrait pour exemple être étudier et fournir des informations sur l'ordre moléculaire aux phénomènes de cristallisation ou des interfaces. La dynamique de cristallisation de paraffine et la congélation de microgouttes de solution de protéine aqueuses pourrait être étudiée comme une fonction de la nature du substrat et sa température. La prise au piège de structures métastables pourrait ainsi être explorée. Cela exige un développement techniques pour fournir une surface fraîche a chaque microgoutte qui arrive.

L'utilisation de microgouttes comme des transporteurs des cristaux n'a pas été explorée jusqu'à présent à la troisième génération de synchrotron, mais il va devenir une technique principale aux sources de laser à électrons libres. (Chapman 2009) La réduction de lu fond de diffusion avec technique stroboscopique, qui utilisent de système de jet d'encre devrait, cependant, aussi arriver à l'intérêt à la troisième génération de synchrotron.

7. Conclusions and perspectives

I have shown in my thesis that ballistic microdrop coalescence can be maintained for extended periods with a high positional stability using a novel DOD inkjet setup. This has provided a first glimpse into the dynamics of conformational changes of cytochrome C on the ms time-scale without shearing effects encountered in microfluidic mixing devices. The X-ray microbeam raster-scan technique applied to microdrops closer to the coalescence point should allow studying the onset of pH driven cytochrome C folding with a sub-ms time-resolution.

Stroboscopic SAXS/WAXS raster-scan techniques could also be used for studying the dynamics of microdrop impact and provide information on molecular ordering at interfaces or crystallization phenomena. Indeed the dynamics of paraffin crystallization and the freezing of aqueous protein solution microdrops could be studied as a function of the nature of the substrate and its temperature. The trapping of metastable structures could thus be explored. This requires, however, developing techniques of providing a fresh surface for every arriving microdrop.

The use of microdrops as carriers for specimen including single crystals has not been explored until now at 3rd generation SR-sources but is becoming a core technique at X-ray free electron laser sources.(Chapman 2009) The reduction of background scattering by stroboscopic techniques using DOD inkjet systems should, however, also become of interest at 3rd generation SR sources.

Acknowledgements

This thesis work has been realized thanks to the support of several people. I wish to thank primarily my supervisor, Christian Riekel for encouraging and pushing me constantly, Richard Davies that dedicated time and competences to the project, Manfred Burghammer, essential for making the experiment and for data analysis, Emanuela Di Cola, precious for the SAXS analysis, Lionel Lardiere for setting up the microdrop generator, Hervé Gonzalez for the electronics support and for writing the software to trigger the system with Manuel Perez, ID10A (A. Madsen) for lending the Medipix detector, Cyril Ponchut for setting up the detector, Anne Martel for the nice welcoming and the good advices for the sample preparations, Sebastian Schoeder, Aurelien Gourrier and Ronald Gebhardt for the several suggestions given and for the nice attitude of the group.

I wish to thank Narayanan Theyencheri for giving the possibility to make the static experiments on ID02 BL, Michael Sztucki for the help with the data collection.

I thank Isabelle Grillo for the support for the DSC measurements at ILL laboratory.

Annex A Beamlines used

A.1 ESRF-ID13 beamline

The schematic layout of the ID13-BL is shown in Figure A1. The two main experimental hutches provide micrometer-sized (EH-2) and nanometer-sized (EH-3) beams for applications, in particular in soft matter science and biology (Riekel 2000; Riekel, Burghammer et al. 2009).

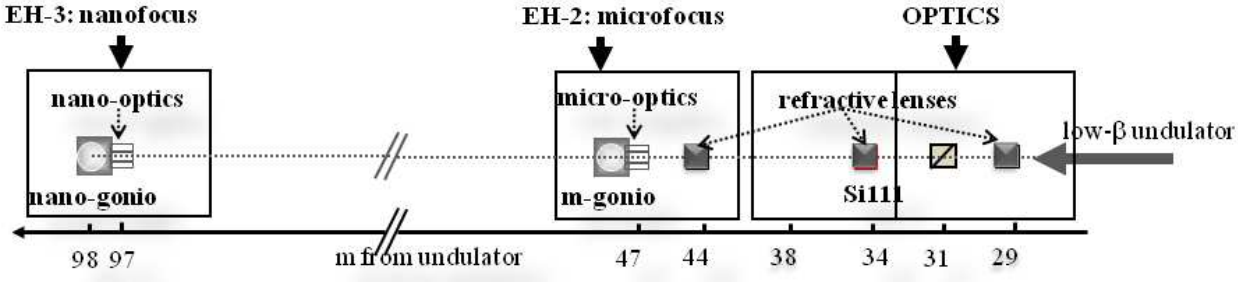

Figure A1 Layout of ESRF-ID13 beamline.(Riekel, Burghammer et al. 2009)
web page: www.esrf.eu/UsersAndScience/Experiments/SoftMatter/ID13/

An *in vacuum* low β undulator with 18 mm period is used as radiation source. Its maximum brilliance is at ~12.5 keV (1st order harmonics). The optical hutch contains a Si_{111} monochromator cooled by liquid N_2. The monochromatic beam is focused into the EH-2 hutch to an about 1*1 μm^2 s by KB-mirrors.(Hignette, Rostaing et al. 2001) The EH-2 hutch is not accessible if the EH-3 hutch is used. Beam sizes of about 100 nm (hor*vert) are generated by KB refractive lenses in EH-3(Schroer, Boye et al. 2008) and about 200-300 nm (hor*vert) by KB-mirrors. Parabolic Be-refractive lenses serve to match the beam size and divergence to the acceptance of the optical elements.

I have used for my thesis project the EH-2 hutch. It contains a scanning setup which provides a modular platform for a range of experiments with different sample environments.

A.2 ESRF-ID02 beamline

The schematic layout of the ESRF-ID02 BL is shown in Figure A2.

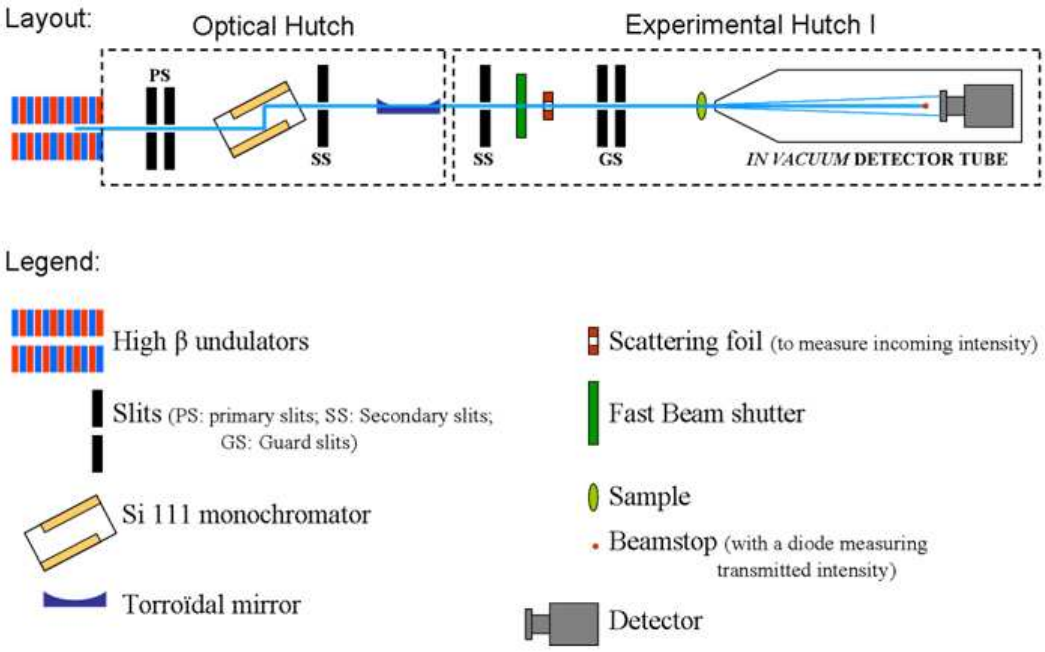

Figure A2 Layout of ESRF-ID02 beamline.
web page: www.esrf.eu/UsersAndScience/Experiments/SoftMatter/ID02/

Annex B Laboratory tools

B.1 OPIOM module control

The operation of the OPIOM module is schematically shown in Figure B1. It is driven trough a HyperTerminal (telnet program; author R. Davies) connection to a PC.

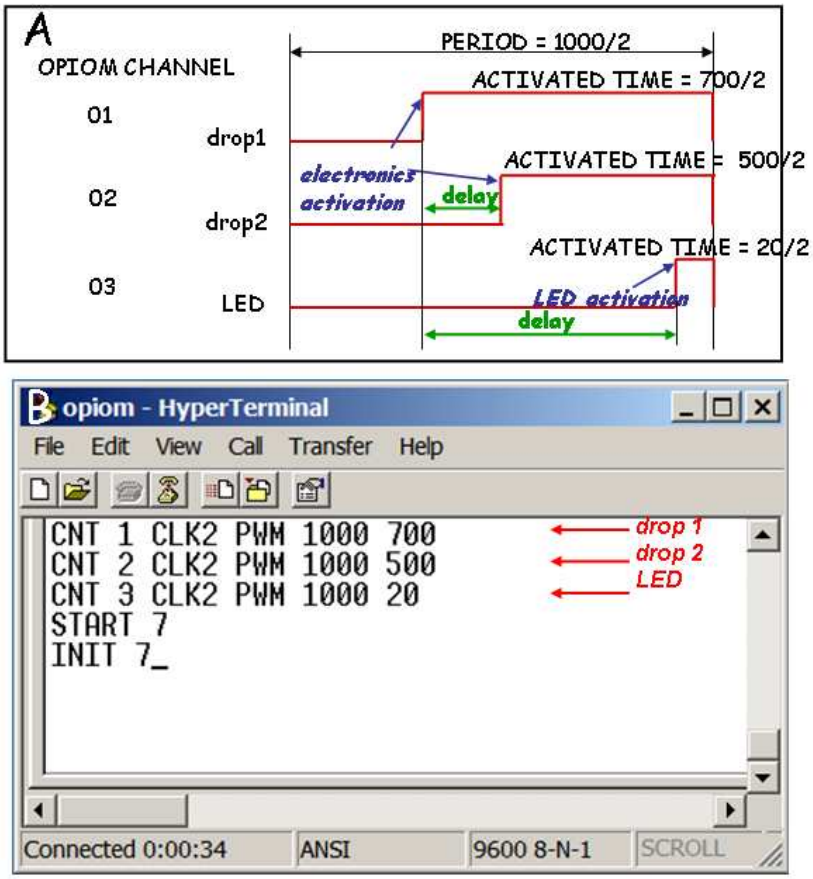

Figure B1 A: Operation sequence of OPIOM module. By setting the activated time(μs) it is possible to choose the delay between the drop emission and the LED activation (it changes the position of observed drops along its trajectory) and a delay between the two drops enabling the mixing process. B: PC screen hyperterminal input parameters

B.2 Triggering parameters calculation

Example: for input parameters (measurement unit: μs)

CNT: defines the count that receives the impulse.

CLK2: clock source 2

PWM: Pulse Width Modulation

1000: 2 * period value for stroboscopic SAXS/WAXS

700: 2 * activated time redistribution

START: it actives the channel

START 7: it actives the channels 1, 2 and 3, i.e. $(2^0 + 2^1 + 2^2)$

INIT: stops the sequence and initialize the values.

B.3 Motor control.

The motors are connected to a Linux computer and are controlled through SPEC.

rita.mac is the macro with motors parameters

To charge macro digit: qdo /users/opid13/rita.mac

To change cables:

1. Unplug the electrical cable
2. Unplug the motor
3. Plug the electrical cable, connect electricity
4. Set parameters using these commands:

	Cable number	*Motor name*
setpolluxmot	1	MTS70
setpolluxmot	2	MTS70
setpolluxmot	3	HT65

5. disconnect electricity
6. connect cable
7. connect electricity

The names of the motors are:

m1	connected to the cable 1	*x translation*
m2	connected to the cable 2	*y translation*
m3	connected to the cable 3	*z translation*

B.4 Electronics control

The communication of the DOD system with the PC is established via the AD-E-232 interface unit of the DDU. (Figure B2A)

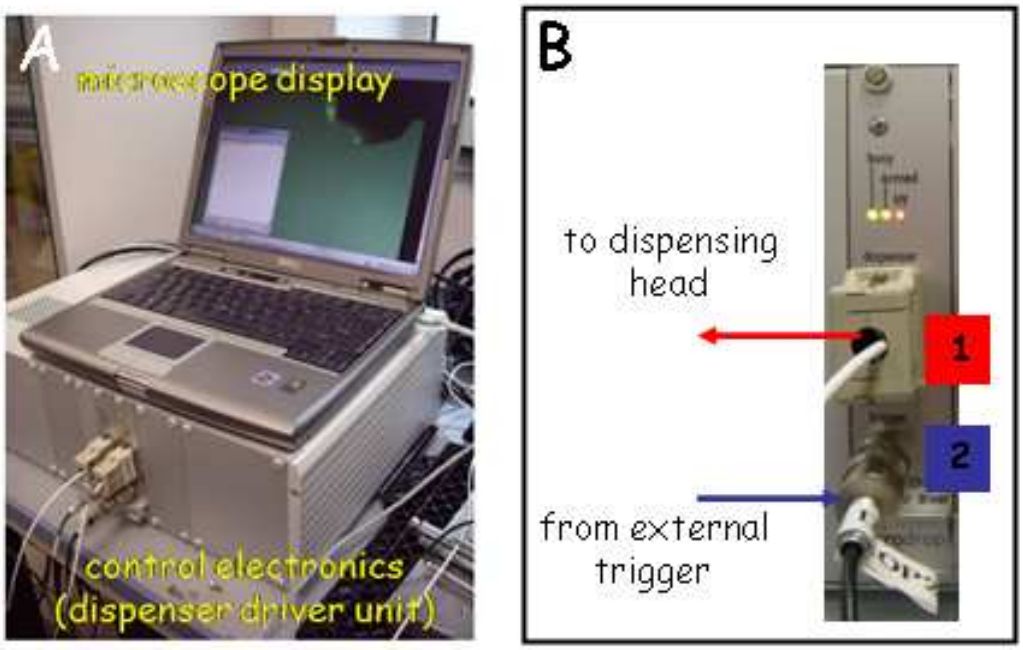

Figure B2 A:DDU electronics control; B: zoom of DDU AD-E-232 interface unit

The interface unit is connected via the serial interface 1 to the COM1 port of the PC. The AD-E-232 interface unit generates the driver pulse for the piezo actuator. (Figure B2B) It contains a high-voltage generator with voltage range of 30-200 V which controls voltage level, pulse duration, pulse frequency and numbers of microdrops per sequence. The DDU is connected to the dispensing head through the port 1. It generates the driver pulses after the trigger signal is released which can be internal or external. In the latter case the DDU is connected through the connection 2 to the external trigger (e.g. pulse-generator).

The LED display indicates the following status:

busy	the dispenser head is busy, driver pulse are generated; the electronics is switched on.
armed	the DDU is addressed, the drive parameters are loaded.
HV	high voltage is applied: drops are ejected

To drive the electronics we used the *Autodrop* software from *Microdrop Technologies GmbH*. Figure B3 shows the input screen of the program. One can select the inkjet head, change the voltage and pulse length values. Operation is possible in continuous or burst modes.

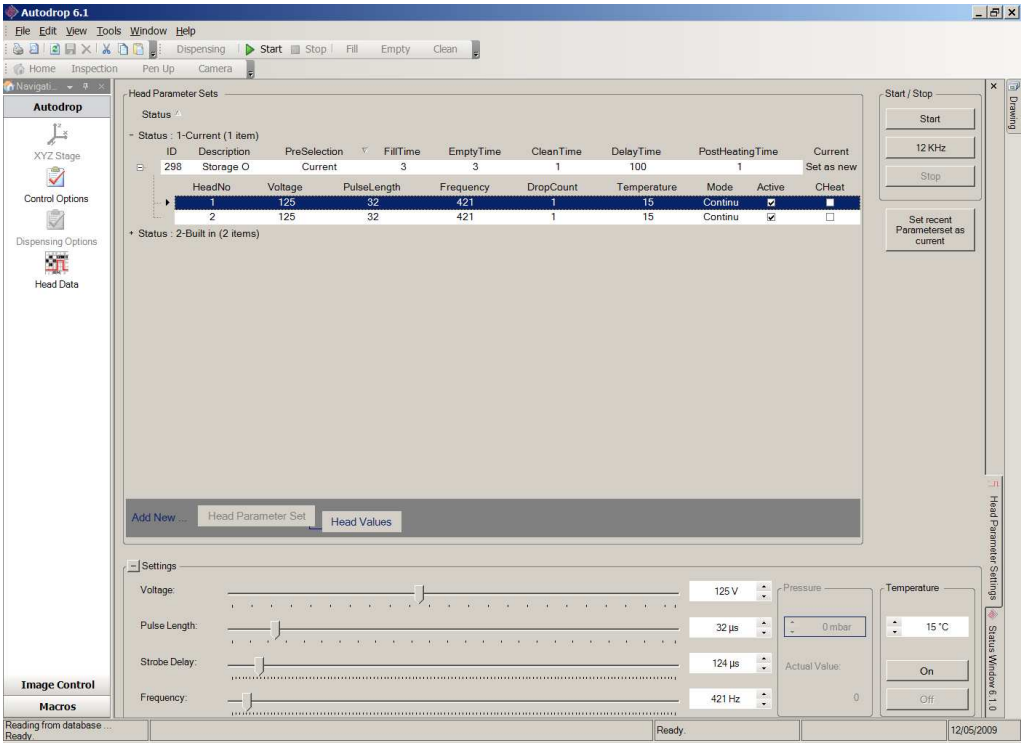

Figure B3: "Autodrop" users surface

The electronics can be triggered by selecting a specific mode from the control options panel (Figure B3)

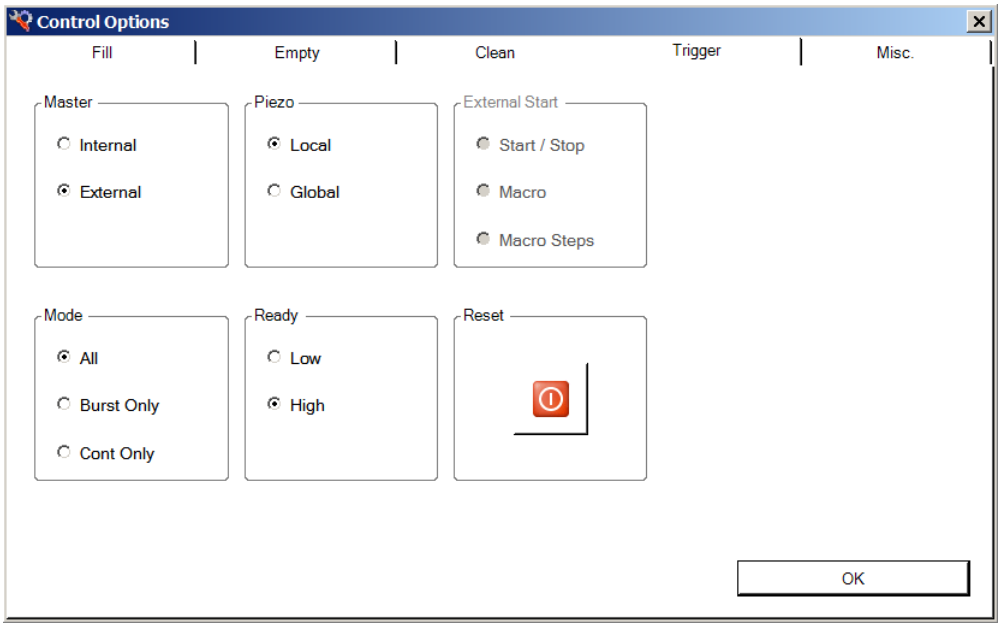

Figure B4 Microdrop control system panel

B.5 Syringe pump system

In order to keep the trajectory of the microdrops constant one has to maintain the pressure in the inkjet head constant via a constant liquid level in the storage container. Refilling of the

reservoir is done by a *Harvard Pico Plus* syringe pump system.[i] It is possible to set the diameter of the syringe and the speed of the liquid flow via a control program running on a PC. (Figure B5A/B)

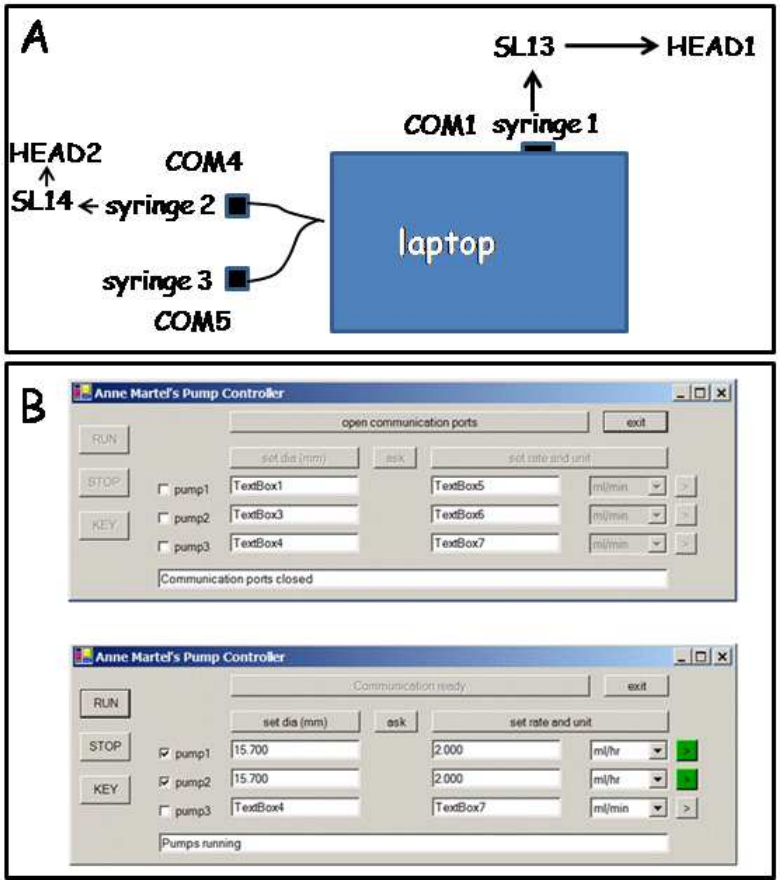

Figure B5 A: connection scheme of syringe control to laptop; SL: serial line; B: laptop input screen for syringe control

B.6 Syringe pump calculation

Example: The storage container of the dispensing head has 4 ml capacity. For a period of 1000 μs (frequency = 1 kHz) the ejection speed is 1ml/hr. In this condition a syringe speed of 1ml/hr allows to keep the level of the liquid inside the storage container stable.

Syringe specifications

Syringe	ID
30ml Omnifix	21.7 mm
5 ml Terumo	12.5 mm
2 ml Omnifix	9.5 mm
20 ml Terumo	19.7 mm
10 ml Omnifix	15.7 mm

Syringe used: 10 ml;

Tubing: portex fine bore polythene tubing; Ref 800/100/120; ID 0.38mm; OD 1.09 mm

[i] www.harvardapparatus.com/webapp/wcs/stores/servlet/haicat1_10001_11051_37295_-1_HAI_Categories_N

Annex C Beamline tools

C.1 Input parameters for triggering session (authors: M. Perez and H. Gonzalez)

SPEC session compatible

A schematic OPIOM sequence for the triggering of two microdrop heads, a LED and the Proxitronic image intensifier of the Frelon camera is shown in Figure C1.

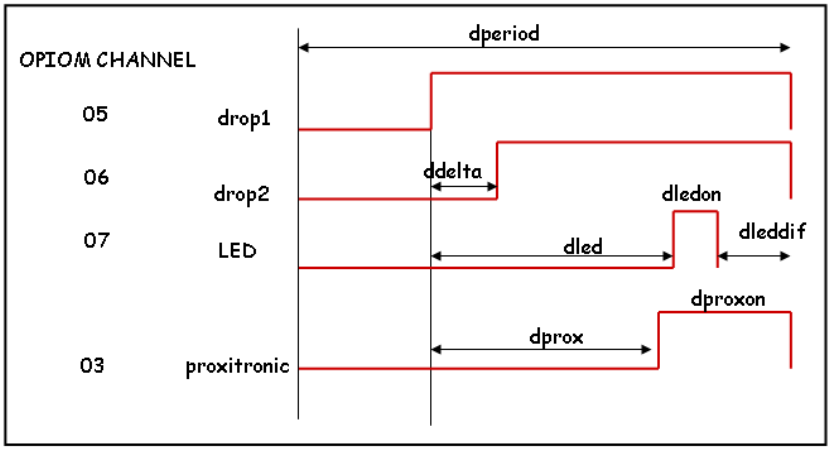

Figure C1 *Beamline program input parameters.*

The parameters are defined as follows

- *dperiod*: it defines the period of the stroboscopic sequence
- *ddelta*: it defines the delay between the electronic drivers activations of the two dispenser heads; it can be positive or negative
- *dled*: it defines the delay between the electronic 1 activations and the LED
- *dledon*: activated time of LED
- *dleddif*: it changes the period of the LED. This allows to see the drops at different positions and furthermore a movie of the drops falling down. To activate dleddif, the triggering of the detector must be off
- *dprox*: delay between the electronics1 activation and the detector readout activation
- *dproxon*: framing time of the detector readout

The parameters are defined via pseudo-motors in SPEC. They have to be set different from 0, except for *dleddif* that has to be 0 to activate *dproxon*. The following condition has to be respected:

$dled + dledon = dprox + dproxon$

$dperiod - (dled + dledon) \leq ddelta \leq dled + dledon$

Useful macros:

- ***dropon*:** activates drops and LED

- ***dropoff***: deactivates drops and LED
- ***dropproxyon***: activates triggering of the detector
- ***dropproxyoff***: deactivates triggering of the detector

N.B. to activate the detector channel (3) the fast shutter has to be open: fshon

For help: help local ID13microdrop

C.2 Pixel detector stroboscopic operation

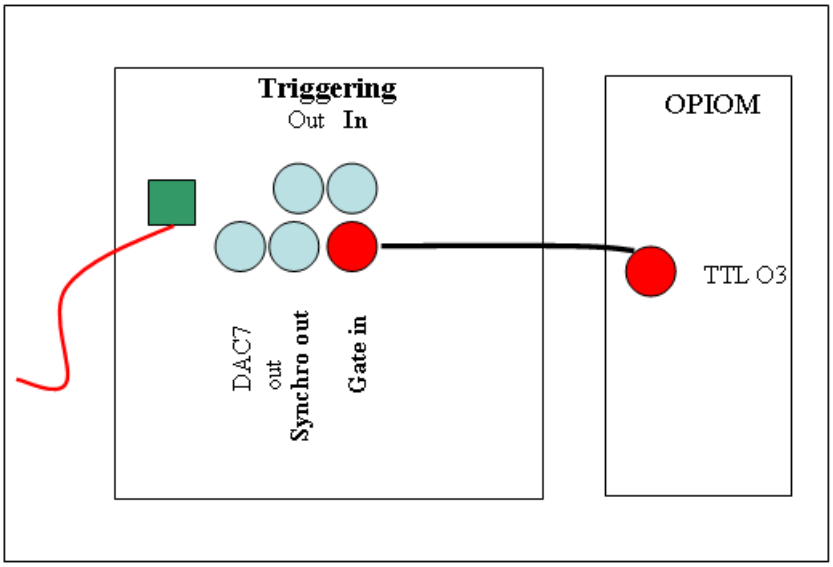

Figure C2 Connection of the detector to the OPIOM

To activate the gatering of the detector:

mpxmenu → 2 → 7 (gate) → 1: camera gatering active
0: camera gatering deactivated

Annex D SAXS studies on cytochrome C

D.1 Lamellar mixing in microfluidic cell(Pollack, Tate et al. 1999)

Pollack et al., have performed experiments with a *diffusive lamellar mixer* using 2.5 mM cytochrome C solution in pH 2 HCL and 0.1 M phosphate buffer at pH 7. A sub-ms mixing time ies estimated. Pollack et al., suggest a 2 states folding process: (1) a beginning compactness of the protein still denatured followed by (2) the formation of the native state.

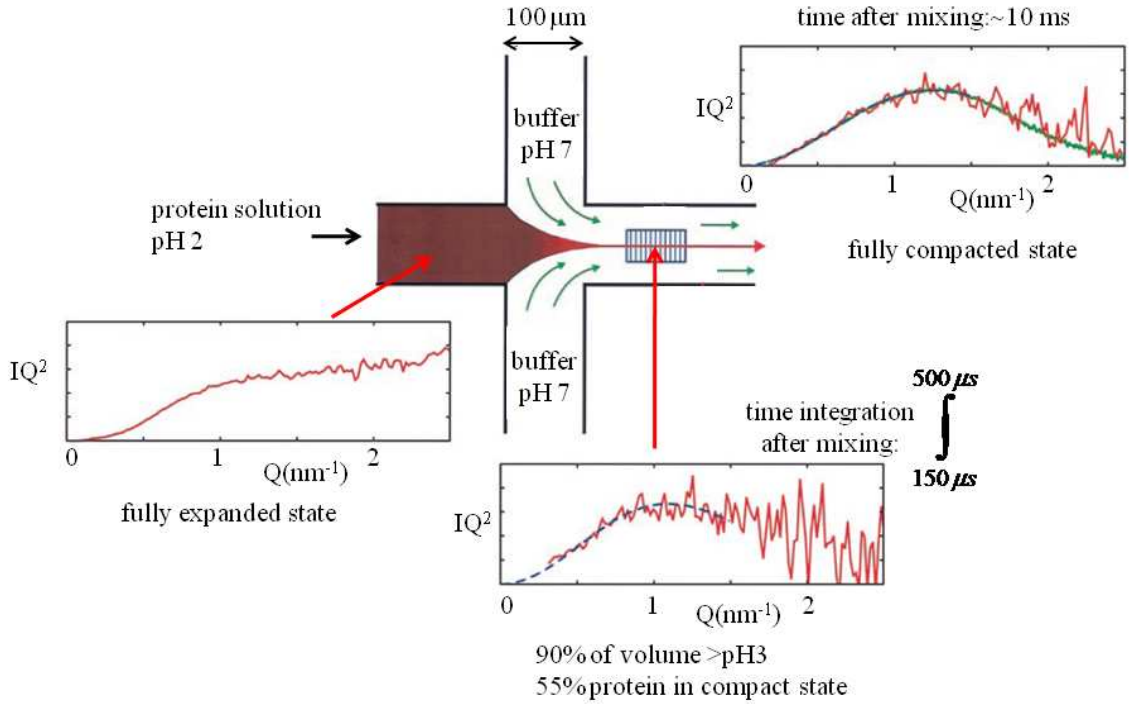

Figure D1 Kratky plots observed for lamellar flow geometry during mixing of pH 2 cytochrome C solution with pH 7 buffer. The time after mixing has been estimated from the position of the beam in the cell and the width of the beam

D.2 stopped flow mixing (Panine, Finet et al. 2006)

Panine et al. have performed experiments in a stopped flow mixing device using 20 mg/ml cytochrome C solution with 0.5 M acetate buffer. The stopped flow device provides turbulent mixing with a minimum mixing time of 2.5 ms.

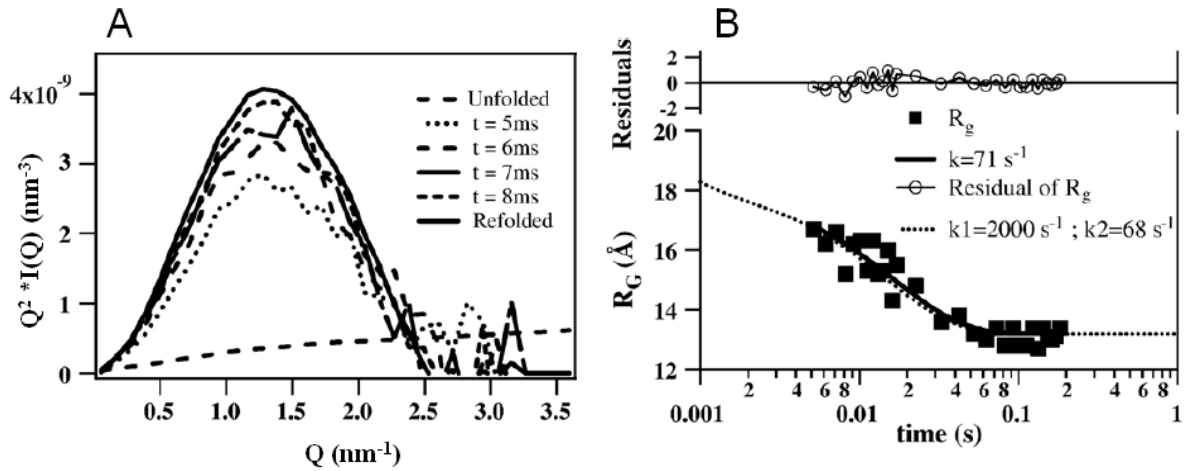

Figure D2 A: Refolding experiment of cytochrome C in the Kratky representation of scattered intensity for selected times after pH jump from 2.0 (unfolded state) to 5.4 (refolding conditions) ; B: Variation of the radius of gyration R_G during cytochrome C refolding in the time domain ranging from 4 to 188 ms. The squares and the solid line correspond to the measured R_G and a single-exponential fit. The dotted line represents the double-exponential fit described by: (Akiyama, Takahashi et al. 2002)Top: the residuals of the single-exponential fit.

D.3 Turbulent mixing in microfluidics cell(Akiyama, Takahashi et al. 2002)

Akiyama et al., have performed experiments in a continuous flow microfluidic mixing device. They claimed a dead time of 160 μs. A two states kinetics was derived from the data.

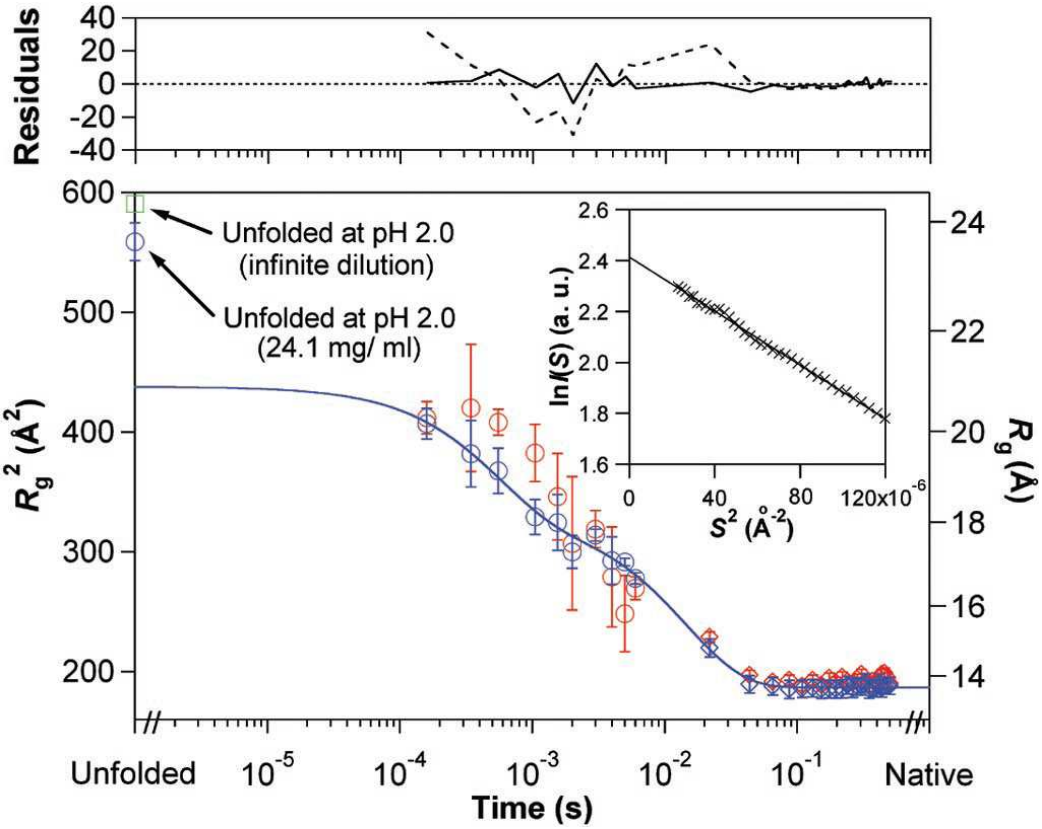

*Figure D3 Variation of R_G^2 of cytochrome upon refolding.(Akiyama, Takahashi et al. 2002) The blue and red points correspond to the results obtained for the protein concentrations at 24.1 and 10.9 mg*ml^{-1}, respectively. The bars denote the standard deviations from the independent measurements repeated several times for each condition. The two black circles correspond to experiments performed at the ESRF-ID02 beamline with a stopped flow apparatus.(Panine, Finet et al. 2006)*

The solutions used by Akiyama et al., are indicated below.

	$[\text{cytochrome C}]_{\text{initial}}$			$[\text{cytochrome C}]_{\text{final}}$		$[\text{NaAc}]_{\text{i}}$		$[\text{NaAc}]_{\text{f}}$	
	mg/ml	mM	pH	mg/ml	mM	mM	pH	mM	pH
Solution1	13.1	1.008	2	10.9	0.838	500	5.5	83	4.5
Solution2	28.9	2.223	2	24.1	1.864	500	5.3	83	4.5

Because of the significant interparticle scattering at the high concentration of cytochrome C (24.1 $mg*ml^{-1}$), it was impossible to determine R_g of the acid-unfolded state from the Guinier analysis (not shown). R_g of the unfolded state was therefore estimated by using a Debye function of a random coil chain as shown elsewhere.(Calmettes, Durand et al. 1994)

References

Akiyama, S., S. Takahashi, et al. (2002). "Conformational landscape of cytochrome c folding studied by microsecond-resolved small-angle x-ray scattering." Proc. Natl. Acad. Sci. USA **99**(3): 1329-1334.

Anson, M. L. and A. E. Mirsky (1931). "Protein Coagulation and its Reversal." The Journal of General Physiology **14**: 605-609.

Bacon, G. E. (1975). Neutron Diffraction. Oxford, Clarendon Press.

Badie, R. and D. F. d. Lange (1997). "Mechanism of drop constriction in a drop-on-demand inkjet system." Proc. R. Soc. Lond. A **453**: 2573-2581.

Banci, L., I. Bertini, et al. (1999). "Solution structure of reduced horse heart cytochrome c." J Biol Inorg Chem **4**: 21-31.

Bartlett, A. I. and S. E. Radford (2009). "An expanding arsenal of experimental methods yields an explosion of insights into protein folding mechanisms." Nature Structural & Molecular Biology **16**(6): 582-588.

Baruchel, J., J. L. Hodeau, et al. (1993). "Neutron and Synchrotron Radiation for Soft Condensed Matter studies." Les éditions de Physique.

Basaran, O. A. (2002). "Small-Scale Free Surface Flows with Breakup:Drop Formation and Emerging Applications." AIChE Journal **48**(9): 1842-1848.

Bernstein, F. C., T. F. Koetzle, et al. (1977). "The protein data bank: A computer-based archival file for macromolecular structures." J. Mol. Biol. **112**: 535-542.

Berthier, J. (2008). Microdrops and Digital Microfluidics. Norwich, N.Y., William Andrew.

Briard, A. J., M. Bouroukba, et al. (2006). "Thermodynamic and structural analysis and mechanisms of the crystallisation of multi-alkane model mixtures similar to petroleum cuts." Fuel **85**: 764-777.

Bringer, M. R., C. J. Gerdts, et al. (2004). "Microfluidic systems for chemical kinetics that rely on chaotic mixing of droplets." Phil. Trans. R. Soc. Lond. A **362**: 1087-1104.

Burgold, J., F. Weise, et al. (2005). "Evolution and Operating Experiences with Different Drop-On-Demand Systems." Macromol. Rapid. Commun. **26**: 265-280.

Calmettes, P., D. Durand, et al. (1994). "How random is a highly denatured protein." Biophysical Chemistry **53**: 105-114.

Chapman, H. N. (2009). "X-ray imaging beyond the limits." Nature Materials **8**: 299-301.

Chevallier, V., D. Petitjean, et al. (1999). "Mixtures of numerous different n-alkanes: 2. Studies by X-ray diffraction and differential thermal analysis with increasing temperature." Polymer **40**: 2129-2137.

Clift, R., J. R. Grace, et al. (1978). Bubbles, Drops and Particles. New York, Academic.

Creighton, T. E. (1994). Mechanisms of Protein Folding. Oxford, GBR, Oxford University Press.

Davies, R. (2006). "A new batch-processing data-reduction application for X-ray diffraction data." J. Appl. Cryst. **39**: 267-272.

Delaney, J. T., P. J. Smith, et al. (2009). "Inkjet printing of proteins." Soft Matter **5**: 4866-4877.

Dijksman, J. F. and A. Pierik (2008). "Fluid dynamical analysis of the distribution of ink jet printed biomolecules in microarray substrates for genotyping applications." Biomicrofluidics **2**: 044101.

Dootz, R., H. Evans, et al. (2007). "Rapid Prototyping of X-Ray Microdiffraction Compatible Continuous Microflow Foils." Small **3**(1): 96-100.

Elmqvist, R. (1951). Continuous Inkjet Printer US.

Endo, I., Y. Sato, et al. (1979). GB, Canon.

Fukai, J., Z. Zhao, et al. (1993). "Modeling of the deformation of a liquid droplet impinging upon a flat surface." Phys. Fluids A **5**(11): 2588-2599.

Gans, B. J. d., P. C. Duineveld, et al. (2004). "Inkjet printing of Polymers: State of the Art and Future Developments." Advanced Materials **16**(3): 203-213.

Gao, F. and A. A. Sonin (1994). "Precise deposition of molten microdrops: the physics of digital microfabrication." Proc. R. Soc. Lond. A **444**: 533-554.

Glatter, O. and O. Kratky (1982). Small Angle Scattering. Small Angle Scattering. O. Glatter and O. Kratky. N.Y., Academic Press.

Glatter, O. and O. Kratky (1982). Small Angle Scattering. N.Y., Academic Press.

Graceffa, R., M. Burghammer, et al. (2009). "Studying macromolecular solutions without wall effects by stroboscopic small-angle X-ray scattering." Appl. Phys. Let. **94**: 062902.

Graceffa, R., M. Burghammer, et al. (2008). "Synchrotron radiation microdiffraction of ballistic molten wax microdrops." Rev. Sci. Instrum. **79**: 086106-1.

Graceffa, R., M. Burghammer, et al. (2009). "Studying macromolecular solutions without wall effects by stroboscopic small-angle x-ray scattering." Appl Phys Lett **94**: 062902.

Grossmann, J. G. (2002). Shape Determination of Biomolecules in Solution from Synchrotron X-Ray Scattering. Scattering, Scattering and Inverse Scattering in Pure and Applied Science R. Pike and P. Sabatier, Elsevier Ltd. **2:** 1123-1139.

Guinier, A. and G. Fournet (1955). Small-Angle Scattering of X-Rays. New York, J. Wiley and Sons.

Hansen, C. and S. R. Quake (2003). "Microfluidics in structural biology: smaller, faster... better." Current Opinion in Structural Biology **13**: 538-544.

Hansen, C. L., E. Skordalakes, et al. (2002). "A robust and scalable microfluidic metering method that allows protein growth by free interface diffusion." PNAS **99**(26): 16531-16536.

Hignette, O., G. Rostaing, et al. (2001). "Submicron focusing of hard X-rays with reflecting surfaces at the ESRF." SPIE Conference Proceedings edited by McNulty: 105.

Jackson, S. E. (1998). "How do small single-domain proteins fold?" Fold. Des. **3**: R81-91.

Kim, H. Y., S. Y. Park, et al. (2003). "Imaging the high-speed impact of microdrop on solid surface." Rev. Sci. Instrum. **74**(11): 4930-4937.

King, S. M. (1999). Small-angle Neutron Scattering. Modern techniques for polymer characterisation. D. J. V. Pethrick R.A. Chichester, Great Britain, John Wiley & Sons Ltd**:** 171-225.

Knight, J. B., A. Vishwanath, et al. (1998). "Hydrodynamic Focusing on a Silicon Chip: Mixing Nanoliters in Microseconds." Phys. Rev. Let. **80**(17): 3863-3866.

Knight, K. (2002). "Honey, I shrank the lab." Nature **418**: 474-475.

Korol, S. and C. Greb (2000). Solid Ink Printing with Dynamic Drop Size Modulation. IS&T's NIP16: International Conference on Digital Printing Technologies, Vancouver, Society for Imaging Science and Technology, Springfield, MA.

Kyser, E. L. and S. B. Sears (1976). US, Silonic Inc.

Labiche, J. C., O. Mathon, et al. (2007). "The fast readout low noise camera as a versatile x-ray detector for time resolved dispersive extended x-ray absorption fine structure and diffraction studies of dynamic problems in materials science, chemistry, and catalysis." Rev. Scient. Instrum. **78**: 091301-1 - 091301-11.

Lee, E. R. (2003). Microdrop Generation. Boca Raton, CRC Press.

Lemke, H., M. Burghammer, et al. (2004). "Structural Processes during Starch Granule Hydration by Synchrotron Radiation Microdiffraction." Biomacromolecules **5**(4): 1316-1324.

Leng, J. and J. B. Salmon (2009). "Microfluidic crystallization." Lab on a Chip **9**: 24-34.

Levinthal, C. (1968). "Are there pathways for protein folding." Journal de Chimie Physique **65**(1): 44.

Lindner, P. (2002). Scattering Experiments: Experimental Aspects, Initial Data Reduction and absolute Calibration. Neutrons, X-Rays and Light: Scattering Methods Applied to Soft Condensed Matter. P. Lindner and T. Zemb. Amsterdam, North-Holland**:** 23-48.

Lion, N., T. C. Rohner, et al. (2003). "Microfluidic systems in proteomics." Electrophoresis **24**: 3533-3562.

Llopart, X., M. Campbell, et al. (2002). "Medipix2: A 64-k pixel readout chip with 55-μm square elements working in single photon counting mode." IEEE Transactions On Nuclear Science **49**: 2279-2283.

Mueller, B. R. and M. P. Hentschel (2004). "Synchrotron radiation refraction topography for characterization of lightweight materials." X-Ray Spectrom. **33**: 402-406.

Narayan, T. (2008). Soft Matter: Characterization. Berlin-Heidelberg, Springer.

Narayan, T. (2008). Synchrotron small-angle X-ray scattering. Soft Matter: Characterization. R. Borsali and R. Pecora. Berlin-Heidelberg, Springer**:** 899-952.

Ottino, J. M., F. J. Muzzio, et al. (1992). "Chaos, symmetry, and self-similarity - exploiting order and disorder in mixing processes." Science **257**: 754-760.

Ottino, J. M. and S. Wiggins (2004). "Introduction: mixing in microfluidics." Phil. Trans. R. Soc. Lond. A **362**: 923-935.

Panine, P., S. Finet, et al. (2006). "Probing fast kinetics in complex fluids by combined rapid mixing and small-angle X-ray scattering." Advances in Colloid and Interface Science **127**: 9-18.

Pfohl, T., F. Mugele, et al. (2003). "Trends in microfluidics with complex fluids." Chem. Phys. Chem. **4**(12): 1291-1298.

Pollack, L., M. W. Tate, et al. (1999). "Compactness of the denaturated state of a fast-folding protein measured by submillisecond small-angle x-ray scattering." Proc. Natl. Acad. Sci. USA **96**: 10115-10117.

Pollack, L., M. W. Tate, et al. (2001). "Time Resolved Collapse of a Folding Protein Observed with Small Angle X-Ray Scattering." PRL **86**(21): 4962-4965.

Ponchut, C., J. Clément, et al. (2007). "Photon-counting X-ray imaging at kilohertz frame rates." Nucl. Instrum. Methods A **576**: 109-112.

Ponchut, C., J. Clément, et al. (2007). "Photon-counting X-ray imaging at kilohertz frame rates." Nucl. Instrum. Methods **A 576**: 109-112.

Ponchut, C., J. L. Visschers, et al. (2002). "Evaluation of a photon-counting hybrid pixel detector array with a synchrotron X-ray source." NIM A **484**(1-3): 396-406.

Ponchut, C., F. Zontone, et al. (2005). "Experimental Comparison of Pixel Detector Arrays and CCD-based Systems for X-ray area detection on Synchrotron Beamlines." IEE Trans. Nucl. Sci. **52**: 1760-1765.

Rein, M. (1993). "Phenomena of liquid drop impact on solid and liquid surfaces." Fluid Dynamics Research **12**: 61-93.

Riekel, C. (2000). "New Avenues in X-ray microbeam experiments." Rep. Prog. Phys. **63**: 233-262.

Riekel, C. (2000). "New avenues in x-ray microbeam experiments." Reports on Progress in Physics **63**(3): 233-262.

Riekel, C., M. Burghammer, et al. (2009). Fundaments of Soft Condensed Matter Scattering and Diffraction with Microfocus Techniques. Applications of Synchrotron Light to Scattering and Diffraction in Materials. T. A. Ezquerra, M. Garcia-Gutierrez, A. Nogales and M. Gomez. Heidelberg, Springer. **776:** 91-104.

Riekel, C., M. Burghammer, et al. (2004). "Combined microdrop generation and microdiffraction for biopolymer hydration experiments." Fibre Diffraction Review **12**: 36-40.

Roder, H., Shastry, M C R (1999). "Methods for exploring early events in protein folding." Current Opinion in Structural Biology **9**: 620-626.

Rössle, M., D. Flot, et al. (2003). "Fast intra-crystalline hydration of β-chitin revealed by a combined microdrop generation and on-line synchrotron radiation microdiffraction." Biomacromolecules **4**: 981-986.

Schoeck, J., R. J. Davies, et al. (2007). "Na-cellulose formation in a single cotton fiber studied by synchrotron radiation microdiffraction." Biomacromolecules **8**(2): 602-610.

Schroer, C. G., P. Boye, et al. (2008). "Coherent X-Ray Diffraction Imaging with Nanofocused Illumination." Phys. Rev. Lett. **101**: 090801.

Song, H., D. L. Chen, et al. (2006). "Reactions in droplets in microfluidic channels." Angew. Chem. Int. Ed. **45**: 7336-7356.

Svergun, D., C. Barberato, et al. (1995). "*CRYSOL-a* Program to Evaluate X-ray Solution Scattering of Biological Macromolecules from Atomic Coordinates." J. Appl. Cryst. **28**: 768-773.

Svergun, D. and M. Koch (2003). "Small-angle scattering studies of biological macromolecules in solution." Rep. Prog. Phys. **66**: 1735-1782.

Sweet, R. G. (1965). "High Frequency Recording with Electrostatically Deflected Ink Jets." Rev. Sci. Instrum. **36**: 131-136.

Ungar, G. (1983). "Structure of rotator phases in n-alkanes." J. Phys. Chem. **87**: 689-695.

Ungar, G. and N. Masic (1985). "Structure of rotator phases in n-alkanes." J. Phys. Chem. **89**: 1036-1942.

Utada, A. S., A. Fernandez-Nieves, et al. (2007). "Dripping to Jetting Transitions in Coflowing Liquid Streams." Phys. Rev. Let. **99**: 094502.

Vaughan, D., Ed. (1986). Center for X-Ray Optics X-Ray Data Booklet. Berkeley, Lawrence Berkeley Laboratory.

Weiss, T. M., T. Narayanan, et al. (2005). "Dynamics of the Self-Assembly of Unilamellar Vesicles." Phys. Rev. Lett.: 038303-1 - 038303-4.

Whitesides, G. M. (2006). "The origins and the future of microfluidics." Nature **44**: 368-373.

Wunderlich, B. (1990). Thermal Analysis. Boston, Academic Press.

Xu, J. and D. Attinger (2008). "Drop on demand in a microfluidic chip." J. Micromech. Microeng. **18**: 1-10.

Xu, Q. and O. A. Basaran (2007). "Computational analysis of drop-on-demand drop formation." Phys. Fluids **19**: 102111.

Zaugg, F. G. and P. Wagner (2003). "Drop-on-Demand Printing of Protein Biochip Arrays." MRS Bulletin **28**(11): 837-842.

Zoltan, S. L. (1974). US, Clevite Corp.